Doctoral Programme in Sciences
Doctoral School of the Universitat Jaume I

Small Perturbation Techniques for the Electronic Analysis of Perovskite Devices

Report submitted by Agustín Bou Catalá in order to be eligible for a doctoral degree awarded by the Universitat Jaume I

Author
Agustín Bou Catalá
Signature:

Director
Juan Bisquert Mascarell
Signature:

Castelló de la Plana, November 2022

Received Funding

The following sources were responsible for funding the research carried out in this thesis.

- FPI grant for pre-doctoral students provided by Ministerio de Economía, Industria y Competitividad (MINECO), Spain, grant number: BES-2017-080351

- Project – “Perovskitas fotovoltaicas estabilizadas de alto rendimiento” from MINECO, Spain, reference number: MAT2016-76892-C3-1-R

Attribution-ShareAlike License CC BY-SA.

Thesis by compendium of publications:

1. Bou, A.; Pockett, A.; Raptis, D.; Watson, T.; Carnie, M. J.; Bisquert, J. Beyond Impedance Spectroscopy of Perovskite Solar Cells: Insights from the Spectral Correlation of the Electrooptical Frequency Techniques, *The Journal of Physical Chemistry Letters*, **2020**, *11*, 8654–8659. DOI: 10.1021/acs.jpclett.0c02459, Impact Factor: 6,475

2. Bou, A.; Āboliņš, H.; Ashoka, A.; Cruanyes, H.; Guerrero, A.; Deschler, F.; Bisquert, J. Extracting *in Situ* Charge Carrier Diffusion Parameters in Perovskite Solar Cells with Light Modulated Techniques, *ACS Energy Letters*, **2021**, *6*, 2248-2255. DOI: 10.1021/acsenergylett.1c00871, Impact Factor: 23,991

3. Bou, A.; Pockett, A.; Cruanyes, H.; Raptis, D.; Watson, T.; Carnie, M. J.; Bisquert, J. Limited information of impedance spectroscopy about electronic diffusion transport: The case of perovskite solar cells, *APL Materials*, **2022**, *10*, 051104. DOI: 10.1063/5.0087705, Impact Factor: 6,635

4. Bou, A.; Bisquert, J. Impedance Spectroscopy Dynamics of Biological Neural Elements: From Memristors to Neurons and Synapses, *The Journal of Physical Chemistry B*, **2021**, 125, 9934–9949. DOI: 10.1021/acs.jpcb.1c03905, Impact Factor: 3,466

This thesis has been accepted by the co-authors of the publications listed above that have waved the right to present them as a part of another PhD thesis

List of Publications not included in this Thesis

1. Ghahremanirad, E.; Bou, A.; Olyaee, S.; Bisquert, J. Inductive loop in the impedance response of perovskite solar cells explained by surface polarization model, *The Journal of Physical Chemistry Letters*, **2017**, *8*, 1402-1406. DOI: 10.1021/acs.jpclett.7b00415, Impact Factor: 8,709

2. Lopez-Varo, P.; Jiménez-Tejada, J. A.; García-Rosell, M.; Anta, J. A.; Ravishankar, S.; Bou, A.; Bisquert, J. Effects of Ion Distributions on Charge Collection in Perovskite Solar Cells, *ACS Energy Letters*, **2017**, *2*, 1450–1453. DOI: 10.1021/acsenergylett.7b00424, Impact Factor: 12,277

3. García-Rosell, M.; Bou, A.; Jiménez-Tejada, J. A.; Bisquert, J.; Lopez-Varo, P. Analysis of the Influence of Selective Contact Heterojunctions on the Performance of Perovskite Solar Cells, *The Journal of Physical Chemistry C*, **2018**, *122*, 13920–13925. DOI: 10.1021/acs.jpcc.8b01070, Impact Factor: 4,309

4. Guerrero, A.; Bou, A.; Matt, G.; Almora, O.; Heumüller, T.; Garcia-Belmonte, G.; Bisquert, J.; Hou, Y.; Brabec, C. Switching Off Hysteresis in Perovskite Solar Cells by Fine-Tuning Energy Levels of Extraction Layers, *Advanced Energy Materials*, **2018**, 8, 1703376. DOI: 10.1002/aenm.201703376, Impact Factor: 24,884

5. Pham, N. D.; Zhang, C.; Tiong, V. T.; Zhang, S.; Will, G.; Bou, A.; Bisquert, J.; Shaw, P. E.; Du, A.; Wilson, G. J.; Wang, H. Tailoring Crystal Structure of $FA_{0.83}Cs_{0.17}PbI_3$ Perovskite Through Guanidinium Doping for Enhanced Performance and Tunable Hysteresis of Planar Perovskite Solar Cells, *Advanced Functional Materials*, **2019**, 29, 1806479. DOI: 10.1002/adfm.201806479, Impact Factor: 16,836

6. Wang, H.; Guerrero, A.; Bou, A.; Al-Mayouf, A. M.; Bisquert, J. Kinetic and material properties of interfaces governing slow response and long timescale phenomena in perovskite solar cells, *Energy & Environmental Science*, **2019**, 12, 2054-2079. DOI: 10.1039/C9EE00802K, Impact Factor: 30,289

7. Cardenas-Morcoso, D.; Bou, A.; Ravishankar, S.; García-Tecedor, M.; Gimenez, S.; Bisquert, J. Intensity-Modulated Photocurrent Spectroscopy for Solar Energy Conversion Devices: What Does a Negative Value Mean?, *ACS Energy Letters*, **2020**, 5, 187–191. DOI: 10.1021/acsenergylett.9b02555, Impact Factor: 23,101

8. Munoz-Diaz, L.; Rosa, A. J.; Bou, A.; Sánchez, R. S.; Romero, B.; John, R. A.; Kovalenko, M. V.; Guerrero, A.; Bisquert, J. Inductive and Capacitive Hysteresis of Halide Perovskite Solar Cells and Memristors Under Illumination, *Frontiers in Energy Research*, **2022**, 10, 914115. DOI: 10.3389/fenrg.2022.914115, Impact Factor: 3,858

Abstract

Metal-halide perovskites have emerged as a promising semiconductor material for a variety of potential applications. They originated primarily as a new photovoltaic technology with potential to become a candidate to compete with the well-established silicon solar cells, due to their intrinsic properties and their low-cost fabrication methods. In fact, perovskite solar cells have reached efficiencies higher than 25% in just a decade. Their intrinsic properties have enabled the development of new applications such as Light Emitting Diodes (LEDs), Lasers, Ultra-Violet (UV) detectors or memristors. Despite these promising prospects, perovskites still have some issues to solve before they become a commercial technology.

In order to get the most out of perovskite materials, it is indispensable to have a deep understanding of the fundamental operation principles of the devices that we want to optimize. Small perturbation techniques are powerful methods of characterization that have been widely used to investigate device properties of solar cells and electrochemical cells. The most used of such techniques is Impedance Spectroscopy (IS) and although it has been widely used in perovskite solar cells, obtaining the electronic parameters for diffusion and recombination in perovskites has been so far elusive, since the measured spectra do not directly display the diffusion of electrons. In this thesis, we combine IS with other small perturbation methods: Intensity Modulated Photocurrent and Photo-Voltage Spectroscopies (IMPS and IMVS). By using a combination of techniques, we are able to explore the electronic properties of perovskite solar cells. We show that, under conditions of generation of carriers far from the collecting contact, IMPS and IMVS spectra of perovskite solar cells display a high frequency spiralling feature determined by the diffusion-recombination constants. From the high-frequency part of the IMPS spectra we are able to extract the electronic diffusion parameters of perovskite solar cells for the first time with small perturbation methods. We also demonstrate how the values of these constants prevent the diffusion trace from being distinguishable in impedance spectra.

We also present an analysis of memristors and neural systems in the frequency domain by IS. We start from the constitutive equations for the conductance and memory effects, and we derive and classify the IS spectra. We first provide a general analysis of a memristor and demonstrate that this element can be expressed as a combination of simple parts. We derive a basic equivalent circuit for such devices where the memory effect is represented by an RL branch, which has been a repeated feature in perovskite spectra. We show that this model is quite general and describes the inductive/negative capacitance response in halide perovskites and other systems, linking the previous IS studies of perovskite devices to the IS response of memristors. On the basis of these insights, we provide an interpretation of the varied spectra that appear in neuron models such as Hodgkin–Huxley model, to establish the criteria to determine the properties that must be found in a material to be a candidate for neuromorphic computation.

Acknowledgments

First and foremost, I would like to thank my thesis supervisor Prof. Juan Bisquert for his instruction and his guidance during the course of my predoctoral stage. Apart from his deep expertise of semiconductor device physics, his desire to face new challenges and solve new problems in our field, have pushed me in the development of this thesis. His help and support have been essential to achieve our goals.

Dr. Antonio Guerrero has also been a great help during the development of this work. The meetings with him throughout the progress of this thesis have been always a great assistance in both the experimental and the bibliographic work.

I would like to acknowledge Prof. Matt Carnie from Swansea University for hosting me as a visiting PhD Student and ensuring a pleasant stay. He and his team opened the doors of their laboratories to me and allowed me to work with total freedom. Specially, the help of Dr. Adam Pockett during my time in Swansea University was essential both scientifically and personally.

This thesis would not have been possible without the help of several colleagues at the Institute of Advanced Materials (INAM). Prof. Francisco Fabregat-Santiago and Prof. Germà Garcia-Belmonte, who have been always open to debate about the techniques used in this thesis. I also thank Dr. Sandheep Ravishankar for the fruitful discussions while he was at INAM and afterwards, we share a great enthusiasm in the understanding of perovskite solar cells through small perturbation techniques. I thank Prof. Juan A. Jiménez-Tejada and Dr. Pilar López-Varo of Universidad de Granada, for hosting a research visit in their group and ensuring that my stay was pleasant.

In addition, I would like to acknowledge several of my colleagues who have become good friends over the course of this thesis and that have been a great support., Dr. Miguel García Tecedor, Marisé Garcia-Batlle, Cedric Gonzales and Dr. Carlos Echeverría Arrondo have made my predoctoral stage a wonderful time, providing help and support. I am grateful to my best friends, Jose and Carlos, for keeping our strong friendship and to my cousin Vicente for sharing so much together. I would like to thank to my Bachelor friends Juancar, Ponce, Pons and Alba for supporting each other after our undergraduate time.

Finally and most importantly, I would like to dedicate this thesis to my parents, Agustín and Ester, my sister, Cristina and my partner, Noelia who have encouraged me and believed in me unconditionally and who have provided their indispensable love.

Table of Contents

Chapter 1

Introduction

1.1 Thesis style

This thesis is presented in a format as a thesis by publications or by articles. This format consists of a compilation of journal article publications that are divided into chapters that correspond to each one of the publications preceded by a chapter summarizing the objectives of the thesis as well as the state of the art. Chapter 1 involves a review of the literature to present the current state of knowledge in the field and is then followed by a critical overview of the studied research problems and the main results obtained, describing their context, interpretation and significance. Chapters 2-5 contain the full results and conclusions in the form of the author's final version of the manuscript prior to publication, with a preliminary statement of contribution provided before each publication. Finally, a section of general conclusions summarises all the findings and their implications for the current and future understanding of the field.

1.2 State of the art

Global energy consumption has increased continuously over the past decades, and global energy demand is projected to continue to grow for years to come.[1] At the same time, the effects of climate change caused by greenhouse gas emissions from fossil fuels are becoming increasingly apparent. In spite of this, global energy production continues to come from sources that emit these gases in more than 50%.[2] As the world population continues to grow and has reached 8 billion people in 2022,[3] both the energy demand and the resources consumption do not seem to stop increasing. Therefore, urgent measures must be taken to curb the effects of global warming.

Renewable energies and other low emission energy sources must be implemented quickly to achieve the proposed objectives of reducing climate change. The most used renewable energies are hydroelectric power, wind power and solar energy, and the most abundant of these sources is the sunlight. Solar energy can be captured using photovoltaic systems, which transform the energy from solar photons into electricity. In fact, the market of solar photovoltaics is growing year after year.[2] Silicon based solar cells are the main technology dominating the photovoltaic field, with still 95% share of production worldwide.[4] Other technologies present in the market are the thin-film technologies such as CdTe, CzTs or CIGS, however, there has not been any alternative technology able to compete with silicon due to its high efficiency and its low-cost production. While some of the low-cost emerging photovoltaic technologies, such as dye-sensitized and organic solar cells are not able to reach efficiencies close to silicon technologies, highly efficient technologies like GaAs can not compete with the costs of production of silicon.

In this environment, perovskites revolutionized the photovoltaic field since their emergence in the work by Miyasaka et al. in 2009.[5] They were first used as a sensitizer on TiO_2 in a dye-sensitized solar cell, i.e., in an electrochemical cell with an electrolyte. From this first moment, the perovskites proved to be an excellent light absorber and a candidate for photovoltaic technology. However, it was not until 2012 when the perovskite community started spreading thanks to the first all-solid thin film perovskite solar cell, reaching a Power Conversion Efficiency (PCE) of 9,7%.[6] Less than ten years after the first thin film perovskite solar cell, this technology has achieved efficiencies above 25% in single junction solar cells[7] and above 31% in tandem configurations, according to NREL Efficiency Chart, in Figure 1. Perovskites have demonstrated that they can be a good alternative to silicon technologies with their rapid development.

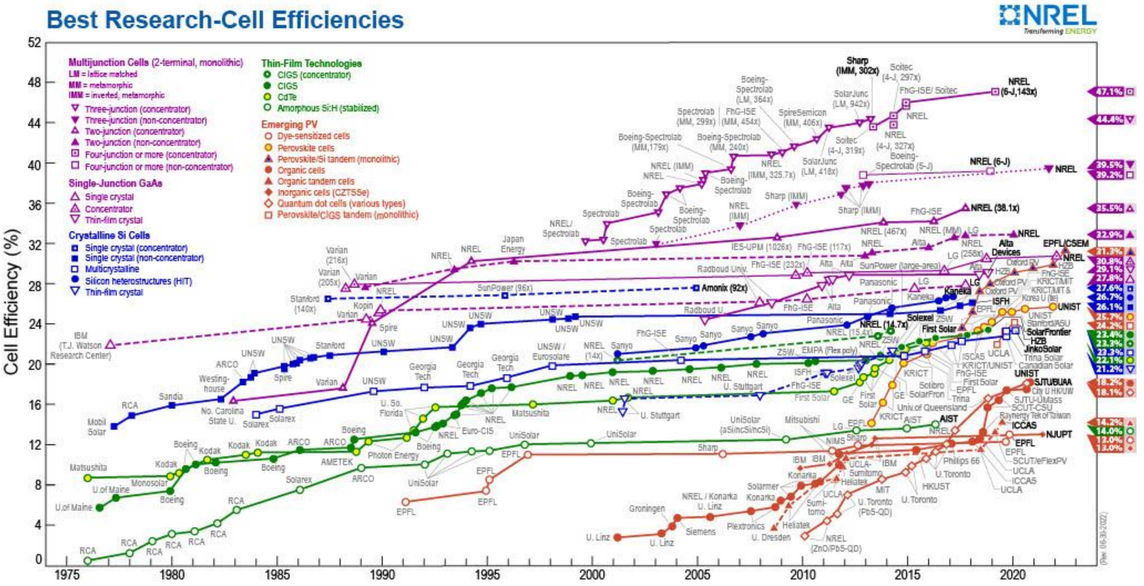

Figure 1. Evolution of efficiencies of several photovoltaic technologies. The circle highlights the efficiency rise of perovskite solar cells. Data obtained from National renewable energy laboratory (NREL), https://www.nrel.gov/pv/cell-efficiency.html.

Perovskites originated as a hybrid organic-inorganic material that satisfy the chemical formula ABX_3, where the A is usually an organic molecule (such as methylammonium or formamidinium), B is a metallic cation (such as Pb^{2+} or Sn^{2+}) and X is a halide anion (such as I^- or Br^-). An example of perovskite structure is shown in Figure 2. Nevertheless, all inorganic compositions have also been proposed where the A organic cation has been substituted by inorganic cations such as Cs^+.[8] In addition to the high PCEs achieved, another factor that makes perovskites a suitable candidate for solar cells commercialization is their low cost production and the abundance of the precursors.[9] In fact, the most common fabrication methods in laboratories are solution processed low-temperature methods, which require neither expensive equipment nor a long time. Besides, some of those methods are scalable and familiar to industry.[10, 11]

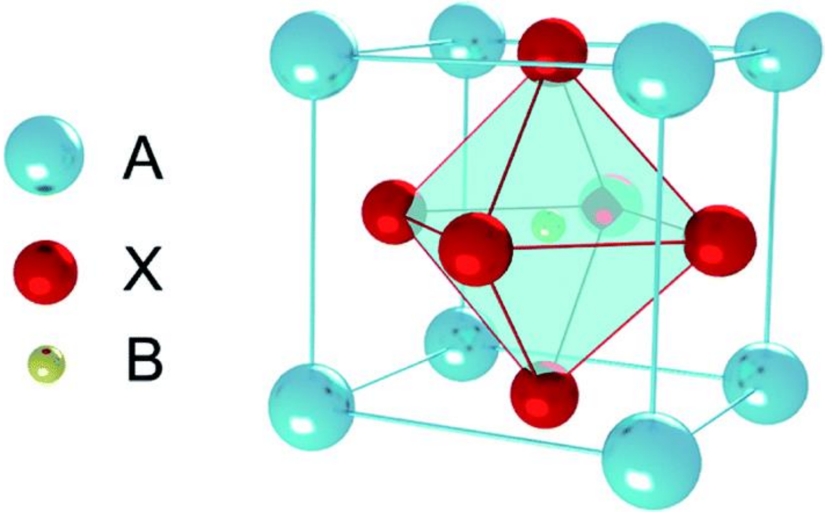

Figure 2. Structure of a ABX_3 perovskite. Reproduced from Ref. [11], licensed by CC BY 3.0, https://creativecommons.org/licenses/by/3.0/.

The chance to use different compositions of the same chemical formula comes with another benefit, since the changes in, e.g., the halide anion X, cause a shift in the band gap of the material. Therefore, the band gap of perovskites is tunable by only changing the stoichiometry of the perovskite.[12] This possibility comes with a number of good opportunities. Regarding solar cell applications, the band gap of the material is of real importance. First, the Shockley-Queisser limit, which depends on the band gap of the material, indicates which band gaps are most suitable for high efficiency solar cells.[13] Second, when building a tandem solar cell, the combination of two or more semiconductor materials must be optimized to get the maximum absorption from the solar spectrum.[14] In Figure 3, we can see the band gap for the most relevant photovoltaic technologies with their theoretical limit.[15]

Moreover, this characteristic opened the door to other applications, such as Light-Emitting Diodes (LEDs)[16, 17] and Lasers[18] with a wide range of wavelengths. Recently, perovskites with a wide band gap have been also used as UV-detectors.[19] Memristors are another alternative application that has been recently explored,[20, 21] proving the versatility of this materials and opening their perspectives.

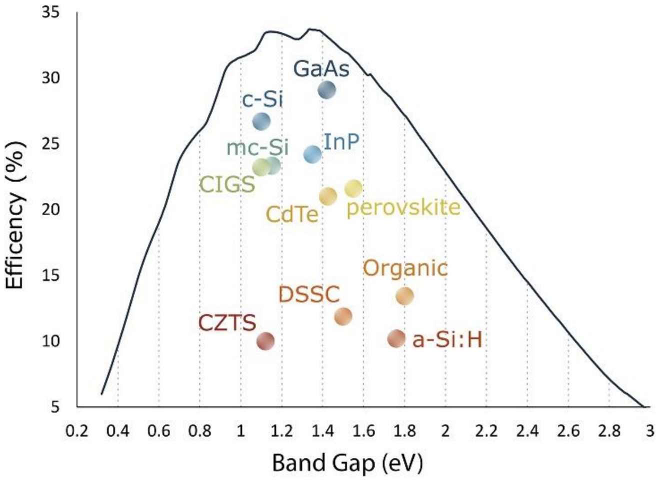

Figure 3. Efficiency for Different Band Gap Materials. Solid line represents the radiative power conversion efficiency limit for single-junction photovoltaics under AM 1.5 illumination as per the Shockley–Queisser limit. Circles correspond to present record efficiency reports for various types of solar cells at active areas greater than or equal to 1 cm^2. Reproduced with permission from ref. [15]. © 2020 Published by Elsevier Inc.

Perovskites have a number of both optical and electrical characteristics that have led them to such a successful growth in the number of both the applications and the efficiency improvement. First, they have a high absorption coefficient, which permits the absorption of the full incident solar spectrum in a few hundred nanometers.[22] The loss in non-radiative recombination losses can be sorted out by minimizing defects in perovskite layers towards the radiative limit.[23] Electronically, perovskites show a good ambipolar carrier transport, having both a high charge carrier mobility and a long diffusion length.[24]

In contrast, perovskite have shown some issues regarding the stability of their performance, and it is that these materials present an unusual characteristic that has led to some difficulties in manufacturing stable solar cells.[25] This characteristic is the intrinsic ionic conductivity of perovskite materials.[26, 27] In the first years of perovskite solar cells development, this characteristic was manifested by means of the dynamic hysteresis of the current-voltage curves.[28-30] Figure 4 shows a variety of the types of hysteresis observed in perovskite solar cells. This hysteresis led to problems in the reliability of performance measurements of perovskite solar cells since the efficiency of solar cells is extracted from current-voltage curves.[31] Therefore, the efficiencies of perovskite solar cells could vary depending on the scan-direction, the scan-rate or the pre-treatment of the solar cell by both voltage and light application. The efforts of the scientific community have solved the hysteresis problems by the optimization of both the perovskite layer and the selective contacts. However, the ionic conductivity is still present in perovskites and it manifests in other ways, such as inductive behaviors.[32] In fact, this combined electronic-ionic conductivity which is problematic for some applications can be a desirable characteristic when using perovskites for building memristors instead of solar cells, since some perovskite devices show similar impedance behavior as theoretical memristors and neurons.[33]

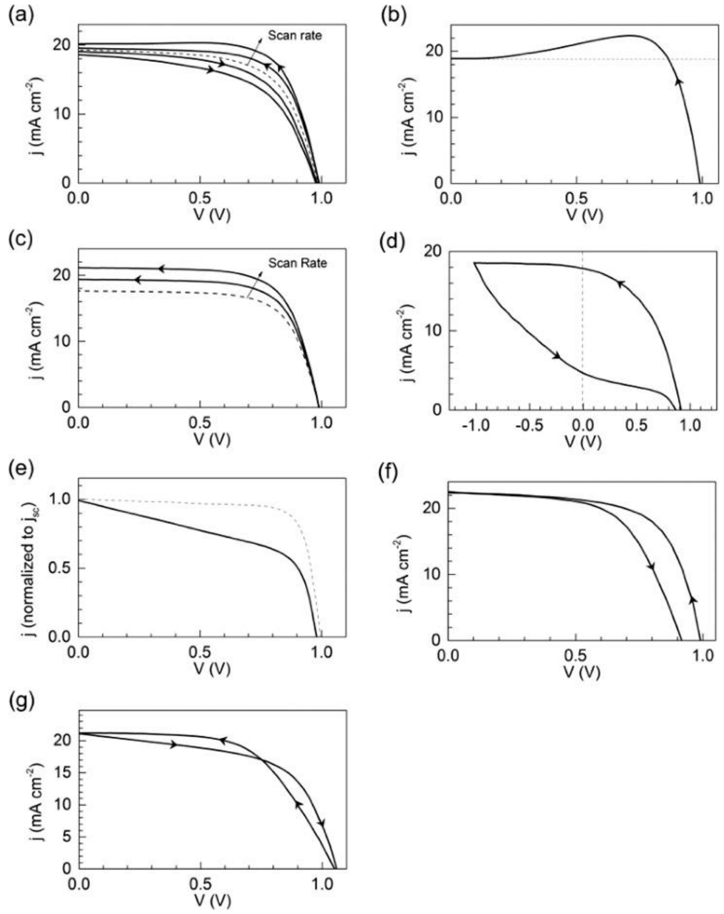

Figure 4. Characteristic patterns of hysteresis behavior in perovskite solar cells. The large arrows on the solid black lines indicate the scan sense. The black dashed lines show the steady-state curve (a, c). In panels b and d, the auxiliary dashed lines signal j_{sc} and zero applied bias respectively, while in panel e, it represents a typical diode curve. Reproduced with permission from ref. [30]. Copyright © 2016, American Chemical Society.

In order to address perovskite device issues such as energy conversion efficiency, stability of operation, current-voltage responses or emission/absorption performances we need to understand the internal operation of such material both electronically and ionically. The characterization by current-voltage curves gives a direct value of current for each given voltage without revealing mechanisms such as charge transport, recombination or polarization. We believe that the characterization by Impedance Spectroscopy (IS) is more adequate to understand the operation of perovskite devices, since it permits measuring at a given point of voltage and applying a small perturbation of voltage around this point, as shown in Figure 5, to extract the current response at a wide range of frequencies from the MHz to the mHz scale. Therefore, the mechanisms occurring at different time-scales can be separated and some phenomena that are not visible in the current-voltage curves can be uncovered. The analysis of IS data is done by looking at both the real value and the phase of the generated IS transfer function. While the real values are related to resistances inside the devices, i.e., voltage drops caused by recombination or transport, the phase lags are related to capacitive behaviours related to polarization at interfaces or the bulk. Therefore, the study of IS response is carried out by constructing an equivalent circuit with the same amount of resistive and/or capacitive elements as those given by the IS data of a device and then extract the resistor and capacitor values.[34] One thing that complicates the successful understanding of IS is the fact that different equivalent circuits can give the same response, so it is important to give a good interpretation of the selected equivalent circuit. As mentioned earlier, the IS can be measured at different points of voltage. By measuring along the current-voltage curve points, we obtain the values of those resistors and capacitors against the voltage, and we can explore what the meaning of those elements are.[35] For example, a series resistance or a geometrical capacitance will not depend on voltage, while a recombination resistance and an interfacial capacitance will depend exponentially. From those capacitances and resistances, we can extract physical parameters such as doping densities[36] or recombination lifetimes.[37]

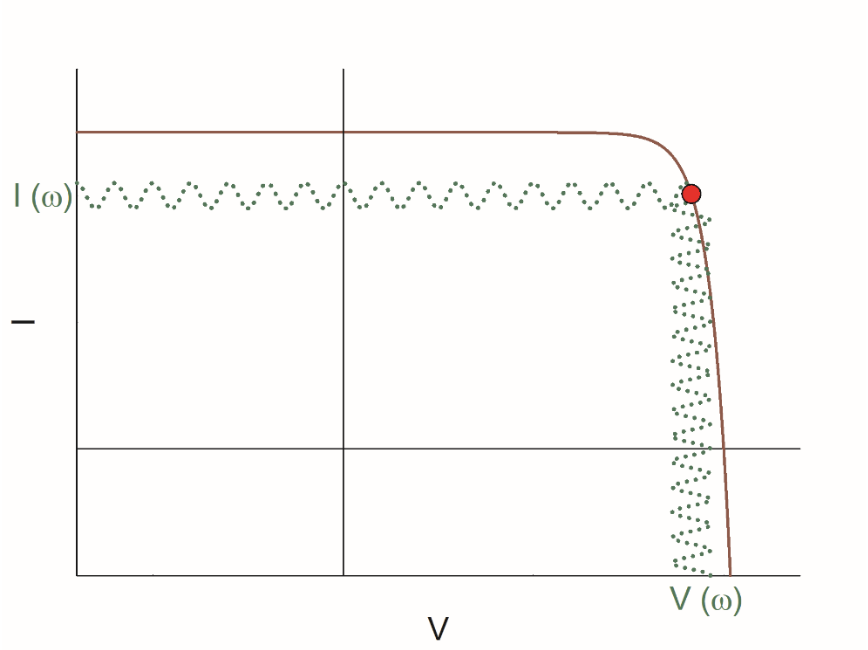

Figure 5. Schematic representation of the voltage and current oscillations at a given point of a current-voltage curve carried out in an IS measurement.

Nevertheless, the analysis of IS that was so successful in devices such as organic[38] or dye-sensitized[39] solar cells has been elusive in perovskite solar cells. In fact, after several years of debate, there are still a variety of exotic responses of perovskite solar cells that are not clearly understood. The difficulty of the interpretation of IS of perovskite solar cells is more than likely caused by the complexity of mixed ionic-electronic phenomena. In certain configurations and dark conditions, the ionic diffusion has been obtained in perovskite single crystals.[40] This is shown in Figure 6a, where the diffusion of ions is extracted via a transmission line in a finite layer. The most repeated IS spectra found in perovskite solar cells is shown in Figure 6b.[41] It is formed by two arcs in the complex plane plot that vary with voltage accordingly. From these spectra, two resistances and two capacitances can be extracted. The resistances at high and at low frequencies are mainly linked with recombination phenomena since they vary equally with voltage. They are attributed to bulk recombination[42] and surface recombination,[41] respectively, due to the capacitance they have in parallel. The high frequency capacitance is the dielectric capacitance and does not depend on voltage. The low frequency capacitance is related to interfacial polarization and has a strong dependence with voltage and illumination.[43] Although the interpretation of these two arcs is well established, there is another phenomenon which interpretation is not straight away: the so-called inductive loop or negative capacitance,[44] which is discussed later. We can observe two examples of the inductive behaviours in Figures 6c[45] and 6d.[32] Moreover, in some cases, there appears a third arc at intermediate frequencies which would add complexity to the interpretation of IS of perovskite solar cells.[46] Figure 6 represents the difficulty to find a unique equivalent circuit to evaluate and interpret the IS response of perovskite solar cells.

Solar cells and related devices have three main variables that are important to determine their performance. These magnitudes are the illumination or light intensity, the applied voltage and the extracted current. In fact, the current-voltage curves, which are used to determine the solar cell efficiencies, are dependent on these three variables (see Figure 7). For a given illumination, we will have a given current-voltage curve, and if we change the light intensity, we will get a different curve. The IS considers only two of these variables. Although we can measure IS at different light intensities, the illumination remains constant during the whole measurement. Therefore, we aim to get a broader picture about the operation of perovskite devices by using similar techniques which include the third variable, the light intensity, to get the electronic properties of perovskites that so far had not been obtained.

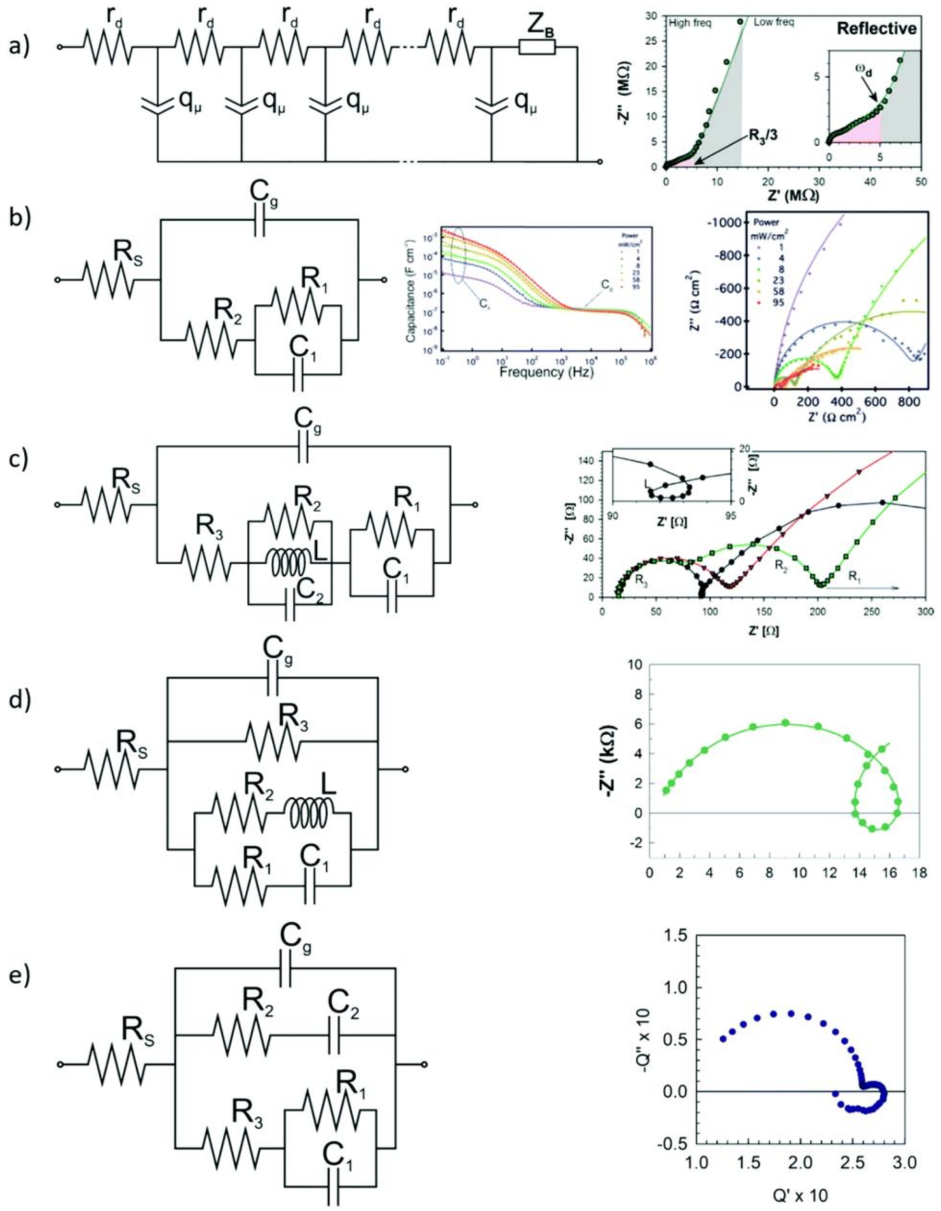

Figure 6. Summary of equivalent circuits used for the analysis of impedance spectra of perovskite solar cells with examples of representative spectra for each circuit. (a) Transmission line showing the impedance of ion diffusion in a finite layer used for ionic transport quantification in perovskites, highlighted in red. (b) Equivalent circuit used for two arc spectra. Here we show capacitance spectra depending on light intensity. (c) Equivalent circuit used for three arc spectra and intermediate frequency loops; here, resistances appear in series. d) Equivalent circuit used for spectra with two arcs that vary in concordance which have exotic features such as inductive loops or negative capacitances; here, resistances appear in parallel. (e) Equivalent circuit obtained from the analysis of both IS and IMPS data together; here we have resistances in parallel as well as in series. Reproduced from ref. [47] with permission from the Royal Society of Chemistry.

As we have already mentioned, IS consists of applying a small voltage perturbation to the sample, to measure the perturbed extracted current through a range of different frequency orders of magnitude while the illumination remains constant. The techniques that we combine with IS follow a similar scheme. We maintain constant one of the three variables, while we apply a small perturbation to another one and we measure the response of the third one. The techniques that we have used throughout this thesis are Intensity-Modulated Photocurrent Spectroscopy (IMPS) and Intensity-Modulated photo-Voltage Spectroscopy (IMVS). Both techniques have in common that the perturbation is applied to the light intensity. In IMPS, the response is measured in the extracted current while the voltage remains constant. Oppositely, in IMVS the extracted current remains constant, and we measure the voltage response at the contacts.

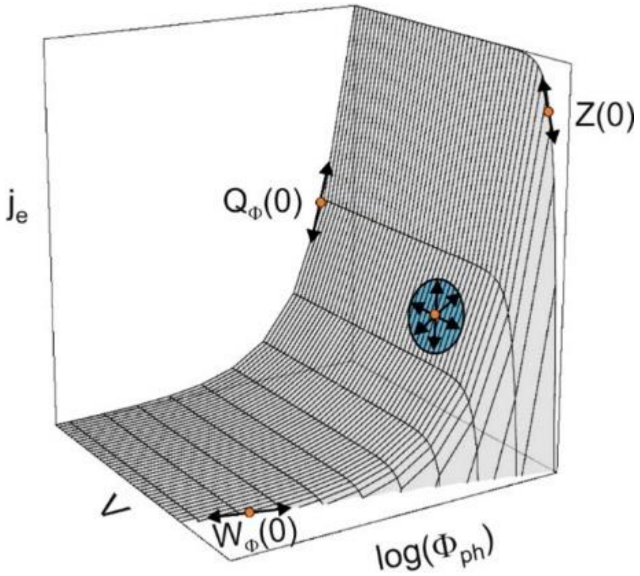

Figure 7. Steady-state performance of a solar energy conversion device in terms of electrical current j_e, voltage V, and illumination flux Φ_{ph}. When these variables are taken in pairs, the slope of the curve is given by the zero frequency value of the transfer functions. In the figure, slopes are shown in the main 2D planes, but the same analysis can be performed at any point of the surface (when the three variables are not zero), as indicated by the circular tangent plane. Reproduced with permission from ref. [48]. Copyright © 2017, American Chemical Society.

The technique of IMPS has been widely used for the investigation of the operation of planar semiconductor-electrolyte interfaces.[49, 50] Later, the technique was used to investigate the transport and recombination of electronic charges in mesoporous layers of dye-sensitized solar cells.[51-53] IMPS has also been used for the characterization of perovskite solar cells, as seen in Figure 8.[54, 55] Although it has given important information about the External Quantum Efficiency (EQE),[56] it has not been useful for the study of electronic parameters of perovskite devices.

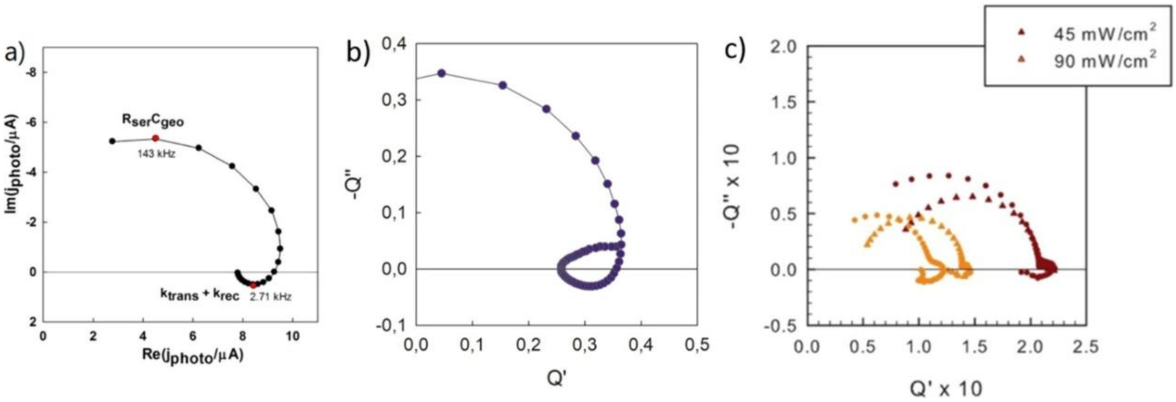

Figure 8. IMPS response for PSCs indicating an excursion to the second quadrant in the case of a and b and staying in the first quadrant for c. Reproduced with permission from ref. [57]. Copyright © 2021 American Chemical Society.

To define the IMPS transfer function, we may take the light intensity in terms of photon flux and convert it to a pseudo-current by multiplying the photon flux Φ by the electronic charge q. In that case, we can define the IMPS transfer function Q as:

$$Q(\omega) = \frac{\hat{j_e}}{q\hat{\Phi}} \tag{1}$$

where j_e is the extracted current and the circumflex is for small perturbations. This definition of the IMPS transfer function leads to a dimensionless magnitude Q that, as it has been discussed in the literature, can be used for the calculation of the External Quantum Efficiency (EQE).[56] In fact, it is important to ensure that the EQE measurements when using AC perturbations are not dependent on the frequency and IMPS can be a useful method to check this effect. Figure 9 shows how the EQE measurements are frequency dependent and the IMPS real part follows a similar trend.

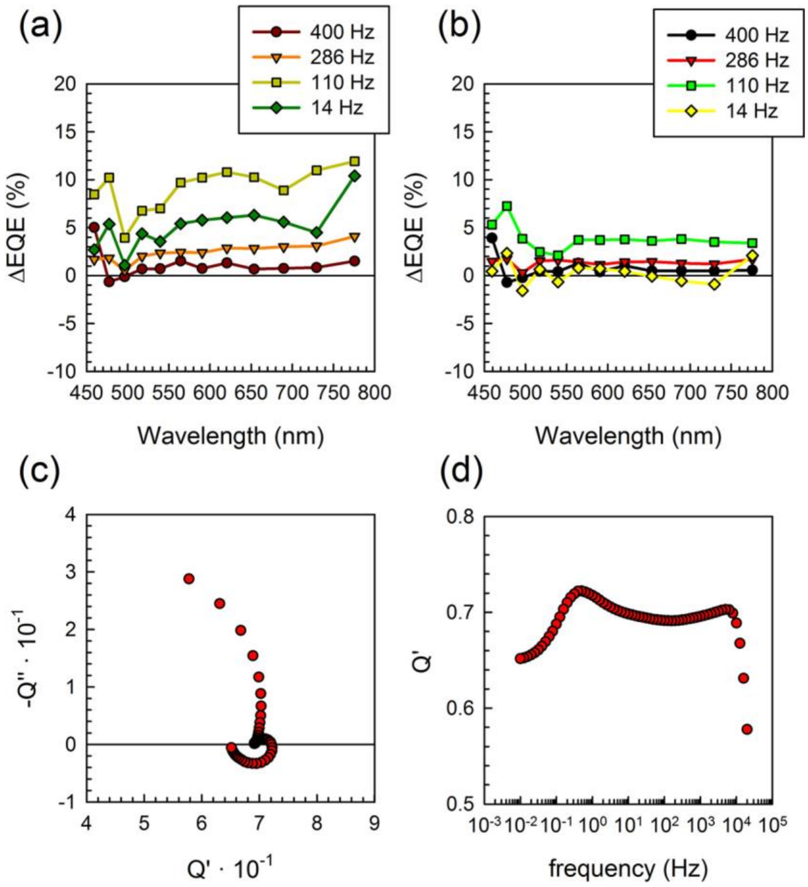

Figure 9. Variation in EQE at (a) 0 DC white light bias and (b) 10 mW·cm^{-2} DC white light bias for different optical chopper frequencies with respect to spectra measured at 500 Hz. (c) IMPS spectra measured at 33 mA·cm^{-2} DC blue light bias and (d) evolution of the real part of the IMPS transfer function versus frequency at 470 nm. Reproduced with permission from ref. [56]. Copyright © 2018, American Chemical Society.

Otherwise, IMVS is a technique mainly used to investigate the recombination mechanisms in photovoltaic systems.[58-60] This method has also been used for the study of other electrochemical systems.[61] IMVS has also been applied to perovskite solar cells.[54] In fact, a study by Pockett et al. demonstrated that, in the same way as IMPS, IMVS transfer function of perovskite solar cells could uncover an intermediate frequency feature which was not present in IS.[62]

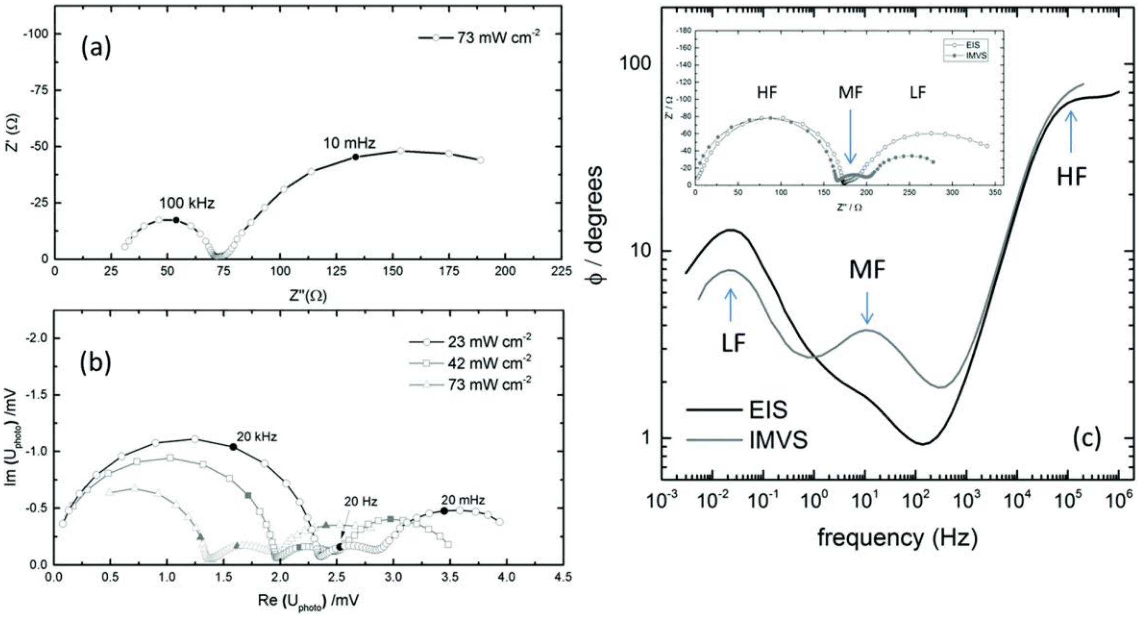

Figure 10. (a) Nyquist plot showing EIS at 73 mW cm^{-2}; (b) IMVS at three different light intensities; (c) Bode plot showing a comparison of EIS and IMVS, where the IMVS has been converted by dividing by the ac photocurrent at VOC obtained using an IMPS measurement. Inset shows the corresponding Nyquist plot. Reproduced from ref. [62] with permission from the Royal Society of Chemistry.

If we use the same photocurrent that we defined for the IMPS transfer function, the definition of the IMVS transfer function W is:

$$W(\omega) = -\frac{\hat{V}}{q\hat{\Phi}} \tag{2}$$

where V is the voltage at the contacts. Thereby, W has units of impedance and, in the same way as IS, the real part of IMVS transfer function corresponds to resistive mechanisms. Therefore, the comparison between IS and IMVS is direct, since they have the same dimensions.

1.3 Critical overview

The work of this thesis started with the aim of understanding the mechanisms of perovskite solar cells via IS experiments and an exhaustive drift-diffusion modelling of the structure of a full device, including the perovskite active layer, the Electron Transporting Layer (ETL) and the Hole Transporting Layer (HTL). This drift-diffusion model included the influence of mobile ions inside the perovskite layer, as well as the electronic effects of the heterojunction interfaces.[63] The intended approach of this strategy was to understand the distribution of charge carriers inside the perovskite layer, as well as the distribution of mobile ions, to understand how this distribution would affect the accumulation of charge in the interfaces,[64] and correlate this simulations with the capacitance values extracted from IS measurements.

The advances in the understanding of perovskite/ETL and perovskite/HTL interfaces were fruitful, and we got to understand in which conditions the ionic charges accumulated in the interfaces and which conditions were more favorable for a distributed allocation of mobile ions. Specifically, we were able to correlate the occurrence of hysteresis in perovskite solar cells with the band alignment of perovskite layer and HTL.[65] The accumulated charge depending on perovskite/HTL alignment is outlined in Figure 11.

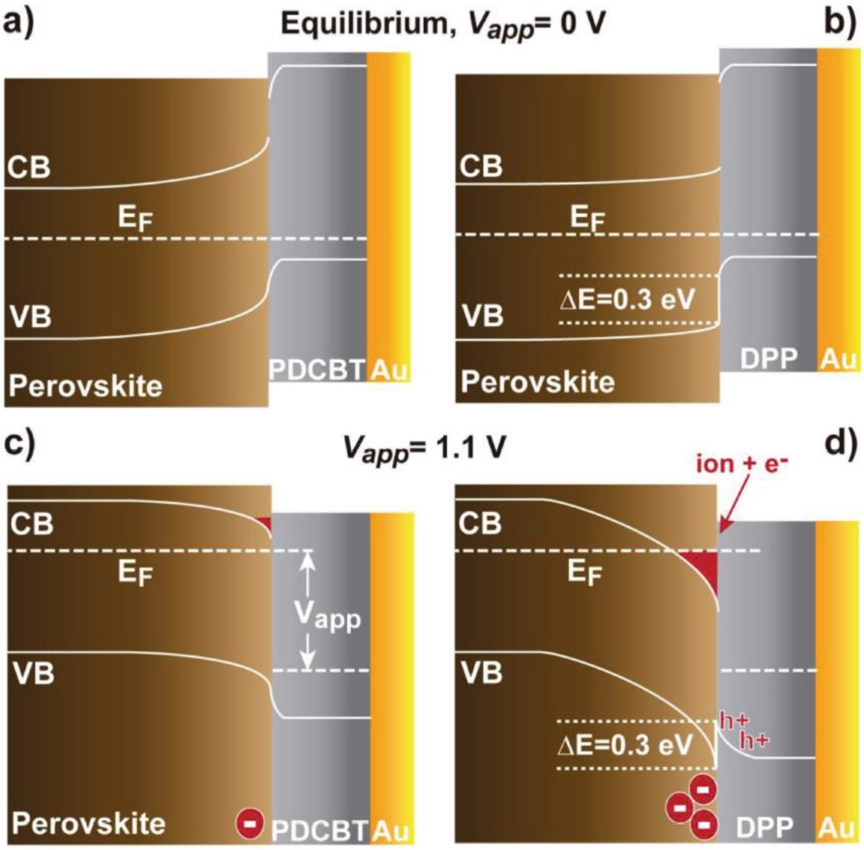

Figure 11. Band diagram scheme of a simulated perovskite/HTL interface in the dark. a,b) At equilibrium conditions Vapp = 0 V and c,d) under applied voltage bias of 1.1 V. a,c) A perovskite/PDCBT interface with energy level alignment of valence band of perovskite with HOMO level of HTL when no hysteresis is observed. b,d) A perovskite/DPP interface represents a system with and energy level offset of 0.3 V that shows strong hysteretic behavior. Reproduced with permission from ref. [65]. © 2018 WILEY-VCH Verlag GmbH & Co. KGaA, Weinheim.

At the same time, we were able to go forward in the understanding of the IS response of perovskite solar cells and its exotic features. Many advances were being developed in the understanding of perovskite solar cells hysteresis.[30, 66-68] However, the proposed mechanisms were varied and different. Hysteresis could be attributed to trapping and de-trapping processes; however, the timescales of perovskite hysteresis were too large and such hypothesis were unrealistic. Ferroelectric mechanisms were also proposed, but they have been later discarded by several studies,[69, 70] and their contribution to hysteresis, too.[71] Finally, the most cited cause for hysteresis in perovskite solar cells is ionic mobility,[27, 54, 71-75] but it is not clear how they exactly affect the current-voltage measurements. Some of these reports advocate for the screening of the electric field,[74] while others suggest an accumulation of interfacial ionic charge that affect the operation of the solar cell.[43, 73] Ravishankar et. al set up a model for the dynamic hysteresis of perovskite solar cells, named "Surface Polarization Model", that was able to reproduce hysteretic trends thanks to the introduction of an internal voltage.[30] This internal voltage is induced by the surface polarization of accumulated ions at the interfaces, and follows the applied external voltage according to a relaxation equation as follows:

$$\frac{\mathrm{d}V_S}{\mathrm{d}t} = -\frac{V_S-(V-V_{bi})}{\tau_{kin}} \tag{3}$$

Based on this approach, we calculated the response of such model to small perturbations of voltage, and we derived the IS transfer function that it generated. From the result of the transfer function, we were able to derive an equivalent circuit that generated the responses of the Surface Polarization Model. This equivalent circuit, shown in Figure 12a, contains an inductive element. The inductor had been an element added in the equivalent circuits used to evaluate the IS data of perovskite solar cells that contained data points going into the fourth quadrant. However, there had not been any explanation for the use of an inductive element apart from the need to fit the IS experiments. For the first time, an inductive element emerged directly from a model, giving significance to it. It appears that the delayed time of the surface voltage V_S to get to its steady-state value is the responsible for the inductor. In fact, equation 3 has served as inspiration for models for hysteresis of perovskite memristors as well as the IS response of such devices.[76-79]

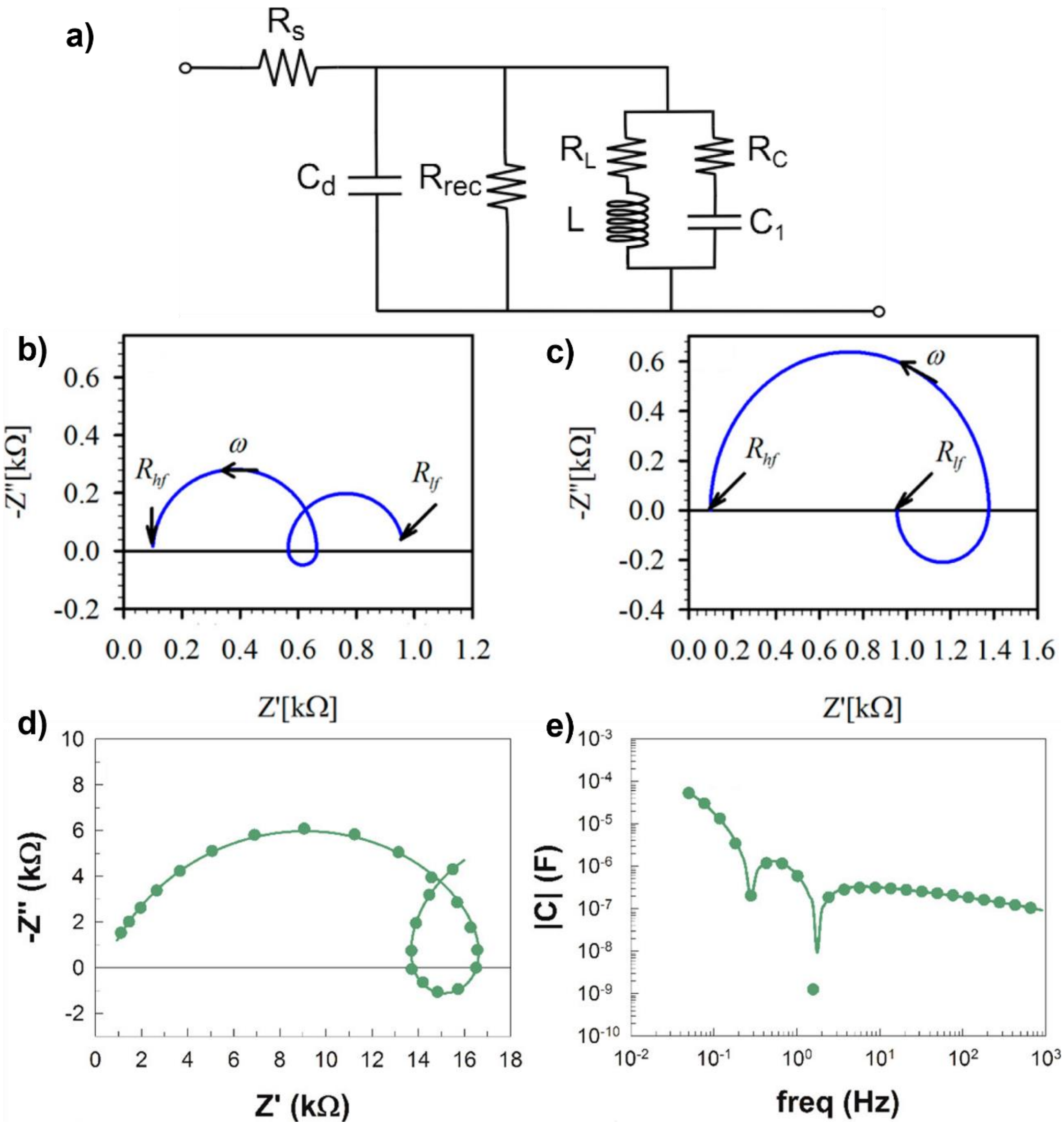

Figure 12. a) Equivalent circuit generated by the Surface Polarization Model. b,c) Complex plane plots of the IS response of the equivalent circuit in (a) going into the fourth quadrant. d) Impedance complex plane plot from experimental data of a perovskite solar cell (points), fitted with the equivalent circuit in (a) and e) bode plot for the capacitance corresponding to (d). Adapted with permission from ref. [32]. Copyright © 2017, American Chemical Society.

From the equivalent circuit in Figure 12a, we were able to generate IS spectra that reproduced the exotic shapes of experimental IS data going into the fourth quadrant, as well as more common the two arc spectra, depending on the values of the kinetic characteristic time τ_{kin} from Equation 3. Two examples of such spectra are shown in Figures 12b and 12c. Moreover, we got satisfactory fittings of experimental data from perovskite solar cells showing the inductive loops in the IS complex plane plots, as in Figure 12d. In Figure 12e, we can see how this feature manifests in the bode plot of capacitance vs. frequency, spiking at the frequencies where the real axis of the complex plane plot is crossed.

The inductive loop in perovskite solar cells is more than likely caused by the ionic conductivity of such material. The fact that it appears in the low frequency region of IS measurements points in that direction, since the electronic mechanisms such as diffusion, transport, extraction and recombination are orders of magnitude faster than those of the characteristic time of the inductive loop. Therefore, the comprehension of such phenomenon and the models for this feature can help understand how the ions affect the internal operation of perovskite devices. From that initial model, we can understand that there exists an internal voltage led by the mobile ions that follows the applied external voltage through a relaxation equation that has a characteristic kinetic time constant.

Despite the advances in both the device modelling and the IS of perovskites, the efforts to obtain electronic parameters for the operation of perovskite solar cells did not pay off, and other alternatives had to be sought. Inspired by the works of Pockett et al.[62] and Ravishankar et al.[55] where additional features were found in IMVS or IMPS spectra in contrast with IS spectra of perovskite solar cells as in Figures 6e and 10, we aim to investigate the response of the three techniques in such devices and see how the transfer functions are related.

For that purpose, we have chosen a particular configuration of perovskite solar cells, which are carbon-based perovskite solar cells. These solar cells are very promising for a future commercialization due to their scalable method of fabrication (screen printing) and the low cost of production through the absence of expensive HTL.[80] Although the efficiencies mesoporous solar cells are not as high as those of the planar perovskite solar cells, they show an outstanding stability in comparison, sorting out one of the most important drawbacks of perovskite devices.[81]

Both the applications regarding solar cells and the perovskite memristors are of the interest of this thesis, and therefore understanding the electronic and the ionic mechanisms that affect the operation of these devices is key for the optimization of their performance and for troubleshooting. The experimental tools used here are frequency dependent, small perturbation methods. This type of methods allows the separation of phenomena occurring at different time scales and, therefore, the analysis of these phenomena can be treated independently. Our approach is based on the calculation of the responses of both voltage and light modulated techniques using theoretical models. We classify the given responses depending on the parameters of the models and we estimate the values of the perovskite devices by comparing the experimental response with the theory. The fitting of the experimental data with theoretical models can give key parameters for the operation of devices.

The main objective is to understand the response of perovskite devices to small perturbation techniques as well as the relation between these responses. Through the comparison of the responses of the three mentioned techniques (IS, IMPS and IMVS) we get a broader picture of electronic and ionic phenomena within perovskites than what we had only with IS. Our investigation has made it possible to link the mid-frequency spectral characteristics with the perovskite layer thickness. It has demonstrated that the hidden charge carrier diffusion of perovskites in IS measurements is observable in IMPS measurements and, in fact, it can be extracted by proper modeling. Moreover, we further explain how diffusion manifests both in IMVS and IMPS but in IS, and we find the factor that uncovers the trace of diffusion. These discoveries are collected in the first three chapters of this thesis.

In the first work, we carried out the measurements of the three techniques on three different groups of carbon-based perovskite solar cells. These groups of solar cells are identical in their configuration, with the same kind of perovskite material and contacts. The only change between these groups is the perovskite layer thickness. This small change allows for a controlled basis for analyzing the effects of perovskite thickness on IS, IMPS and IMVS spectra. Since one of our goals is to compare the results of the three experiments, we made the three measurements under the same conditions of steady-state voltage and illumination. Specifically, we carried out the measurements at open-circuit voltage (IMVS) conditions or applying the open-circuit voltage (IS and IMPS).

From our first observations on the three techniques, we could see how the IMPS spectra spiral around the four quadrants at the highest frequencies, although we still could not give an explanation to this feature. The spectra of the three techniques have a several number of arcs in both first and fourth quadrants, but only IMPS went to the negative side of the real part. In fact, we believed this spiraling loop at high frequencies was an artefact of the measurement, and the spectra shown in the original publication do not show the negative side of the spectra. Here, in Figure 13, we show the full spectra of IMPS crossing the four quadrants in the three cases. Later on, we realized those were not a problem of the measurement, but a real feature of this kind of perovskite solar cells.

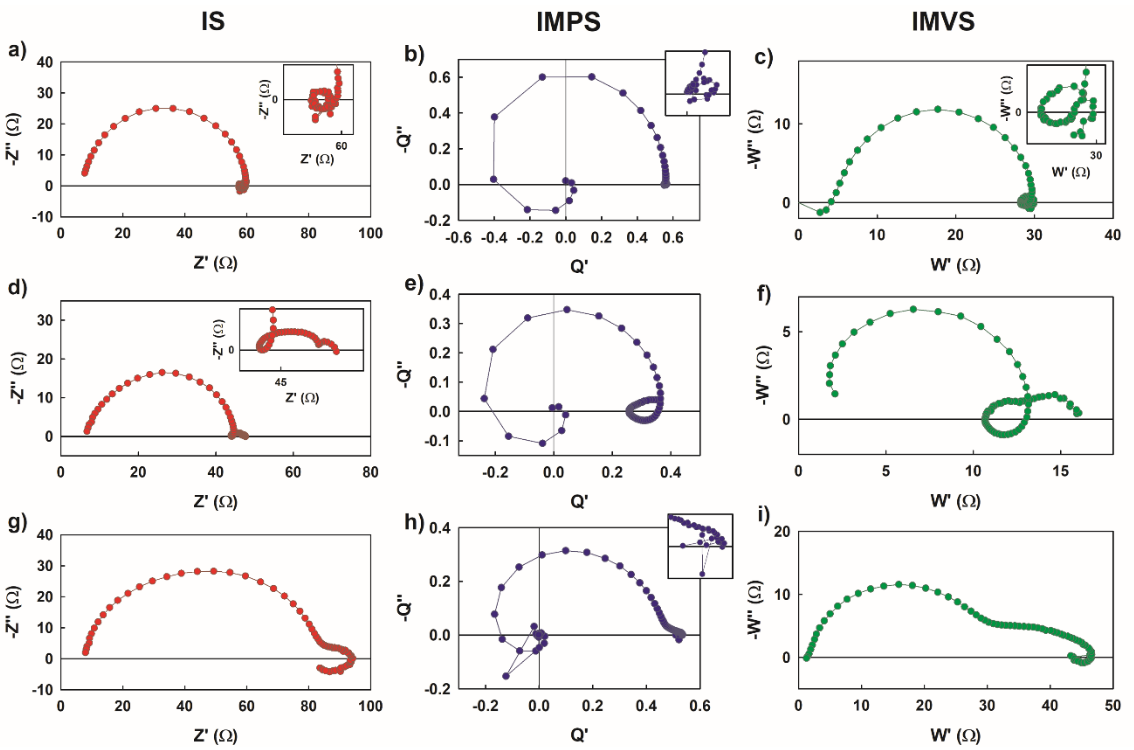

Figure 13. Complex plane plots of the IS (red), IMPS (blue), and IMVS (green) transfer functions (Z, Q, and W, respectively) for the three devices measured under 0.1 sun of illumination, for a frequency range of 1 MHz to 0.01 Hz and at open circuit voltage. (a–c) are the spectra for Cell 1 (normal perovskite layer thickness); (d–f) are the spectra for Cell 2 (double perovskite layer thickness); and (g–i) are the spectra for Cell 3 (triple perovskite layer thickness). Adapted with permission from ref. [82]. Copyright © 2020 American Chemical Society.

Although we were not able to give an explanation to these features yet, we managed to get an equivalent circuit able to fit the IS data. The existence of inductive features required using an inductive element in the equivalent circuit. Moreover, the IS spectra showed up to three arcs in the first quadrant, thus requiring the insertion of three capacitances. For the placement of the third capacitance, we relied on the work made by Ravishankar et al., where they introduced a mid-frequency capacitor in order to explain the additional feature that they found in IMPS measurements.[55, 83] For the inductive element, we followed the aforementioned Surface Polarization Model to introduce a Resistor-Inductor (R-L) additional branch. The equivalent circuit that we built can be seen in Figure 14, accompanied with some examples of fitted spectra of the three types of carbon-based perovskite solar cells.

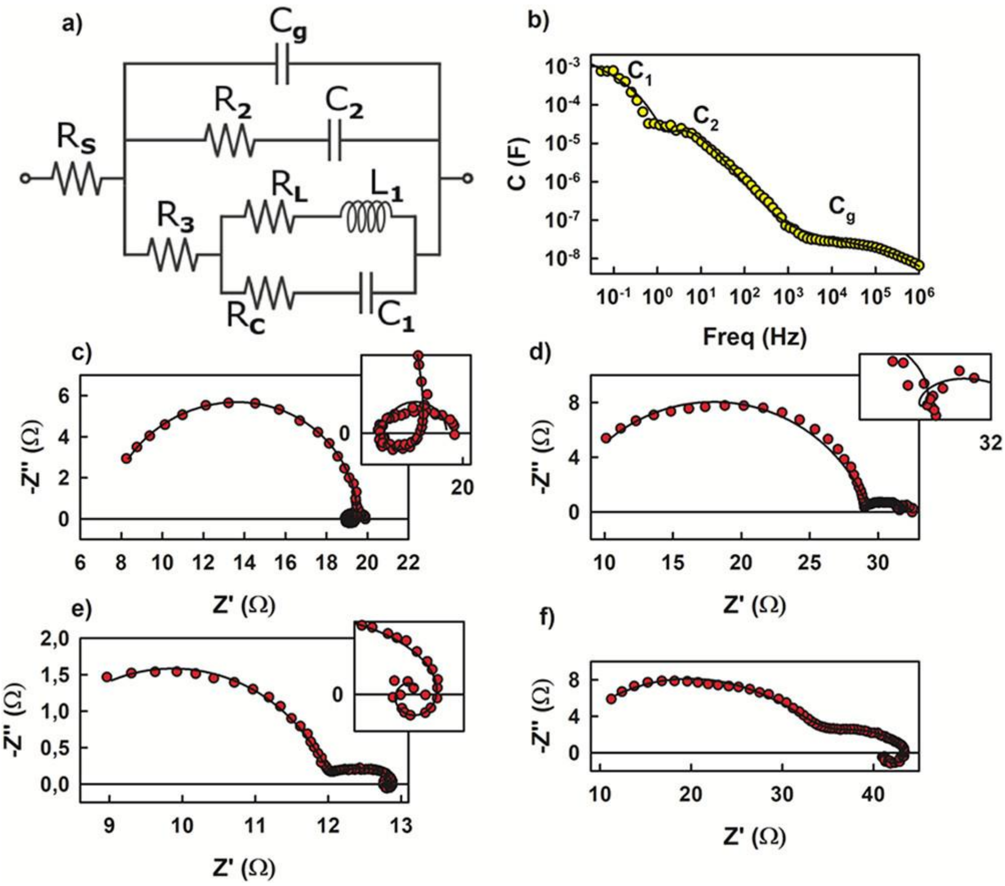

Figure 14. (a) Equivalent circuit for the data fitting of IS of carbon-based perovskite solar cells. (b) Capacitance–frequency plot of Cell 2 showing three capacitances at different frequencies. (d–f) Impedance complex plots at open circuit conditions. Red and yellow points are experimental data, and the straight black line is the fitting given by the EC. (c) is for Cell 1, (d,e) are for Cell 2, and (f) is for Cell 3. Reproduced with permission from ref. [82]. Copyright © 2020 American Chemical Society.

From the fitting results, we could conclude that the perovskite layer thickness affects mainly the mid-frequency part of the IS spectra, by increasing the mid-frequency capacitance. We also demonstrate experimentally the theoretical relation between the transfer functions of the three techniques, that was previously proposed by Bertoluzzi et al.,[48] by the formula:

$$Z(\omega) = \frac{W(\omega)}{Q(\omega)} \tag{4}$$

After such results and thanks to exhaustive work by Pockett and collaborators, they made a study about the IMPS and IMVS spiraling through the four quadrants.[84] In this work, they designed a custom-built system to measure both IMPS and IMVS, in order to avoid any artifacts of the commercial systems that have limitations at high frequency ranges. In fact, they did not only measure both techniques, but supplemented these measurements with Transient Photo-Current (TPC) and Transient Photo-Voltage (TPV) experiments. Therefore, they were able to link the results of the time-dependent measurements (TPC and TPV) with the frequency-dependent experiments (IMPS and IMVS, respectively).

Specifically, they were able to match the evolution of the high frequency value of the negative real part of the IMPS and IMVS transfer functions with the change in the short-time negative spike of TPC and TPV measurements, respectively. We can see this phenomenon in Figure 15.

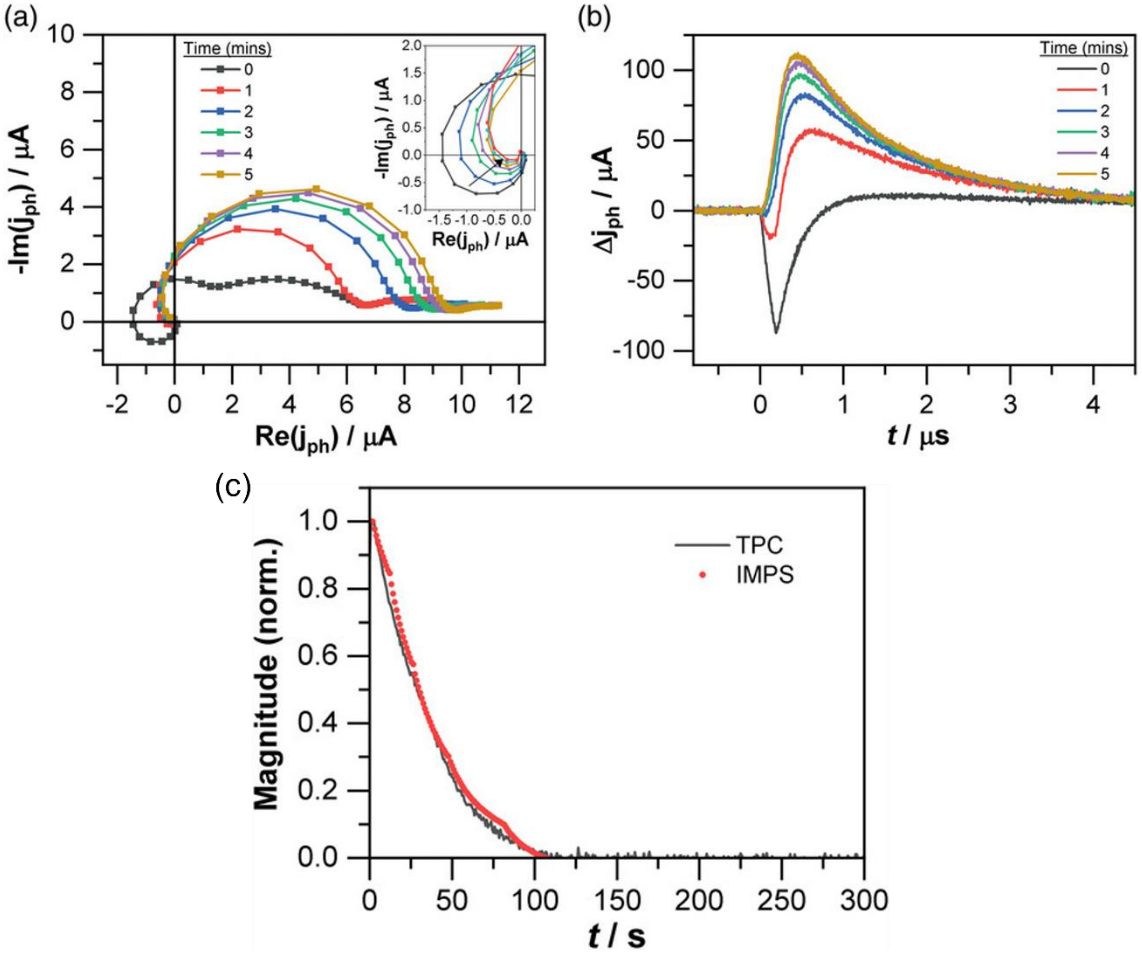

Figure 15. a) Progression of IMPS response of meso-C device at 1 min intervals (inset: 10 s intervals for first 1 min after illumination). b) Progression of TPC response at 1 min intervals. c) Comparison of the relative magnitude of the negative photocurrent signal from IMPS and TPC measurements for a meso-C device. Adapted with permission from ref. [84]. © 2021 The Authors. Solar RRL published by Wiley-VCH GmbH.

After confirmation that this feature was real, and not a failure of the experiment, the second work dealt with the explanation of this high-frequency spiral characteristic of the IMPS. In fact, we observed this feature in another kind of configuration (lateral contacted) and experimental set-up that lead us to the proper explanation for this feature. We found out that the spiraling at high frequency is due to a non-uniform generation profile that forces one of the charge carriers to diffuse until its selective contact. We model both configurations, (lateral contacted and the carbon-based solar cell), and we found a compromise between the absorption length and the diffusion length that governs the shape of the IMPS spectra and whether it would spiral or not. Finally, we achieve the extraction of charge carrier diffusion by the fitting of IMPS transfer functions, and we demonstrated that the diffusion of perovskites can be ascertained with small perturbation techniques. For the first time, we got values for the diffusion length of perovskites that are coherent with those of the literature. An example of the fitting of such measurements is shown in Figure 16.

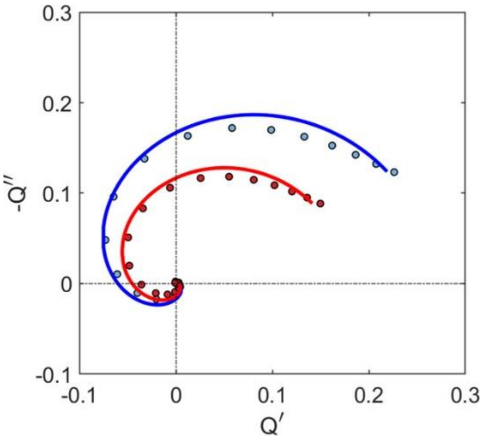

Figure 16. IMPS data (point) and fit (line) for a perovskite cell of 5.3 μm thickness illuminated with blue and red light, with an estimated absorption length of 40 and 140 nm, respectively. (34) The series resistance is 10 Ω cm2, and the geometrical capacitance is 36 nF cm–2 as determined by impedance spectroscopy. The effect of RC attenuation is negligible. Reproduced with permission from ref. ^{57}. Copyright © 2021 American Chemical Society.

In the third work relating the three techniques we aim to explain why voltage-modulated measurements do not have the same information as light-modulated techniques. For that purpose, we calculated the response of charge carrier diffusion for the voltage-modulated technique, the IS, and the two light-modulated techniques, the IMPS and the IMVS. From these results, we concluded that while in IS both the perturbation and the response take place at the same contact, in IMPS and IMVS it is possible to apply the perturbation far from the collecting contact of one of the charge carriers, disclosing the diffusion of these particles along the film. We corroborated these results with experimental evidence that put together the three spectra showing how both the IMPS and the IMVS drew the spiral through various quadrants at high frequency, while the IS drew directly an arc. Figure 17 is a recap of such results, and it contains the three techniques in one panel, by normalizing their transfer functions dimensionless. We found and defined the factor that provokes the spiraling of the spectra, which is present in both the IMPS and IMVS calculated transfer functions, but missing in the IS. The details of such factor are found in Chapter 4.

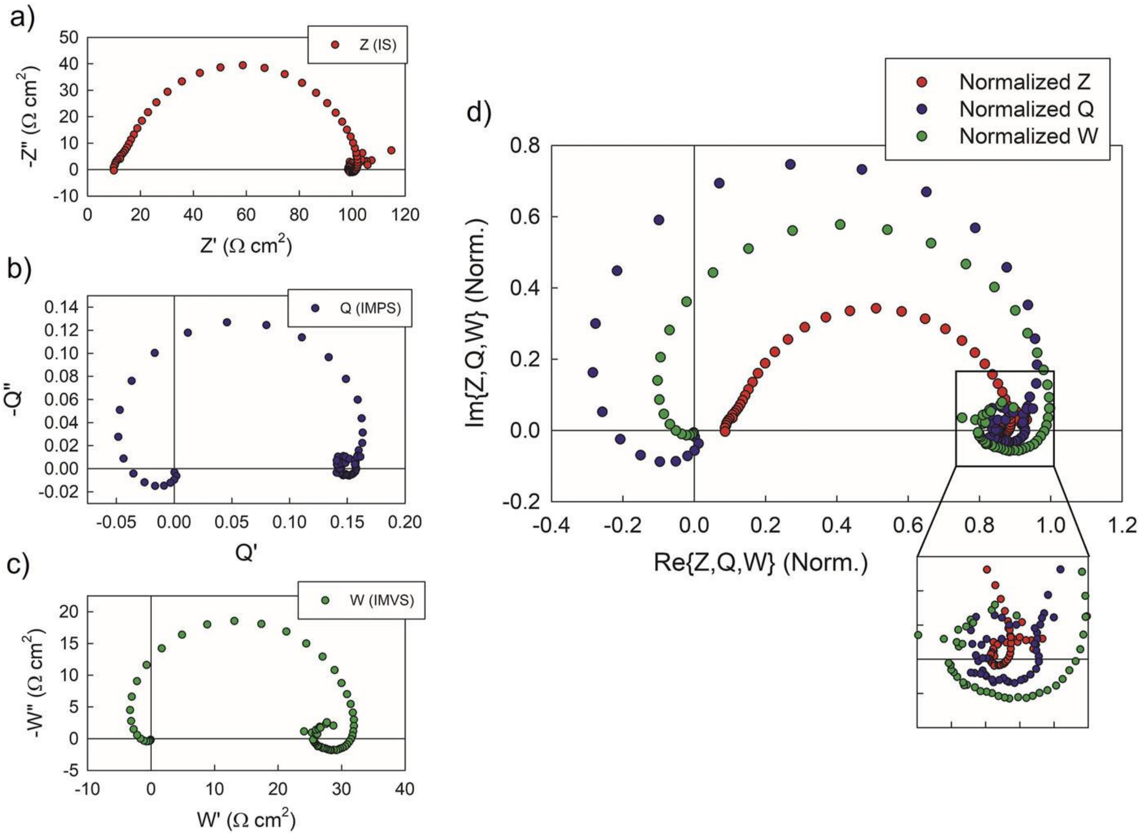

Figure 17. Experimental complex plane plots of (a) IS, (b) IMPS, and (c) IMVS for a carbon-based perovskite solar cell measured with illumination of 0,11 sun and at open circuit voltage (V = 0.85 V). (d) shows the three normalized spectra together. Reproduced from ref. [85] with the permission of AIP Publishing.

To validate this results, we tested the relation between the transfer functions in Equation 4 by dividing both theoretically and experimentally the IMVS and IMPS transfer functions, and we get a successful result, since the result of the division is comparable to the IS experimental spectra.

The last chapter of this thesis comes back to the IS characterization alone and is mainly focused on the exotic behavior of perovskite devices, the inductive loop or negative capacitance. This characteristic is displayed in the complex-plane plot of IS transfer function as a third arc going into the fourth quadrant either at a lower frequency after the low frequency positive arc or between the two arcs above.[86-88] This arc in the fourth quadrant goes in the direction of decreasing resistance with decreasing frequency, resulting in a lower dc resistance. Usually, this feature is not present at low voltage bias but appears when increasing the voltage to values close to the open-circuit voltage.[89] In fact, the low frequency first-quadrant arc can be sometimes substituted by a fourth-quadrant arc with increasing voltage.[78] Although there is not a consensus regarding the name of this feature, we will call it inductive loop instead of negative capacitance. The "negative capacitance" designation arises from the bode plot of capacitance vs.

frequency, where the negative values of the imaginary part of the IS transfer function give an apparent negative capacitance.

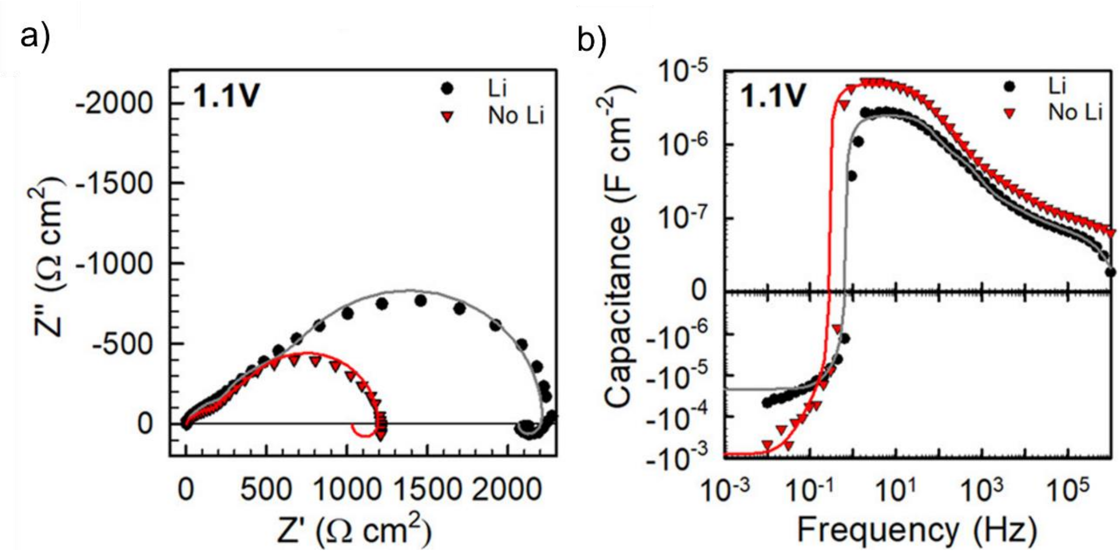

Figure 18. (a) Impedance plot and corresponding (b) capacitance spectra, measured under dark conditions and at 1.1 V. Solid lines correspond to fits using the equivalent circuit from Surface Polarization Model. Reproduced with permission from ref. [88]. Copyright © 2020, American Chemical Society.

The capacitance is calculated from the IS transfer function as:

$$C'(\omega) = \frac{-1}{\omega Z''(\omega)} \quad (5)$$

Therefore, any IS data going into the fourth quadrant will give an apparent negative capacitance, as in Figure 18b. However, we know, from calculations, that a negative capacitance with a parallel resistance gives an arc in the fourth quadrant in the direction of increasing resistances with decreasing frequency, i.e., opposite to the experimental spectra. In order to reproduce the experimental data from perovskite solar cells with a negative capacitance, the parallel resistance must be negative as well. Instead, introducing a parallel branch with a resistance and an inductor gives exactly the kind of spectra that is generated by a variety of perovskite devices. For this reason, we shall refer to this feature as inductive loop.

Recently, the concept of the chemical inductor was proposed by Bisquert.[90] This concept is based in an additional current component which is controlled by an internal variable of the device. This internal variable has a relaxation equation of the form:

$$\tau_k \frac{\mathrm{d}\,x}{\mathrm{d}\,t} = g(x, u) \quad (6)$$

where u es the applied voltage. When calculating the equivalent circuit generated by this equation, we obtain a branch containing a resistance and an inductor parallel to the rest of the circuit. Although the chemical inductor has been introduced recently as a general concept, we had previously worked on models that satisfy the form of Eq. 6, such as the

Surface Polarization Model. As mentioned above, the hysteresis of perovskite solar cells has been an issue and the modelling of such behavior has challenged researchers. Ravishankar et al. proposed the surface polarization model that, as we previously explained, is based on an internal surface voltage that is governed by a relaxation equation (Equation 3) capable of reproducing the hysteretic current-voltage curves.[30] The calculation of the impedance response of such model, resulted in an equivalent circuit with a parallel branch including a resistance and an inductor directly from the model.[32] The discovery of such equivalent circuit has been the precedent of the last chapter of the thesis and, as we shall see, it has similarities with the equivalent circuits of both memristors and various models describing the action potentials in neurons, such as Hodgkin-Huxley model. Hence, this work demonstrates that perovskites are a strong candidate for memristor devices and for building artificial neuromorphic networks, all by means of their IS characteristics. In like manner, this justifies the “inductive loop” denomination or chemical inductor for the fourth quadrant arc of perovskites solar cells, since the R-L branch in the equivalent circuit is common in a variety of systems and models.

Perovskite memristors have shown systematically inductive loops in the IS measurements connected with inverted hysteresis in current-voltage characteristics.[76] Since memristors are one of the most promising candidates for the realization of artificial neuromorphic computation, we aim to compare their IS characteristics with those of natural systems. Therefore, in this last chapter, we calculated the impedance response of a generic memristor, as well as the responses of other complex models that describe the operation of neuron spiking. We derived the equivalent circuits that generate such responses, and we immediately found the well-known R-L branches from the perovskite models or the chemical inductor. In fact, some neuron models included several R-L branches in their equivalent circuit. We carried out an exhaustive study of the responses of such models depending on the parameters of the models. In the case of the Hodgkin-Huxley model, for example, we found a rich variety of spectra depending on the applied voltage, as seen in Figure 19.

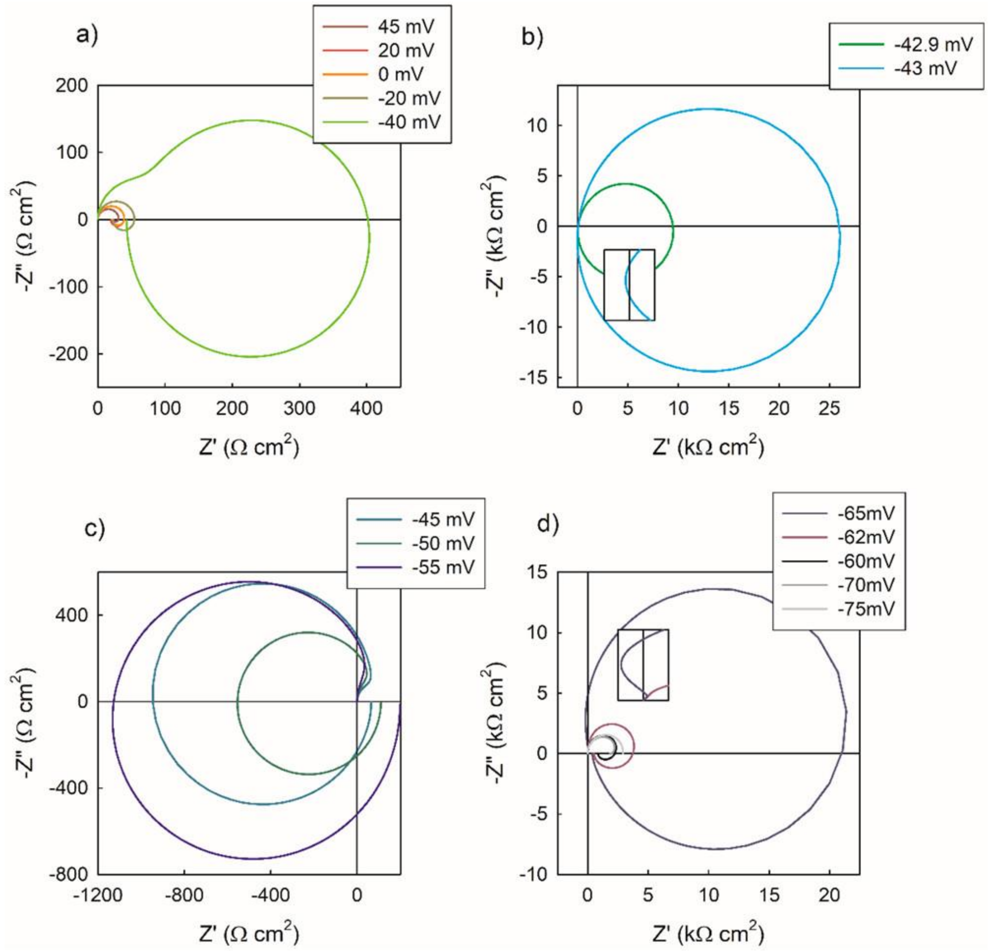

Figure 19. Impedance complex plane plots for voltages (a) above the upper limit of the negative impedance region, (b) around the upper limit VM = −42.99 mV, (c) in the negative impedance region, and (d) around the lower limit VM = −60.25 mV. Reproduced with permission from ref. [91]. Copyright © 2021 American Chemical Society.

It is important to remark that, despite the complexity of the equivalent circuits generated by such models, the values of the electrical elements that form these equivalent circuits are determined by variables such as the applied voltage, and the spectra that they can generate are not infinite. In fact, as we shall see in chapter 5, some of the elements depend on the other elements and evolve with voltage. This can be seen in Figure 20, where we show the dependence of some circuit elements with voltage.

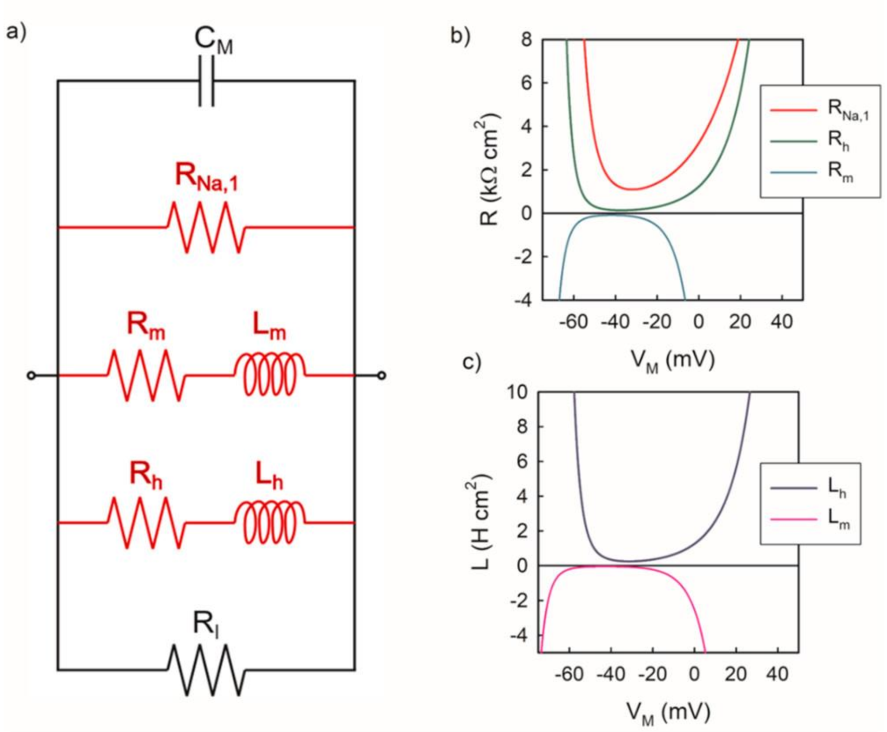

Figure 20. Impedance details of the Na channel of the Hodgkin-Huxley model. (a) EC used for the Na channel. (b and c) Values of the resistances and inductors for the range of membrane voltages, respectively. Reproduced with permission from ref. [91]. Copyright © 2021 American Chemical Society.

In summary, the work carried out in this thesis has resulted in a broad picture about the small perturbation techniques characteristics of perovskite solar cells and perovskite memristors. In the case of perovskite solar cells, we have made extensive research with both light-modulated and voltage-modulated techniques that has resulted in three main conclusions. First, the electronic diffusion of perovskites can be extracted from small perturbation techniques under conditions of non-uniform generation profiles. Specifically, we have calculated the diffusion parameters of perovskites from the spiraling feature of the high frequency part of IMPS spectra. Second, we have identified the factor that allows the display of the diffusion trace in light-modulated techniques in contrast with voltage-modulated ones, and we have demonstrated experimentally how they are manifested. Third, we have proved the relation between the techniques and we have been able to distinguish the features that occur at different time-scales. In the case of perovskite memristors, we have developed a systematic method for the analysis of the similarity of their IS characteristics with neuron models, broadening the possibilities to study these devices as a possible candidate for applications in neuromorphic networks.

References

1. Ahmad, T.; Zhang, D., A critical review of comparative global historical energy consumption and future demand: The story told so far. *Energy Reports* **2020,** *6*, 1973-1991.

2. IEA (2021), World Energy Outlook 2021, IEA, Paris https://www.iea.org/reports/world-energy-outlook-2021.

3. United Nations Department of Economic and Social Affairs, Population Division (2022). *World Population Prospects 2022: Summary of Results*.

4. ©Fraunhofer ISE: Photovoltaics Report, updated: 22 September 2022.

5. Kojima, A.; Teshima, K.; Shirai, Y.; Miyasaka, T., Organometal Halide Perovskites as Visible-Light Sensitizers for Photovoltaic Cells. *Journal of the American Chemical Society* **2009,** *131* (17), 6050-6051.

6. Kim, H.-S.; Lee, C.-R.; Im, J.-H.; Lee, K.-B.; Moehl, T.; Marchioro, A.; Moon, S.-J.; Humphry-Baker, R.; Yum, J.-H.; Moser, J. E.; Grätzel, M.; Park, N.-G., Lead Iodide Perovskite Sensitized All-Solid-State Submicron Thin Film Mesoscopic Solar Cell with Efficiency Exceeding 9%. *Scientific Reports* **2012,** *2* (1), 591.

7. Jeong, J.; Kim, M.; Seo, J.; Lu, H.; Ahlawat, P.; Mishra, A.; Yang, Y.; Hope, M. A.; Eickemeyer, F. T.; Kim, M.; Yoon, Y. J.; Choi, I. W.; Darwich, B. P.; Choi, S. J.; Jo, Y.; Lee, J. H.; Walker, B.; Zakeeruddin, S. M.; Emsley, L.; Rothlisberger, U.; Hagfeldt, A.; Kim, D. S.; Grätzel, M.; Kim, J. Y., Pseudo-halide anion engineering for α-FAPbI3 perovskite solar cells. *Nature* **2021,** *592* (7854), 381-385.

8. Wang, J.; Zhang, J.; Zhou, Y.; Liu, H.; Xue, Q.; Li, X.; Chueh, C.-C.; Yip, H.-L.; Zhu, Z.; Jen, A. K. Y., Highly efficient all-inorganic perovskite solar cells with suppressed non-radiative recombination by a Lewis base. *Nature Communications* **2020,** *11* (1), 177.

9. Li, Z.; Klein, T. R.; Kim, D. H.; Yang, M.; Berry, J. J.; van Hest, M. F. A. M.; Zhu, K., Scalable fabrication of perovskite solar cells. *Nature Reviews Materials* **2018,** *3* (4), 18017.

10. Parida, B.; Singh, A.; Kalathil Soopy, A. K.; Sangaraju, S.; Sundaray, M.; Mishra, S.; Liu, S.; Najar, A., Recent Developments in Upscalable Printing Techniques for Perovskite Solar Cells. *Advanced Science* **2022,** *9* (14), 2200308.

11. Chen, Y.; Zhang, L.; Zhang, Y.; Gao, H.; Yan, H., Large-area perovskite solar cells – a review of recent progress and issues. *RSC Advances* **2018,** *8* (19), 10489-10508.

12. Adjokatse, S.; Fang, H.-H.; Loi, M. A., Broadly tunable metal halide perovskites for solid-state light-emission applications. *Materials Today* **2017,** *20* (8), 413-424.

13. Shockley, W.; Queisser, H. J., Detailed Balance Limit of Efficiency of p-n Junction Solar Cells. *Journal of Applied Physics* **1961,** *32* (3), 510-519.

14. Fang, Z.; Zeng, Q.; Zuo, C.; Zhang, L.; Xiao, H.; Cheng, M.; Hao, F.; Bao, Q.; Zhang, L.; Yuan, Y.; Wu, W.-Q.; Zhao, D.; Cheng, Y.; Tan, H.; Xiao, Z.; Yang, S.; Liu, F.; Jin, Z.; Yan, J.; Ding, L., Perovskite-based tandem solar cells. *Science Bulletin* **2021,** *66* (6), 621-636.

15. Sutherland, B. R., Solar Materials Find Their Band Gap. *Joule* **2020,** *4* (5), 984-985.

16. Liu, M.; Zhao, R.; Sun, F.; Zhang, P.; Zhang, R.; Chen, Z.; Li, S., Wavelength-Tuneable Near-Infrared Luminescence in Mixed Tin–Lead Halide Perovskites. **2022,** *10*.

17. Karlsson, M.; Yi, Z.; Reichert, S.; Luo, X.; Lin, W.; Zhang, Z.; Bao, C.; Zhang, R.; Bai, S.; Zheng, G.; Teng, P.; Duan, L.; Lu, Y.; Zheng, K.; Pullerits, T.; Deibel, C.; Xu, W.; Friend, R.; Gao, F., Mixed halide perovskites for spectrally stable and high-efficiency blue light-emitting diodes. *Nature Communications* **2021,** *12* (1), 361.

18. Zhang, Q.; Shang, Q.; Su, R.; Do, T. T. H.; Xiong, Q., Halide Perovskite Semiconductor Lasers: Materials, Cavity Design, and Low Threshold. *Nano Letters* **2021,** *21* (5), 1903-1914.

19. Deumel, S.; van Breemen, A.; Gelinck, G.; Peeters, B.; Maas, J.; Verbeek, R.; Shanmugam, S.; Akkerman, H.; Meulenkamp, E.; Huerdler, J. E.; Acharya, M.; García-Batlle, M.; Almora, O.; Guerrero, A.; Garcia-Belmonte, G.; Heiss, W.; Schmidt, O.; Tedde, S. F., High-sensitivity high-resolution X-ray imaging with soft-sintered metal halide perovskites. *Nature Electronics* **2021,** *4* (9), 681-688.

20. Park, Y.; Lee, J.-S., Metal Halide Perovskite-Based Memristors for Emerging Memory Applications. *The Journal of Physical Chemistry Letters* **2022,** *13* (24), 5638-5647.

21. Zhao, X.; Xu, H.; Wang, Z.; Lin, Y.; Liu, Y., Memristors with organic-inorganic halide perovskites. *InfoMat* **2019,** *1* (2), 183-210.

22. Stranks, S. D.; Eperon, G. E.; Grancini, G.; Menelaou, C.; Alcocer, M. J. P.; Leijtens, T.; Herz, L. M.; Petrozza, A.; Snaith, H. J., Electron-Hole Diffusion Lengths Exceeding 1 Micrometer in an Organometal Trihalide Perovskite Absorber. *Science* **2013,** *342* (6156), 341-344.

23. Luo, D.; Su, R.; Zhang, W.; Gong, Q.; Zhu, R., Minimizing non-radiative recombination losses in perovskite solar cells. *Nature Reviews Materials* **2020,** *5* (1), 44-60.

24. Yang, Z.; Yu, Z.; Wei, H.; Xiao, X.; Ni, Z.; Chen, B.; Deng, Y.; Habisreutinger, S. N.; Chen, X.; Wang, K.; Zhao, J.; Rudd, P. N.; Berry, J. J.; Beard, M. C.; Huang, J., Enhancing electron diffusion length in narrow-bandgap perovskites for

efficient monolithic perovskite tandem solar cells. *Nature Communications* **2019,** *10* (1), 4498.

25. Meng, L.; You, J.; Yang, Y., Addressing the stability issue of perovskite solar cells for commercial applications. *Nature Communications* **2018,** *9* (1), 5265.

26. Tress, W.; Marinova, N.; Moehl, T.; Zakeeruddin, S. M.; Nazeeruddin, M. K.; Grätzel, M., Understanding the rate-dependent J–V hysteresis, slow time component, and aging in CH3NH3PbI3 perovskite solar cells: the role of a compensated electric field. *Energy & Environmental Science* **2015,** *8* (3), 995-1004.

27. Eames, C.; Frost, J. M.; Barnes, P. R. F.; O'Regan, B. C.; Walsh, A.; Islam, M. S., Ionic transport in hybrid lead iodide perovskite solar cells. *Nature Communications* **2015,** *6* (1), 7497.

28. Snaith, H. J.; Abate, A.; Ball, J. M.; Eperon, G. E.; Leijtens, T.; Noel, N. K.; Stranks, S. D.; Wang, J. T.-W.; Wojciechowski, K.; Zhang, W., Anomalous Hysteresis in Perovskite Solar Cells. *The Journal of Physical Chemistry Letters* **2014,** *5* (9), 1511-1515.

29. Jacobs, D. A.; Wu, Y.; Shen, H.; Barugkin, C.; Beck, F. J.; White, T. P.; Weber, K.; Catchpole, K. R., Hysteresis phenomena in perovskite solar cells: the many and varied effects of ionic accumulation. *Physical Chemistry Chemical Physics* **2017,** *19* (4), 3094-3103.

30. Ravishankar, S.; Almora, O.; Echeverría-Arrondo, C.; Ghahremanirad, E.; Aranda, C.; Guerrero, A.; Fabregat-Santiago, F.; Zaban, A.; Garcia-Belmonte, G.; Bisquert, J., Surface Polarization Model for the Dynamic Hysteresis of Perovskite Solar Cells. *The Journal of Physical Chemistry Letters* **2017,** *8* (5), 915-921.

31. Kang, D.-H.; Park, N.-G., On the Current–Voltage Hysteresis in Perovskite Solar Cells: Dependence on Perovskite Composition and Methods to Remove Hysteresis. *Advanced Materials* **2019,** *31* (34), 1805214.

32. Ghahremanirad, E.; Bou, A.; Olyaee, S.; Bisquert, J., Inductive Loop in the Impedance Response of Perovskite Solar Cells Explained by Surface Polarization Model. *The Journal of Physical Chemistry Letters* **2017**, 1402-1406.

33. Bisquert, J., The Impedance of Spiking Neurons Coupled by Time-Delayed Interaction. *physica status solidi (a)* **2022,** *219* (12), 2200064.

34. Guerrero, A.; Bisquert, J.; Garcia-Belmonte, G., Impedance Spectroscopy of Metal Halide Perovskite Solar Cells from the Perspective of Equivalent Circuits. *Chemical Reviews* **2021,** *121* (23), 14430-14484.

35. Salado, M.; Andresini, M.; Huang, P.; Khan, M. T.; Ciriaco, F.; Kazim, S.; Ahmad, S., Interface Engineering by Thiazolium Iodide Passivation Towards Reduced

Thermal Diffusion and Performance Improvement in Perovskite Solar Cells. *Advanced Functional Materials* **2020,** *30* (14), 1910561.

36. Straub, A.; Gebs, R.; Habenicht, H.; Trunk, S.; Bardos, R. A.; Sproul, A. B.; Aberle, A. G., Impedance analysis: A powerful method for the determination of the doping concentration and built-in potential of nonideal semiconductor p-n diodes. *Journal of Applied Physics* **2005,** *97* (8), 083703.

37. Barbero, G.; Fytas, N. G.; Lelidis, I.; da Silva Andrade, J. V.; Freire, F. C. M.; Santana, A. J., Determination of the recombination coefficient in electrolytic solutions from impedance spectroscopy measurements. *Journal of Electroanalytical Chemistry* **2022,** *907*, 116070.

38. Fabregat-Santiago, F.; Garcia-Belmonte, G.; Mora-Seró, I.; Bisquert, J., Characterization of nanostructured hybrid and organic solar cells by impedance spectroscopy. *Physical Chemistry Chemical Physics* **2011,** *13*, 9083–9118.

39. Wang, Q.; Moser, J.-E.; Grätzel, M., Electrochemical Impedance Spectroscopic Analysis of Dye-Sensitized Solar Cells. *The Journal of Physical Chemistry B* **2005,** *109* (31), 14945-14953.

40. Peng, W.; Aranda, C.; Bakr, O. M.; Garcia-Belmonte, G.; Bisquert, J.; Guerrero, A., Quantification of Ionic Diffusion in Lead Halide Perovskite Single Crystals. *ACS Energy Letters* **2018,** *3* (7), 1477-1481.

41. Zarazua, I.; Han, G.; Boix, P. P.; Mhaisalkar, S.; Fabregat-Santiago, F.; Mora-Seró, I.; Bisquert, J.; Garcia-Belmonte, G., Surface Recombination and Collection Efficiency in Perovskite Solar Cells from Impedance Analysis. *The Journal of Physical Chemistry Letters* **2016,** *7* (24), 5105-5113.

42. Almora, O.; Cho, K. T.; Aghazada, S.; Zimmermann, I.; Matt, G. J.; Brabec, C. J.; Nazeeruddin, M. K.; Garcia-Belmonte, G., Discerning recombination mechanisms and ideality factors through impedance analysis of high-efficiency perovskite solar cells. *Nano Energy* **2018,** *48*, 63-72.

43. Zarazua, I.; Bisquert, J.; Garcia-Belmonte, G., Light-Induced Space-Charge Accumulation Zone as Photovoltaic Mechanism in Perovskite Solar Cells. *The Journal of Physical Chemistry Letters* **2016,** *7* (3), 525-528.

44. Anaya, M.; Zhang, W.; Hames, B. C.; Li, Y.; Fabregat-Santiago, F.; Calvo, M. E.; Snaith, H. J.; Míguez, H.; Mora-Seró, I., Electron injection and scaffold effects in perovskite solar cells. *Journal of Materials Chemistry C* **2017,** *5* (3), 634-644.

45. Guerrero, A.; Garcia-Belmonte, G.; Mora-Sero, I.; Bisquert, J.; Kang, Y. S.; Jacobsson, T. J.; Correa-Baena, J.-P.; Hagfeldt, A., Properties of Contact and Bulk Impedances in Hybrid Lead Halide Perovskite Solar Cells Including Inductive Loop Elements. *The Journal of Physical Chemistry C* **2016,** *120* (15), 8023-8032.

46. García-Rodríguez, R.; Ferdani, D.; Pering, S.; Baker, P. J.; Cameron, P. J., Influence of bromide content on iodide migration in inverted MAPb(I1−xBrx)3 perovskite solar cells. *Journal of Materials Chemistry A* **2019,** *7* (39), 22604-22614.

47. Wang, H.; Guerrero, A.; Bou, A.; Al-Mayouf, A. M.; Bisquert, J., Kinetic and material properties of interfaces governing slow response and long timescale phenomena in perovskite solar cells. *Energy & Environmental Science* **2019,** *12* (7), 2054-2079.

48. Bertoluzzi, L.; Bisquert, J., Investigating the Consistency of Models for Water Splitting Systems by Light and Voltage Modulated Techniques. *The Journal of Physical Chemistry Letters* **2017,** *8* (1), 172-180.

49. Li, J.; Peat, R.; Peter, L. M., Surface recombination at semiconductor electrodes: Part II. Photoinduced “near-surface” recombination centres in p-GaP. *Journal of Electroanalytical Chemistry and Interfacial Electrochemistry* **1984,** *165* (1), 41-59.

50. Peter, L. M., Dynamic aspects of semiconductor photoelectrochemistry. *Chemical Reviews* **1990,** *90* (5), 753-769.

51. Halme, J.; Miettunen, K.; Lund, P., Effect of Nonuniform Generation and Inefficient Collection of Electrons on the Dynamic Photocurrent and Photovoltage Response of Nanostructured Photoelectrodes. *The Journal of Physical Chemistry C* **2008,** *112* (51), 20491-20504.

52. Dloczik, L.; Ileperuma, O.; Lauermann, I.; Peter, L. M.; Ponomarev, E. A.; Redmond, G.; Shaw, N. J.; Uhlendorf, I., Dynamic Response of Dye-Sensitized Nanocrystalline Solar Cells: Characterization by Intensity-Modulated Photocurrent Spectroscopy. *The Journal of Physical Chemistry B* **1997,** *101* (49), 10281-10289.

53. de Jongh, P. E.; Vanmaekelbergh, D., Trap-Limited Electronic Transport in Assemblies of Nanometer-Size Ti${\mathrm{O}}_{2}$ Particles. *Physical Review Letters* **1996,** *77* (16), 3427-3430.

54. Pockett, A.; Eperon, G. E.; Peltola, T.; Snaith, H. J.; Walker, A.; Peter, L. M.; Cameron, P. J., Characterization of Planar Lead Halide Perovskite Solar Cells by Impedance Spectroscopy, Open-Circuit Photovoltage Decay, and Intensity-Modulated Photovoltage/Photocurrent Spectroscopy. *The Journal of Physical Chemistry C* **2015,** *119* (7), 3456-3465.

55. Ravishankar, S.; Aranda, C.; Sanchez, S.; Bisquert, J.; Saliba, M.; Garcia-Belmonte, G., Perovskite Solar Cell Modeling Using Light- and Voltage-Modulated Techniques. *The Journal of Physical Chemistry C* **2019,** *123* (11), 6444-6449.

56. Ravishankar, S.; Aranda, C.; Boix, P. P.; Anta, J. A.; Bisquert, J.; Garcia-Belmonte, G., Effects of Frequency Dependence of the External Quantum Efficiency of Perovskite Solar Cells. *The Journal of Physical Chemistry Letters* **2018,** *9* (11), 3099-3104.

57. Bou, A.; Āboliņš, H.; Ashoka, A.; Cruanyes, H.; Guerrero, A.; Deschler, F.; Bisquert, J., Extracting in Situ Charge Carrier Diffusion Parameters in Perovskite Solar Cells with Light Modulated Techniques. *ACS Energy Letters* **2021,** *6* (6), 2248-2255.

58. Set, Y. T.; Li, B.; Lim, F. J.; Birgersson, E.; Luther, J., Analytical modeling of intensity-modulated photovoltage spectroscopic responses of organic bulk-heterojunction solar cells. *Applied Physics Letters* **2015,** *107* (17), 173301.

59. Pereyra, C. J.; Di Iorio, Y.; Berruet, M.; Vazquez, M.; Marotti, R. E., Carrier recombination and transport dynamics in superstrate solar cells analyzed by modeling the intensity modulated photoresponses. *Physical Chemistry Chemical Physics* **2019,** *21* (36), 20360-20371.

60. Schlichthörl, G.; Huang, S. Y.; Sprague, J.; Frank, A. J., Band Edge Movement and Recombination Kinetics in Dye-Sensitized Nanocrystalline TiO2 Solar Cells: A Study by Intensity Modulated Photovoltage Spectroscopy. *The Journal of Physical Chemistry B* **1997,** *101* (41), 8141-8155.

61. Thorne, J. E.; Jang, J.-W.; Liu, E. Y.; Wang, D., Understanding the origin of photoelectrode performance enhancement by probing surface kinetics. *Chemical Science* **2016,** *7* (5), 3347-3354.

62. Pockett, A.; Eperon, G. E.; Sakai, N.; Snaith, H. J.; Peter, L. M.; Cameron, P. J., Microseconds, milliseconds and seconds: deconvoluting the dynamic behaviour of planar perovskite solar cells. *Physical Chemistry Chemical Physics* **2017,** *19* (8), 5959-5970.

63. García-Rosell, M.; Bou, A.; Jiménez-Tejada, J. A.; Bisquert, J.; Lopez-Varo, P., Analysis of the Influence of Selective Contact Heterojunctions on the Performance of Perovskite Solar Cells. *The Journal of Physical Chemistry C* **2018,** *122* (25), 13920-13925.

64. Pham, N. D.; Zhang, C.; Tiong, V. T.; Zhang, S.; Will, G.; Bou, A.; Bisquert, J.; Shaw, P. E.; Du, A.; Wilson, G. J.; Wang, H., Tailoring Crystal Structure of FA0.83Cs0.17PbI3 Perovskite Through Guanidinium Doping for Enhanced Performance and Tunable Hysteresis of Planar Perovskite Solar Cells. *Advanced Functional Materials* **2019,** *29* (1), 1806479.

65. Guerrero, A.; Bou, A.; Matt, G.; Almora, O.; Heumüller, T.; Garcia-Belmonte, G.; Bisquert, J.; Hou, Y.; Brabec, C., Switching Off Hysteresis in Perovskite Solar Cells by Fine-Tuning Energy Levels of Extraction Layers. *Advanced Energy Materials* **2018,** *8* (21), 1703376.

66. Chen, B.; Yang, M.; Priya, S.; Zhu, K., Origin of J–V Hysteresis in Perovskite Solar Cells. *The Journal of Physical Chemistry Letters* **2016,** *7* (5), 905-917.

67. van Reenen, S.; Kemerink, M.; Snaith, H. J., Modeling Anomalous Hysteresis in Perovskite Solar Cells. *The Journal of Physical Chemistry Letters* **2015,** *6* (19), 3808-3814.

68. Nemnes, G. A.; Besleaga, C.; Stancu, V.; Dogaru, D. E.; Leonat, L. N.; Pintilie, L.; Torfason, K.; Ilkov, M.; Manolescu, A.; Pintilie, I., Normal and Inverted Hysteresis in Perovskite Solar Cells. *The Journal of Physical Chemistry C* **2017,** *121* (21), 11207-11214.

69. Liu, Y.; Collins, L.; Proksch, R.; Kim, S.; Watson, B. R.; Doughty, B.; Calhoun, T. R.; Ahmadi, M.; Ievlev, A. V.; Jesse, S.; Retterer, S. T.; Belianinov, A.; Xiao, K.; Huang, J.; Sumpter, B. G.; Kalinin, S. V.; Hu, B.; Ovchinnikova, O. S., Chemical nature of ferroelastic twin domains in CH3NH3PbI3 perovskite. *Nature Materials* **2018,** *17* (11), 1013-1019.

70. Gómez, A.; Wang, Q.; Goñi, A. R.; Campoy-Quiles, M.; Abate, A., Ferroelectricity-free lead halide perovskites. *Energy & Environmental Science* **2019,** *12* (8), 2537-2547.

71. Meloni, S.; Moehl, T.; Tress, W.; Franckevičius, M.; Saliba, M.; Lee, Y. H.; Gao, P.; Nazeeruddin, M. K.; Zakeeruddin, S. M.; Rothlisberger, U.; Graetzel, M., Ionic polarization-induced current–voltage hysteresis in CH3NH3PbX3 perovskite solar cells. *Nature Communications* **2016,** *7* (1), 10334.

72. Futscher, M. H.; Lee, J. M.; McGovern, L.; Muscarella, L. A.; Wang, T.; Haider, M. I.; Fakharuddin, A.; Schmidt-Mende, L.; Ehrler, B., Quantification of ion migration in CH3NH3PbI3 perovskite solar cells by transient capacitance measurements. *Materials Horizons* **2019,** *6* (7), 1497-1503.

73. Weber, S. A. L.; Hermes, I. M.; Turren-Cruz, S.-H.; Gort, C.; Bergmann, V. W.; Gilson, L.; Hagfeldt, A.; Graetzel, M.; Tress, W.; Berger, R., How the formation of interfacial charge causes hysteresis in perovskite solar cells. *Energy & Environmental Science* **2018,** *11* (9), 2404-2413.

74. Richardson, G.; O'Kane, S. E. J.; Niemann, R. G.; Peltola, T. A.; Foster, J. M.; Cameron, P. J.; Walker, A. B., Can slow-moving ions explain hysteresis in the current–voltage curves of perovskite solar cells? *Energy & Environmental Science* **2016,** *9* (4), 1476-1485.

75. Li, C.; Guerrero, A.; Huettner, S.; Bisquert, J., Unravelling the role of vacancies in lead halide perovskite through electrical switching of photoluminescence. *Nature Communications* **2018,** *9* (1), 5113.

76. Berruet, M.; Pérez-Martínez, J. C.; Romero, B.; Gonzales, C.; Al-Mayouf, A. M.; Guerrero, A.; Bisquert, J., Physical Model for the Current–Voltage Hysteresis and Impedance of Halide Perovskite Memristors. *ACS Energy Letters* **2022,** *7* (3), 1214-1222.

77. Gonzales, C.; Guerrero, A.; Bisquert, J., Spectral properties of the dynamic state transition in metal halide perovskite-based memristor exhibiting negative capacitance. *Applied Physics Letters* **2021,** *118*, 073501.

78. Gonzales, C.; Guerrero, A.; Bisquert, J., Transition from Capacitive to Inductive Hysteresis: A Neuron-Style Model to Correlate I–V Curves to Impedances of Metal Halide Perovskites. *The Journal of Physical Chemistry C* **2022,** *126* (32), 13560-13578.

79. Bisquert, J.; Guerrero, A., Dynamic Instability and Time Domain Response of a Model Halide Perovskite Memristor for Artificial Neurons. *The Journal of Physical Chemistry Letters* **2022,** *13* (17), 3789-3795.

80. Wang, K.; Zhang, Z.; Wang, L.; Chen, K.; Tao, L.; Zhang, Y.; Zhou, X., Commercial Carbon-Based all-Inorganic Perovskite Solar Cells with a High Efficiency of 13.81%: Interface Engineering and Photovoltaic Performance. *ACS Applied Energy Materials* **2021,** *4* (4), 3255-3264.

81. Fagiolari, L.; Bella, F., Carbon-based materials for stable, cheaper and large-scale processable perovskite solar cells. *Energy & Environmental Science* **2019,** *12* (12), 3437-3472.

82. Bou, A.; Pockett, A.; Raptis, D.; Watson, T.; Carnie, M. J.; Bisquert, J., Beyond Impedance Spectroscopy of Perovskite Solar Cells: Insights from the Spectral Correlation of the Electrooptical Frequency Techniques. *The Journal of Physical Chemistry Letters* **2020,** *11* (20), 8654-8659.

83. Ravishankar, S.; Riquelme, A.; Sarkar, S. K.; Garcia-Batlle, M.; Garcia-Belmonte, G.; Bisquert, J., Intensity-Modulated Photocurrent Spectroscopy and Its Application to Perovskite Solar Cells. *The Journal of Physical Chemistry C* **2019,** *123* (41), 24995-25014.

84. Pockett, A.; Spence, M.; Thomas, S. K.; Raptis, D.; Watson, T.; Carnie, M. J., Beyond the First Quadrant: Origin of the High Frequency Intensity-Modulated Photocurrent/Photovoltage Spectroscopy Response of Perovskite Solar Cells. *Solar RRL* **2021,** *5* (5), 2100159.

85. Bou, A.; Pockett, A.; Cruanyes, H.; Raptis, D.; Watson, T.; Carnie, M. J.; Bisquert, J., Limited information of impedance spectroscopy about electronic diffusion transport: The case of perovskite solar cells. *APL Materials* **2022,** *10* (5), 051104.

86. Ebadi, F.; Taghavinia, N.; Mohammadpour, R.; Hagfeldt, A.; Tress, W., Origin of apparent light-enhanced and negative capacitance in perovskite solar cells. *Nature Communications* **2019,** *10* (1), 1574.

87. Fabregat-Santiago, F.; Kulbak, M.; Zohar, A.; Vallés-Pelarda, M.; Hodes, G.; Cahen, D.; Mora-Seró, I., Deleterious Effect of Negative Capacitance on the Performance of Halide Perovskite Solar Cells. *ACS Energy Letters* **2017,** *2* (9), 2007-2013.

88. Alvarez, A. O.; Arcas, R.; Aranda, C. A.; Bethencourt, L.; Mas-Marzá, E.; Saliba, M.; Fabregat-Santiago, F., Negative Capacitance and Inverted Hysteresis: Matching Features in Perovskite Solar Cells. *The Journal of Physical Chemistry Letters* **2020,** *11* (19), 8417-8423.

89. Munoz-Diaz, L.; Rosa, A. J.; Bou, A.; Sánchez, R. S.; Romero, B.; John, R. A.; Kovalenko, M. V.; Guerrero, A.; Bisquert, J., Inductive and Capacitive Hysteresis of Halide Perovskite Solar Cells and Memristors Under Illumination. **2022,** *10*.

90. Bisquert, J.; Guerrero, A., Chemical Inductor. *Journal of the American Chemical Society* **2022,** *144* (13), 5996-6009.

91. Bou, A.; Bisquert, J., Impedance Spectroscopy Dynamics of Biological Neural Elements: From Memristors to Neurons and Synapses. *The Journal of Physical Chemistry B* **2021,** *125* (35), 9934-9949.

Chapter 2

Publication 1

Beyond Impedance Spectroscopy of Perovskite Solar Cells: Insights from the Spectral Correlation of the Electrooptical Frequency Techniques

Bou, A.; Pockett, A.; Raptis, D.; Watson, T.; Carnie, M. J.; Bisquert, J. Beyond Impedance Spectroscopy of Perovskite Solar Cells: Insights from the Spectral Correlation of the Electrooptical Frequency Techniques, *The Journal of Physical Chemistry Letters*, **2020**, *11*, 8654–8659.

Candidate’s Contribution

Nature of Contribution	Extent of Contribution
• Performed the measurements • Performed the fitting and simulations • Developed the conceptualization • Wrote the first draft of the manuscript • Wrote the reply to the referees	80%

Introduction

This work presents the spectra of IS, IMPS and IMVS of carbon-based perovskite solar cells. It compares the response from three different kinds of perovskite solar cells, based on the perovskite layer thickness, concluding that the perovskite layer thickness affects mainly the mid-frequency part of the spectra. The correlation of the three techniques is also studied.

Published Manuscript

Beyond Impedance Spectroscopy of Perovskite Solar Cells: Insights from the Spectral Correlation of the Electrooptical Frequency Techniques

Agustín Bou[1], Adam Pockett*[2], Dimitrios Raptis[2], Trystan Watson[2], Matthew J. Carnie[2], Juan Bisquert*[1]

[1] Institute of Advanced Materials (INAM), Universitat Jaume I, 12006 Castelló, Spain

[2] SPECIFIC, Materials Research Center, College of Engineering, Swansea University, Bay Campus, Swansea SA1 8EN, UK

Email: adam.pockett@swansea.ac.uk bisquert@uji.es

Abstract

Small perturbation techniques have proven to be useful tools for the investigation of perovskite solar cells. A correct interpretation of the spectra given by impedance spectroscopy (IS), intensity-modulated photocurrent spectroscopy (IMPS) and intensity-modulated photovoltage spectroscopy (IMVS) is key for the understanding of device operation. The utilization of a correct equivalent circuit to extract real parameters is essential to make this good interpretation. In this work, we present an equivalent circuit, which is able to reproduce the general and the exotic behaviors found in impedance spectra. From the measurements, we demonstrate that the midfrequency features that may appear to depend on the active layer thickness, and we also prove the spectral correlation of the three techniques that has been suggested theoretically.

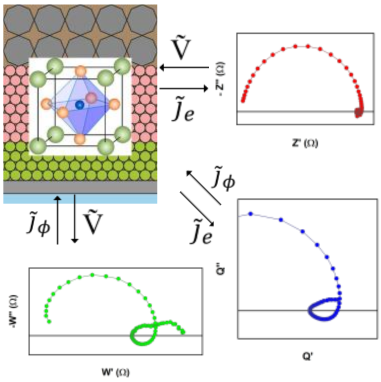

Perovskite solar cells' record efficiencies have rapidly risen over the last decade thanks to advances and progress in the device design and engineering. The improvements in the active layer, the selective contacts, and their interfaces have made perovskite solar cells a real candidate for commercialization. Understanding the electronic and ionic processes taking place in the bulk and contact layers is key for the control of the device quality and for the development of this technology.

Impedance spectroscopy (IS) is a useful technique to characterize physical processes in solar cell devices, and it has been applied extensively in perovskite solar cell research. However, the interpretation and analysis of IS results requires the use of a suitable equivalent circuit (EC). The search for an appropriate EC has been an aim among the perovskite community in the past years,[1-5] given the fact that a suitable EC would allow extraction of important parameters of the operation of perovskite solar cells. The wide variety of different spectra reported in the literature makes the convergence to a unique EC a complicated objective.

The majority of perovskite IS complex plots show two distinguishable arcs. However, the combination of both IS and intensity-modulated photocurrent spectroscopy (IMPS) has led to a better distinction of three different features.[6] This work introduced a novelty in the EC to explain the midfrequency arcs. In addition, the combination of time transient and capacitive methods shows an evolution of capacitance related to ionic dynamics.[7, 8] Another important feature to take into account in IS spectra is the negative capacitance.[9-12] This feature has been reported in a variety of publications and its meaning is still under debate.[5, 13-15] It usually appears in the lowest frequency region of the spectra and it shows up under different conditions, which makes it more complex to interpret. Different ECs have been proposed for the reproduction of experimental data.[5, 9, 10, 12, 13, 16] A negative capacitance could have a response due to distinct classes of phenomena. On the one hand, it is the interaction of ionic and electronic effects that conspires to produce delayed dynamics. On the other hand, it is a possible intrinsic instability of the device during the time of measurement of IS. This last phenomenon is clearly observed in perovskite memristors.[17]

The aim of this paper is to describe joint experimental measurements of IS, IMPS and intensity-modulated photovoltage spectroscopy (IMVS) in carbon-based perovskite solar cells with IS spectra that include negative capacitance features under open circuit conditions. Based on the observations, we wish to point out the distinct spectral features that are obtained in the combination of methods. Due to the lack of previous systematic studies, the election of a proper EC is not an easy question. Here, we propose a new EC that is able to reproduce spectra with midfrequency arcs and negative capacitances, based on previous studies.[6, 13] Earlier studies have also shown results of the use of the three techniques together for perovskite solar cells.[18] Here, we aim to clarify how the occurrence of the negative capacitance will affect the shape of the IMPS and IMVS spectra as a tool for interpretation of experiments.

For this work, we chose carbon-based perovskite solar cells, because although they take some time to stabilise, once they are stabilised, they are more stable than other architectures, and therefore, the reproducibility of the measurements is optimal. Moreover, they are a good candidate for addressing issues regarding large scale production. These solar cells consist of a scaffold of mesoporous TiO_2 and ZrO_2 layers infiltrated with perovskite and do not require a hole-conducting layer; see the structure of the cell in Figure S1.[19] These devices have a thicker perovskite active layer than regular devices and this could help see interesting spectra. In fact, carbon cells have shown very slow dynamic phenomena in voltage decay methods[20, 21] and tuneable hysteresis.[22] In this work, we used three kinds of devices with the same structure where the only change was the thickness of the zirconia layer and, therefore, the perovskite layer. We have chosen three thicknesses: Cells 1, 2 and 3 correspond to regular, double and triple thicknesses, respectively. Since the contacts and configuration are the same in all cells, any change in the spectral shapes can be directly related to the perovskite thickness. The current-voltage characteristics of the cells are detailed in Figure S2.

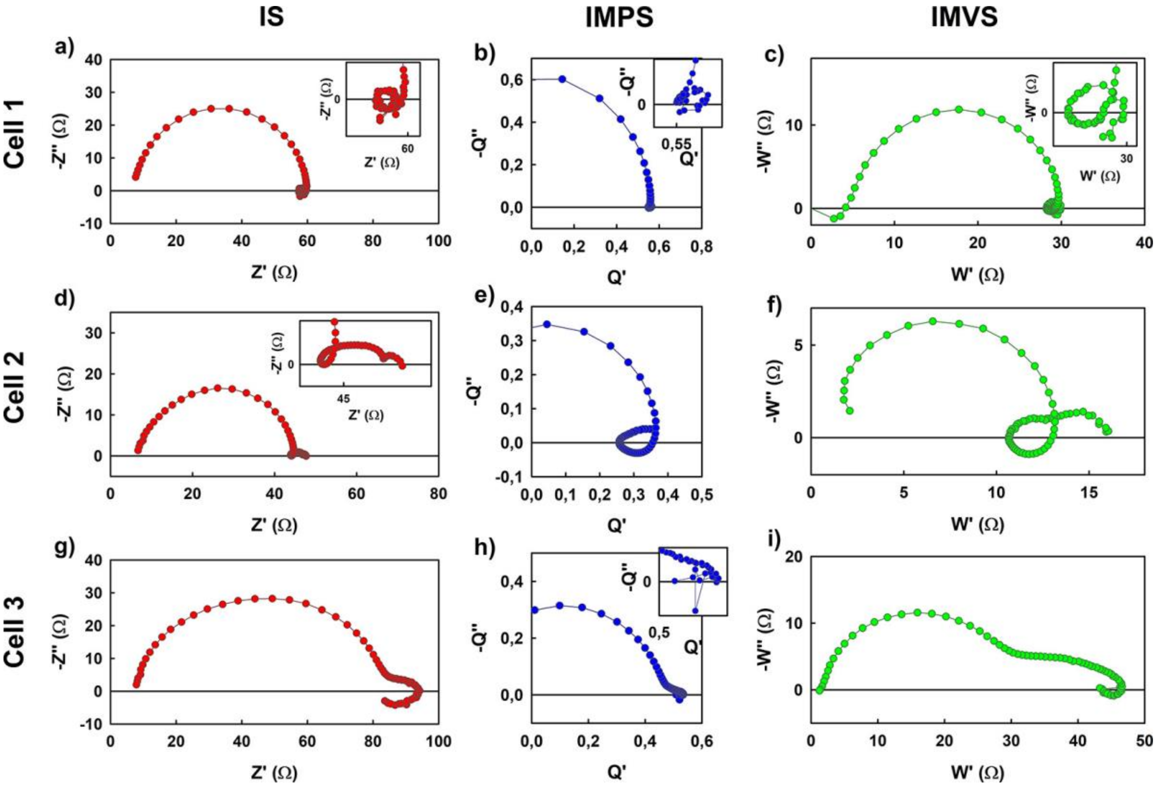

Figure 1. Complex plane plots of the IS (red), IMPS (blue) and IMVS (green) transfer functions (Z, Q, and W, respectively) for the three devices measured under 0.1 sun of illumination, for a frequency range of 1 MHz to 0.01 Hz and at open circuit voltage. (a-c) are the spectra for Cell 1; (d-f) are the spectra for Cell 2; and (g-i) are the spectra for Cell 3.

The spectra of IS, IMPS and IMVS for each cell are shown in Figure 1. If we want to compare all the measurements of the three techniques, it is important that all of them are made under the same conditions. Since IMVS measures the photovoltage change under a small perturbation in the light intensity, it takes place at open circuit conditions. Therefore, all the measurements were made at open circuit voltage.

The IS measurements were performed in the first instance. The fact that the literature about this technique is much more extensive makes it is easier to distinguish common features. A representative spectrum of each cell is shown in Figure S2. In general, a big high-frequency arc is common for the three cells, attributed to the geometrical capacitance and the recombination resistance. However, the features that appear next are not as common. We can immediately see inductive loops, negative capacitances, and intermediate frequency arcs. The analysis of the extracted parameters from IS is presented below. As mentioned above, the combination of more than one small perturbation technique has been demonstrated to help distinguish features happening at different frequencies in perovskite solar cells.[6] After negative capacitance features were detected in every device, it is a great opportunity to study how the presence of the negative capacitance affects the shape of IMPS and IMVS spectra.

In the second instance, we measured IMPS. The complex plane plots of the IMPS transfer function Q are shown in Figure 1(b,e,h) (blue). Again, we have a common feature in the high-frequency region: a bigger arc coming from the second quadrant. We find differences in the midfrequency region. Cell 1 shows another small arc with an intermediate loop in the first quadrant. Cell 2 goes into the fourth quadrant forming an intermediate frequency arc there and then coming back to the first quadrant, where it forms a low frequency arc. Cell 3 forms another arc in the first quadrant, and the lowest frequency points go slightly into the fourth quadrant, although this measurement is noisy at low frequency, and the points do not form a clear shape. Unlike the previous studies,[6, 23, 24] the low frequency part of the spectra remains or comes back to the first quadrant; this could be linked to the negative capacitance in IS spectra.

In the third instance, we measured IMVS. This is a technique for which spectra are not usually shown in the literature when talking about perovskite solar cells; instead, they only extract time constants. However, when converting the illumination intensity into current units, the IMVS transfer function (W) takes the same units as the IS transfer function (Z),[25] so their spectra may be comparable. In fact, we found spectra with similar shapes to those of IS, as we see in Figure 1(c,f,i) (green). Although the size of the different features changes somewhat, when comparing Z (red) with W (green), we see a significant correlation regarding the amount and kind of characteristics of the spectra. The change in the size of IMVS features compared to IS has previously been observed for midfrequency characteristics.[26]

Usually, impedance spectra of perovskite solar cells show only two well-separated arcs. The high frequency arc is related to bulk recombination and the geometrical capacitance, while the low frequency arc is related to interfacial phenomena. The large capacitance at low frequency has been interpreted as an accumulation of both ionic and electronic charge in the interfaces of the perovskite with the selective contacts.[27] The most widely used equivalent circuit for impedance spectra data fitting is shown in Figure 2. We will call this circuit Standard EC. Here, the low-frequency resistance and capacitance are R_1 and C_1, respectively, and R_3 is the high frequency resistance. C_g is the geometrical capacitance, and R_S is the series resistance.

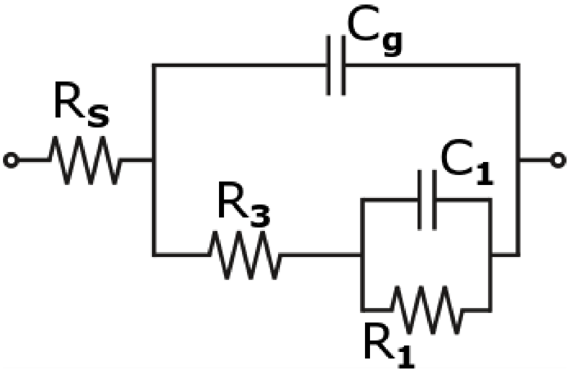

Figure 2. Standard EC used for the analysis of impedance spectra of perovskite solar cells.

This circuit is only able to produce impedance spectra with one or two arcs in the complex plane plot. However, perovskite spectra showing more features, either at intermediate or at low frequency, are not unusual, as we have seen in Figure S3. In fact, intermediate frequency features that can be hindered in impedance spectra may appear in IMPS spectra of the same cell. This is due to the fact that the time constants of IS features are different from those of IMPS ($\tau_{HF,IMPS} = R_S C_g$, $\tau_{HF,IS} = R_3 C_g$), so that features that appear distinct in one technique become combined in the other one, as previously discussed.[6] The standard EC is able to produce IMPS spectra with only two arcs,[23] as shown in Figure S4. Therefore, we can conclude that the Standard EC is too simple for explaining complex spectra with more features, as remarked in the literature.[9]

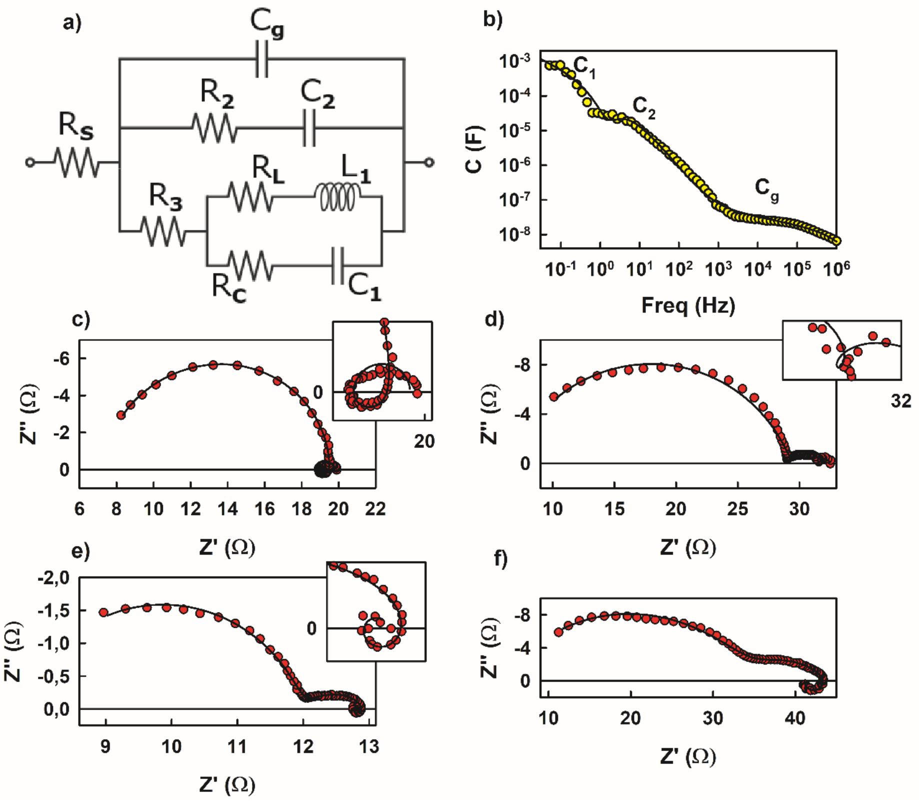

Figure 3. (a) Equivalent circuit for the data fitting of IS of carbon-based perovskite solar cells. (b) Capacitance-frequency plot of Cell 2 showing three capacitances at different frequencies. (d-f) Impedance complex plots at open circuit conditions. Red and yellow points are experimental data, and the straight black line is the fitting given by the EC. (c) is for Cell 1, (d) and (e) are for Cell 2 and (f) is for Cell 3.

As remarked above, the observation of negative capacitance is very common, but the physical origin remains uncertain.[5, 13-15] One hypothesis is that the interaction of ionic and electronic effects generates delayed dynamics, either by charge accumulation at the interface[13] or by ionic redistribution controlling charge injection.[28] It may also be an intrinsic instability of the device during the time of measurement of IS[17] or only an apparent effect.[14] Based on these approaches, we adopt the model proposed by Ghahremanirad et al. for including the negative capacitance features in the EC,[13] shown in the lower branch of Figure 3a. This method is based on a surface polarization model[29] that provides a quantitative description of the slow dynamics associated with the ionic-electronic coupling at the interface. The model describes the evolution of an internal surface voltage V_s (related to interfacial polarization) towards equilibrium dictated by the external voltage V and the built-in potential V_{bi} according to the relaxation equation

$$\frac{dV_s}{dt} = -\frac{V_s - (V - V_{bi})}{\tau_{kin}} \tag{1}$$

The EC parameters (including the inductor element) are determined from the physical parameters as described by Ghahremanirad et al.[13] The time constant τ_{kin} has been found in the range 1-10 s, and it has been linked to ionic binding phenomena at the interface.[30] This EC is able to fit both negative capacitances at low frequency and inductive loops at midfrequency values, and both features appear in the solar cells that we are presenting. However, this circuit is not able to reproduce midfrequency arcs like the circuit proposed by Ravishankar et al.[6] for IMPS and IS. Therefore, we propose in Figure 3a a generalized EC able to reproduce all these features, altogether.

The generalized EC has three parallel branches with three different capacitances that are able to generate three separated features. The elements are ordered according to the frequency in which they appear, i.e. number 1 goes with the lowest-frequency elements, and number 3 goes with the highest; number 2 is for midfrequency, following the established convention.[9] Figure 3b shows a capacitance-frequency (*C*-*f*) plot that clearly shows the appearance of three capacitances in the impedance measurements. This *C*-*f* plot corresponds to the impedance plot in Figure 3d. The proper functioning of the circuit is demonstrated in Figure 3c-f, where we can see how the same circuit gives a good fitting for a variety of spectra showing different phenomena at mid and low frequencies, such as inductive loops, midfrequency arcs or negative capacitances. Here, the red points are the experimental data measured for different cells, at different illuminations and at open-circuit voltage, and the straight line is the fitting given by the EC in Figure 3a.

By being able to fit all these different spectra, this EC proves to be appropriate for the study of perovskite solar cells. From the fitted spectra, we can extract some conclusions. In Figure 4a (orange), we can see that the value of C_2, i.e., the midfrequency capacitance, depends on the cell thickness. The values are several orders of magnitude lower for Cell 1, in comparison with Cell 2 and Cell 3, which have much thicker perovskite layers. In contrast, C_1 (yellow) takes similar values for all the cells. This means that the intermediate frequency capacitance depends on the perovskite layer thickness, while the low-frequency capacitance does not and can be attributed to surface phenomena.[27] Moreover, if we look into the values of R_3 and R_2 (Figure 4b), we can clearly see that the high-frequency resistance does not depend on the thickness, while the midfrequency resistances are normally higher for Cells 2 and 3. Therefore, the midfrequency elements change with the perovskite thickness.

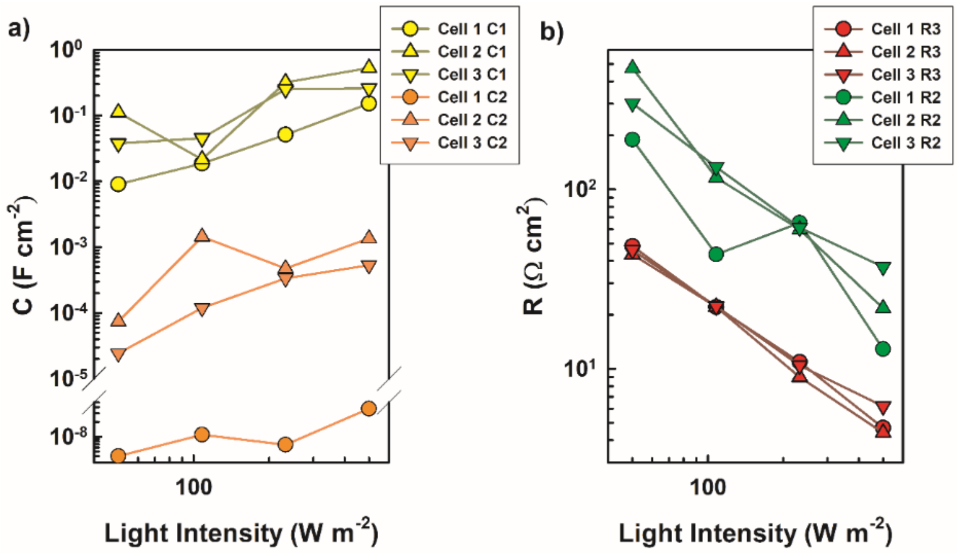

Figure 4. Values of C_1 and C_2 (a) and R_2 and R_3 (b) depending on the light intensity for the three cells.

The resistances and the arcs from IS spectra vary from one cell to another. However, the evolution of all the resistances in one cell with voltage is similar for all the resistances. Therefore, there is a concordance with all the resistances in each cell. This can be seen in Figure S5.

Coming back to Figure 1, when comparing IS and IMVS spectra, the similarities are easily seen. Interestingly, we have found that the IMVS spectra are similar to the IS spectra in the number and the type of characteristics they have, although they are not exactly equal. Moreover, the low-frequency features, which are key for the correct understanding of perovskite solar cell operation, seem to be amplified and more easily distinguishable. Therefore, IMVS can help support the results obtained in IS measurements as well as improve the analysis of those mid- and low-frequency loops and arcs.

The fact that we are doing all measurements under the same conditions, and the three measurement perturbation variables (V, j_e and j_{ph}) appear in pairs in the three different techniques, suggests that the three techniques may be linked. This has been previously suggested for dye-sensitized solar cells[31] and shown with a general derivation by Bertoluzzi et al.[25] When taken in the same conditions, the three techniques are related by the following equation:

$$Q(\omega) = \frac{W(\omega)}{Z(\omega)} \tag{2}$$

Therefore, if the measurements are correct, the values for the IMPS transfer function Q should be similar when obtained directly from the measurement and by calculating it from eq 2.

We have calculated IMPS transfer function Q by dividing IMVS and IS transfer functions, W and Z, respectively, for each cell. The comparison between the IMPS experimental transfer function from direct measurements and the IMPS calculated transfer function from W and Z is shown in Figure S6. For all cells, both experimental and calculated spectra have the same number of features with similar shapes. This result indicates the good relation between the techniques, giving truthfulness to the results obtained in these measurements.

In summary, we have measured IS in three similar perovskite solar cells with only one difference: the perovskite layer thickness. From the measurements, we conclude that the effects of the intermediate frequency features are amplified by the perovskite thickness as well as the negative capacitance, which is bigger in the thickest cell. Based on the measurements of IMPS and IMVS in perovskite solar cells that show negative capacitance in IS measurements, we have been able to see how this feature manifests in IMPS and IMVS spectra. In the case of IMPS, we see how the fourth quadrant low-frequency common feature ends up coming back to the first quadrant. Regarding IMVS, the spectra look similar to those of IS. We have built an EC for impedance spectra of perovskite solar cells that is able to reproduce and explain intermediate frequency arcs, inductive loops, and negative capacitances. This EC is based on previous studies that have explained these features separately, and here, we aim to unify this feature in one complete EC. Moreover, it has been able to fit a wide variety of spectra shown by a group of perovskite solar cells. Finally, we have checked the relation between the transfer functions of the three techniques by dividing IMVS and IS transfer functions, obtaining a calculated IMPS transfer function, which is comparable with the measured IMPS spectra.

Acknowledgments

J.B. and A.B. thank Ministerio de Ciencia e Innovación of Spain for support of this work in the project PID2019-107348GB-100. A.B. thanks Ministerio de Ciencia e Innovación of Spain for FPI Fellowship (BES-2017-080351). A.P., D.R., T.W. and M.C. would like to thank the EPSRC (EP/N020863/1, EP/R032750/1, EP/M015254/2, EP/P032591/1), the Welsh European Funding Office (SPARC II) and the Welsh Government’s Sêr Solar programme for funding.

Supporting Information

Experimental details on device preparation, schematic illustration of the devices, and characterization methods. J-V characteristics of devices. Detailed IS measurements. IS, IMPS, and IMVS simulations with ECs. Resistance-Voltage Plots extracted from IS fittings. IMPS comparison figure.

References

1. Bisquert, J.; Bertoluzzi, L.; Mora-Sero, I.; Garcia-Belmonte, G., Theory of Impedance and Capacitance Spectroscopy of Solar Cells with Dielectric Relaxation, Drift-Diffusion Transport, and Recombination. *The Journal of Physical Chemistry C* **2014**, *118*, 18983-18991.

2. Guillén, E.; Ramos, F. J.; Anta, J. A.; Ahmad, S., Elucidating Transport-Recombination Mechanisms in Perovskite Solar Cells by Small-Perturbation Techniques. *The Journal of Physical Chemistry C* **2014**, *118*, 22913-22922.

3. Miyano, K.; Yanagida, M.; Tripathi, N.; Shirai, Y., Simple Characterization of Electronic Processes in Perovskite Photovoltaic Cells. *Applied Physics Letters* **2015**, *106*, 093903.

4. Todinova, A.; Contreras-Bernal, L.; Salado, M.; Ahmad, S.; Morillo, N.; Idígoras, J.; Anta, J. A., Towards a Universal Approach for the Analysis of Impedance Spectra of Perovskite Solar Cells: Equivalent Circuits and Empirical Analysis. *ChemElectroChem* **2017**, *4*, 2891-2901.

5. Jacobs, D. A.; Shen, H.; Pfeffer, F.; Peng, J.; White, T. P.; Beck, F. J.; Catchpole, K. R., The Two Faces of Capacitance: New Interpretations for Electrical Impedance Measurements of Perovskite Solar Cells and Their Relation to Hysteresis. *Journal of Applied Physics* **2018**, *124*, 225702.

6. Ravishankar, S.; Aranda, C.; Sanchez, S.; Bisquert, J.; Saliba, M.; Garcia-Belmonte, G., Perovskite Solar Cell Modeling Using Light- and Voltage-Modulated Techniques. *The Journal of Physical Chemistry C* **2019**, *123*, 6444-6449.

7. Klotz, D.; Tumen-Ulzii, G.; Qin, C.; Matsushima, T.; Adachi, C., Detecting and Identifying Reversible Changes in Perovskite Solar Cells by Electrochemical Impedance Spectroscopy. *RSC Advances* **2019**, *9*, 33436-33445.

8. Futscher, M. H.; Lee, J. M.; McGovern, L.; Muscarella, L. A.; Wang, T.; Haider, M. I.; Fakharuddin, A.; Schmidt-Mende, L.; Ehrler, B., Quantification of Ion Migration in Ch3nh3pbi3 Perovskite Solar Cells by Transient Capacitance Measurements. *Materials Horizons* **2019**, *6*, 1497-1503.

9. Guerrero, A.; Garcia-Belmonte, G.; Mora-Sero, I.; Bisquert, J.; Kang, Y. S.; Jacobsson, T. J.; Correa-Baena, J.-P.; Hagfeldt, A., Properties of Contact and Bulk Impedances in Hybrid Lead Halide Perovskite Solar Cells Including Inductive Loop Elements. *The Journal of Physical Chemistry C* **2016**, *120*, 8023-8032.

10. Zohar, A.; Kedem, N.; Levine, I.; Zohar, D.; Vilan, A.; Ehre, D.; Hodes, G.; Cahen, D., Impedance Spectroscopic Indication for Solid State Electrochemical Reaction in (Ch3nh3)Pbi3 Films. *The Journal of Physical Chemistry Letters* **2016**, *7*, 191-197.

11. Anaya, M.; Zhang, W.; Hames, B. C.; Li, Y.; Fabregat-Santiago, F.; Calvo, M. E.; Snaith, H. J.; Míguez, H.; Mora-Seró, I., Electron Injection and Scaffold Effects in Perovskite Solar Cells. *Journal of Materials Chemistry C* **2017**, *5*, 634-644.

12. Fabregat-Santiago, F.; Kulbak, M.; Zohar, A.; Vallés-Pelarda, M.; Hodes, G.; Cahen, D.; Mora-Seró, I., Deleterious Effect of Negative Capacitance on the Performance of Halide Perovskite Solar Cells. *ACS Energy Letters* **2017**, *2*, 2007-2013.

13. Ghahremanirad, E.; Bou, A.; Olyaee, S.; Bisquert, J., Inductive Loop in the Impedance Response of Perovskite Solar Cells Explained by Surface Polarization Model. *The Journal of Physical Chemistry Letters* **2017**, *8*, 1402-1406.

14. Ebadi, F.; Taghavinia, N.; Mohammadpour, R.; Hagfeldt, A.; Tress, W., Origin of Apparent Light-Enhanced and Negative Capacitance in Perovskite Solar Cells. *Nat. Commun.* **2019**, *10*, 1574.

15. Klotz, D., Negative Capacitance or Inductive Loop? – a General Assessment of a Common Low Frequency Impedance Feature. *Electrochemistry Communications* **2019**, *98*, 58-62.

16. Taibl, S.; Fafilek, G.; Fleig, J., Impedance Spectra of Fe-Doped Srtio3 Thin Films Upon Bias Voltage: Inductive Loops as a Trace of Ion Motion. *Nanoscale* **2016**, *8*, 13954-13966.

17. Solanki, A.; Guerrero, A.; Zhang, Q.; Bisquert, J.; Sum, T. C., Interfacial Mechanism for Efficient Resistive Switching in Ruddlesden-Popper Perovskites for Non-Volatile Memories. *J. Phys. Chem. Lett.* **2020**, *11*, 463-470.

18. Pockett, A.; Eperon, G. E.; Peltola, T.; Snaith, H. J.; Walker, A.; Peter, L. M.; Cameron, P. J., Characterization of Planar Lead Halide Perovskite Solar Cells by Impedance Spectroscopy, Open-Circuit Photovoltage Decay, and Intensity-Modulated Photovoltage/Photocurrent Spectroscopy. *The Journal of Physical Chemistry C* **2015**, *119*, 3456-3465.

19. Mei, A., et al., A Hole-Conductor–Free, Fully Printable Mesoscopic Perovskite Solar Cell with High Stability. *Science* **2014**, *345*, 295.

20. Pockett, A.; Raptis, D.; Meroni, S. M. P.; Baker, J.; Watson, T.; Carnie, M., Origin of Exceptionally Slow Light Soaking Effect in Mesoporous Carbon Perovskite Solar Cells with Ava Additive. *J. Phys. Chem. C* **2019**, *123*, 11414-11421.

21. Bertoluzzi, L.; Sanchez, R. S.; Liu, L.; Lee, J.-W.; Mas-Marza, E.; Han, H.; Park, N.-G.; Mora-Sero, I.; Bisquert, J., Cooperative Kinetics of Depolarization in Ch3nh3pbi3 Perovskite Solar Cells. *Energy Environ. Sci.* **2015**, *8*, 910-915.

22. Rong, Y. G., et al., Tunable Hysteresis Effect for Perovskite Solar Cells. *Energy Environ. Sci.* **2017**, *10*, 2383-2391.

23. Ravishankar, S.; Riquelme, A.; Sarkar, S. K.; Garcia-Batlle, M.; Garcia-Belmonte, G.; Bisquert, J., Intensity-Modulated Photocurrent Spectroscopy and Its Application to Perovskite Solar Cells. *The Journal of Physical Chemistry C* **2019**, *123*, 24995-25014.

24. Ravishankar, S.; Aranda, C.; Boix, P. P.; Anta, J. A.; Bisquert, J.; Garcia-Belmonte, G., Effects of Frequency Dependence of the External Quantum Efficiency of Perovskite Solar Cells. *The Journal of Physical Chemistry Letters* **2018**, *9*, 3099-3104.

25. Bertoluzzi, L.; Bisquert, J., Investigating the Consistency of Models for Water Splitting Systems by Light and Voltage Modulated Techniques. *The Journal of Physical Chemistry Letters* **2017**, *8*, 172-180.

26. Pockett, A.; Eperon, G. E.; Sakai, N.; Snaith, H. J.; Peter, L. M.; Cameron, P. J., Microseconds, Milliseconds and Seconds: Deconvoluting the Dynamic Behaviour of Planar Perovskite Solar Cells. *Physical Chemistry Chemical Physics* **2017**, *19*, 5959-5970.

27. Zarazua, I.; Bisquert, J.; Garcia-Belmonte, G., Light-Induced Space-Charge Accumulation Zone as Photovoltaic Mechanism in Perovskite Solar Cells. *The Journal of Physical Chemistry Letters* **2016**, *7*, 525-528.

28. Moia, D., et al., Ionic-to-Electronic Current Amplification in Hybrid Perovskite Solar Cells: Ionically Gated Transistor-Interface Circuit Model Explains Hysteresis and Impedance of Mixed Conducting Devices. *Energy & Environmental Science* **2019**, *12*, 1296-1308.

29. Ravishankar, S.; Almora, O.; Echeverría-Arrondo, C.; Ghahremanirad, E.; Aranda, C.; Guerrero, A.; Fabregat-Santiago, F.; Zaban, A.; Garcia-Belmonte, G.; Bisquert, J., Surface Polarization Model for the Dynamic Hysteresis of Perovskite Solar Cells. *The Journal of Physical Chemistry Letters* **2017**, *8*, 915-921.

30. Wang, H.; Guerrero, A.; Bou, A.; Al-Mayouf, A. M.; Bisquert, J., Kinetic and Material Properties of Interfaces Governing Slow Response and Long Timescale Phenomena in Perovskite Solar Cells. *Energy & Environmental Science* **2019**, *12*, 2054-2079.

31. Halme, J., Linking Optical and Electrical Small Amplitude Perturbation Techniques for Dynamic Performance Characterization of Dye Solar Cells. *Physical Chemistry Chemical Physics* **2011**, *13*, 12435-12446.

Supporting Information

Beyond Impedance Spectroscopy in Perovskite Solar Cells: Correlation of Multiple Frequency Techiques

Agustín Bou[1], Adam Pockett*[2], Dimitrios Raptis[2], Trystan Watson[2], Matthew J. Carnie[2], Juan Bisquert*[1]

[1] Institute of Advanced Materials (INAM), Universitat Jaume I, 12006 Castelló, Spain

[2] SPECIFIC, Materials Research Center, College of Engineering, Swansea University, Bay Campus, Swansea SA1 8EN, UK

Email: bisquert@uji.es

Experimental methods

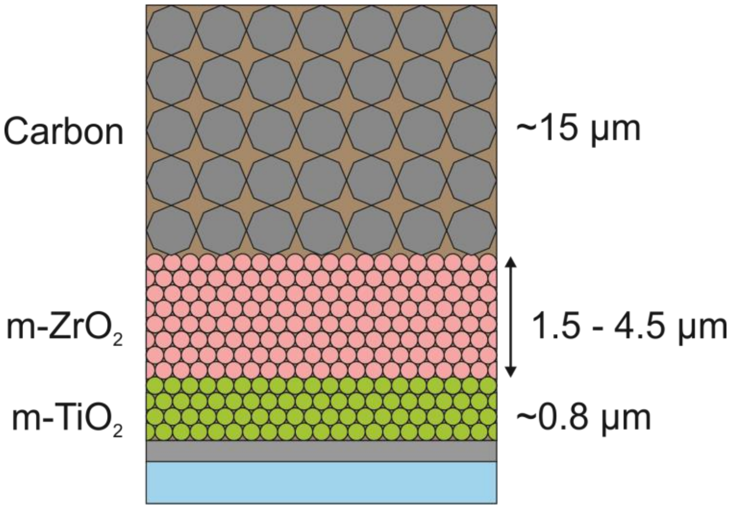

Figure S1. Scheme of the carbon cell. Brown colour represents the infiltrated perovskite through the mesoporous layers.

Materials: PbI_2 (99%, Sigma-Aldrich), MAI (CH_3NH_3I, anhydrous, Dyesol), 5-ammonium valeric acid iodide (5-AVAI, Dyesol) and γ-Butyrolactone (Sigma Aldrich) were used as received for preparation of perovskite precursors. Stacks were prepared using the following: anhydrous 2-propanol (IPA, 99.5%), carbon paste (Gwent electronic materials), ZrO_2 paste (Solaronix), TiO_2 paste (30NR-D, Dyesol), terpineol (95%, Sigma-Aldrich), and titanium diisopropoxide bis (acetylacetonate) (TAA, 75% in IPA, Sigma-Aldrich).

Device fabrication: The FTO substrate was initially patterned with a Nb:YVO4 laser (532nm), then cleaned with a solution of Hellmanex in deionised water, rinsed with acetone, IPA, and finally plasma cleaned in an O_2 atmosphere for 5 min. A compact TiO_2 blocking layer was sprayed with a solution of 10% Titanium di-isopropoxide bis (acetylacetonate) in IPA on the FTO substrate, which was kept at 300 ^oC on a hot plate. Mesoporous layers of TiO_2, ZrO_2, and carbon were sequentially screen printed. The annealing of each layer occurred at 550 ^oC for TiO_2, and 400 ^oC for ZrO_2 and carbon. For devices with double and triple ZrO_2, the layers were printed two and three times respectively after drying each printed layer at 100 ^oC. The paste for the TiO_2 layer was diluted in terpineol in a 1:1 ratio by weight. The other pastes were used as bought. The precursor perovskite solution was synthesized by dissolving 0.439 of PbI_2, 0.1514 of MAI and 0.0067 g of 5-AVAI in 1 ml γ-butyrolactone at 60 ^oC. In case of devices with one ZrO_2 layer, 15 μL of the solution drop casted on the 1 cm^2 active area of the cells through the carbon layer, while in the case of devices with double and triple ZrO_2 the amount of the infiltrated perovskite precursor solution was 20 and 25 μL respectively. Allowing 10 minutes time for the solution to percolate throughout the stack, the devices were annealed in a fan oven for 1 h at 50 ^oC. The finished solar cells were then exposed to 70% relative humidity at 40 °C for 24 hours to induce a recrystallisation and then dried in a vacuum oven before measuring to reach their final efficiency.

Films thicknesses were measured with a DEKTAK 150 profilometer system and found as follows (average values):

- Standard: ZrO_2=1.5 μm, total stack= 17 μm
- Double ZrO_2, ZrO_2=2.9 μm, total stack= 18.3 μm
- Triple ZrO_2, ZrO_2=4.5 μm, total stack= 19.5 μm

JV characterization: Masked devices (0.5 cm^2 were tested under a class AAA solar simulator (Newport Oriel Sol3A) at AM1.5 100 mW cm−2 illumination conditions (calibrated using a KG5 filtered reference cell) using a Keithley 2400 source meter. The devices were scanned from V_{oc} to J_{sc} and vice versa at a scan rate of 330 mV s^{-1}, after 3 min of light soaking.

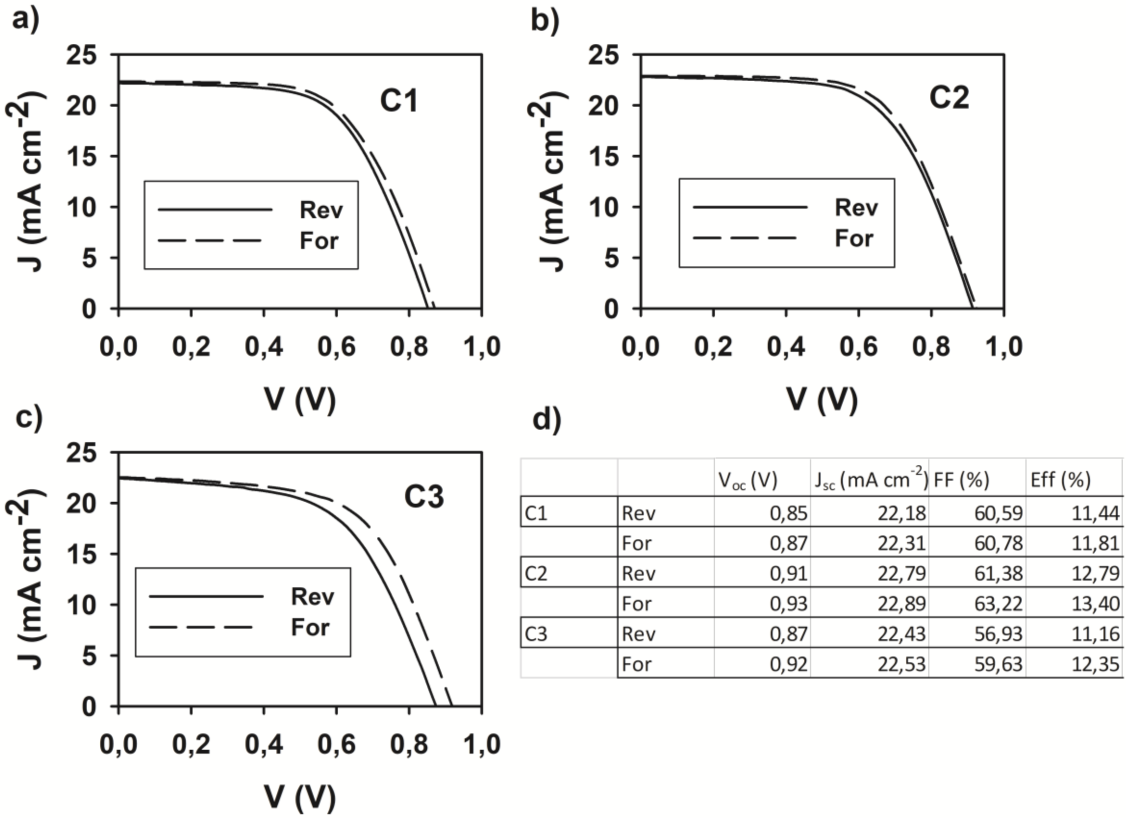

		V_{oc} (V)	J_{sc} (mA cm^{-2})	FF (%)	Eff (%)
C1	Rev	0,85	22,18	60,59	11,44
	For	0,87	22,31	60,78	11,81
C2	Rev	0,91	22,79	61,38	12,79
	For	0,93	22,89	63,22	13,40
C3	Rev	0,87	22,43	56,93	11,16
	For	0,92	22,53	59,63	12,35

Figure S2. J-V curves of Cell 1 (a), Cell 2 (b) and Cell 3 (c). (d) shows the characteristic values of J-V curves.

Characterization: Impedance spectroscopy (IS), intensity-modulated photocurrent spectroscopy (IMPS) and intensity-modulated photovoltage spectroscopy (IMVS) measurements were performed on unmasked devices using a Zahner CIMPS-X photoelectrochemical workstation with 630 nm LED illumination. The frequency range for these measurements was 1 MHz to 0.01 Hz and all the measurements were performed at open-circuit voltage.

Impedance Spectra

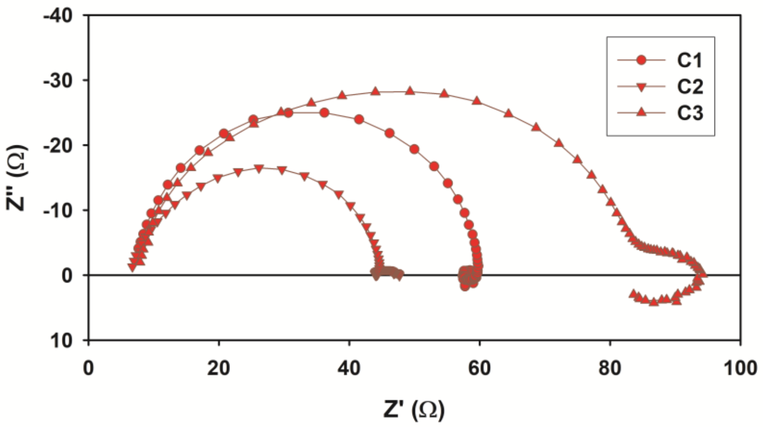

Figure S3. Impedance Spectroscopy complex plane plot for the Cell 1, Cell 2 and Cell 3 at open circuit conditions.

Standard Circuit Simulations

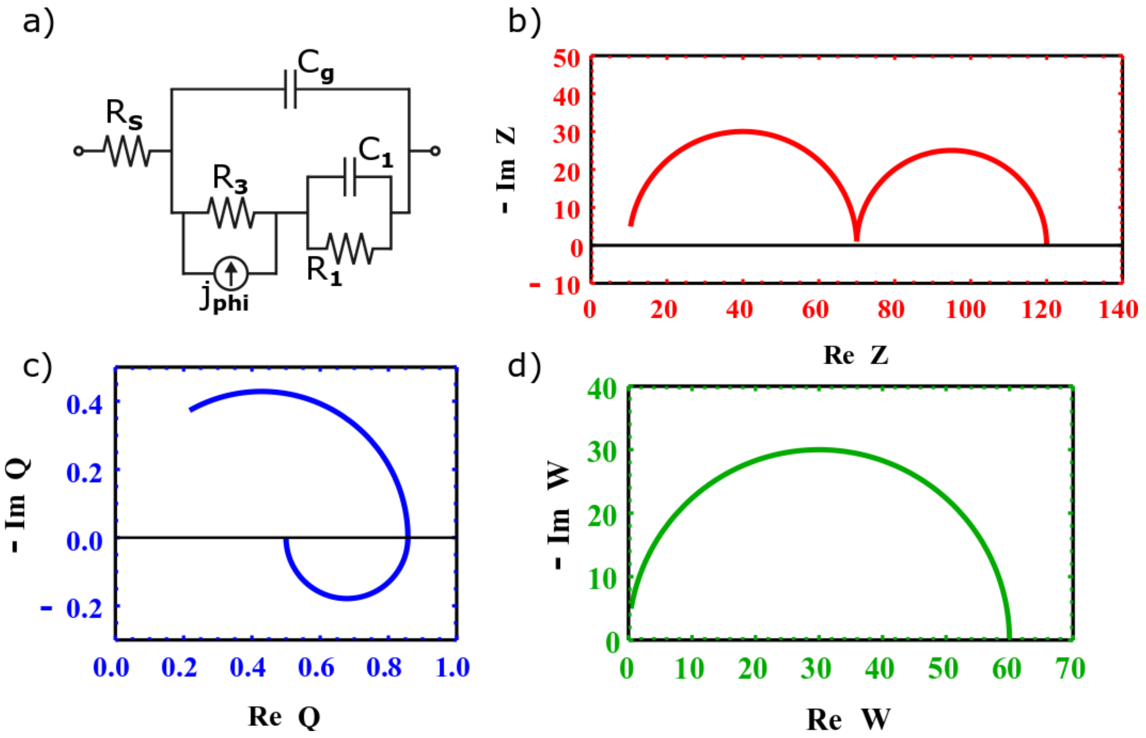

Figure S4. a) Standard EC shown in Figure 1 with the addition of the generator in parallel with R_3. The EC is accompanied by IS (b), IMPS (c) and IMVS (d) spectra for the following values of the circuit elements: $R_S = 10\Omega$, $C_g = 0.2\mu F$, $R_3 = 60\Omega$ and $R_1 = 50\Omega$, $C_1 = 1mF$.

Resistances from IS Fittings

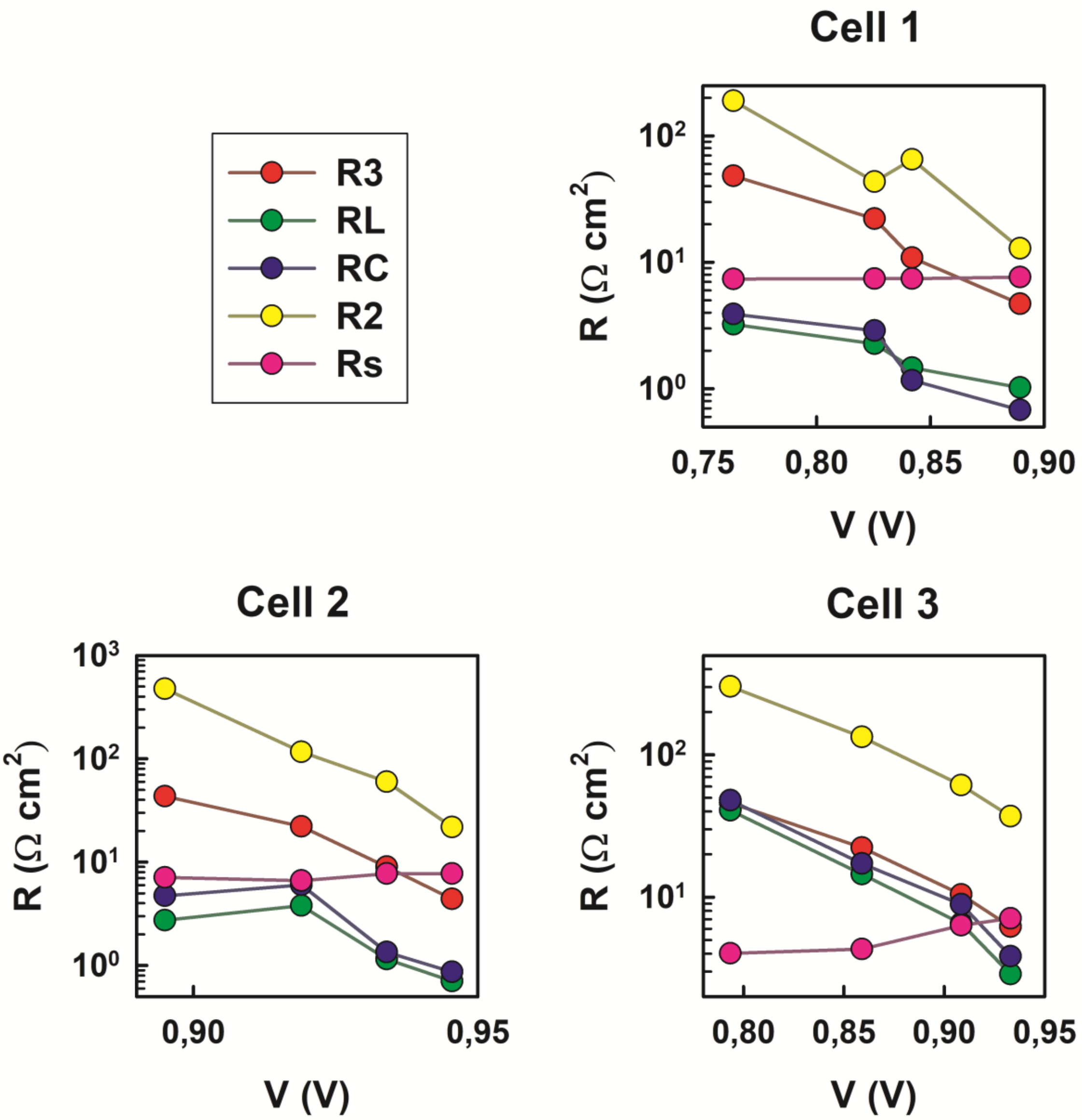

Figure S5. Resistance-Voltage plots, extracted from IS measurements.

Experimental vs Calculated IMPS Transfer Function

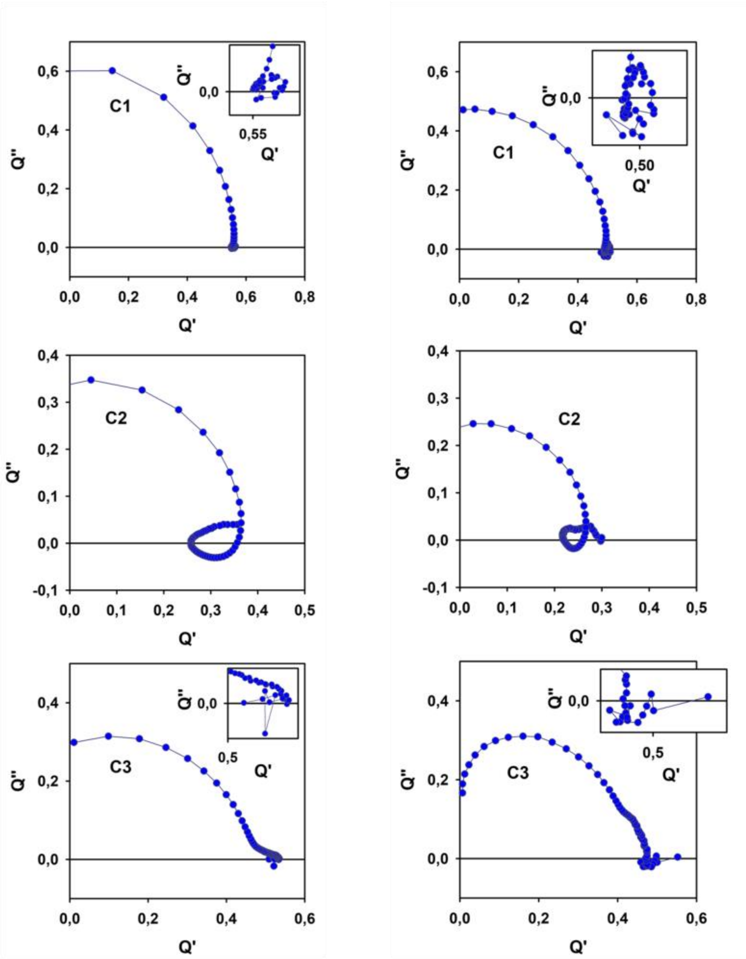

Figure S6. Experimental IMPS complex plane plots (left) vs Calculated IMPS complex plots (right).

Chapter 3

Publication 2

Extracting *in Situ* Charge Carrier Diffusion Parameters in Perovskite Solar Cells with Light Modulated Techniques

Bou, A.; Āboliņš, H.; Ashoka, A.; Cruanyes, H.; Guerrero, A.; Deschler, F.; Bisquert, J. Extracting *in Situ* Charge Carrier Diffusion Parameters in Perovskite Solar Cells with Light Modulated Techniques, *ACS Energy Letters,* **2021**, *6*, 2248-2255.

Candidate's Contribution

Nature of Contribution	Extent of Contribution
• Contributed to the calculation of transfer functions • Did part of the fitting and simulations • Linked the experimental traces with models • Built and designed several figures • Wrote part of the manuscript	50%

Introduction

This work achieves for the first time the extraction of charge carrier diffusion parameters of perovskites directly from small perturbation techniques. The method is based on the IMPS measurements of two kind of perovskite device configurations that present a non-uniform generation profile. The IMPS spectral shape is discussed in terms of the relation of different physical parameters.

Published Manuscript

Extracting *In-Situ* Charge Carrier Diffusion Parameters in Perovskite Solar Cells with Light Modulated Techniques

Agustín Bou[a], Haralds Āboliņš,[b] Arjun Ashoka,[b] Héctor Cruanyes,[a] Antonio Guerrero,[a] Felix Deschler,[c]* Juan Bisquert[a]*

Corresponding authors: Felix Deschler Felix.Deschler@wsi.tum.de, Juan Bisquert bisquert@uji.es

[a]Institute of Advanced Materials (INAM), Universitat Jaume I, Avda. Sos Baynat sn, 12006 Castelló, Spain
[b]Cavendish Laboratory, University of Cambridge, J.J. Thomson Avenue, CB3 0HE, Cambridge, United Kingdom
[c]Walter-Schottky-Institute, Physics Department, Technical University Munich, Am Coulombwall 4, Garching bei München, Germany

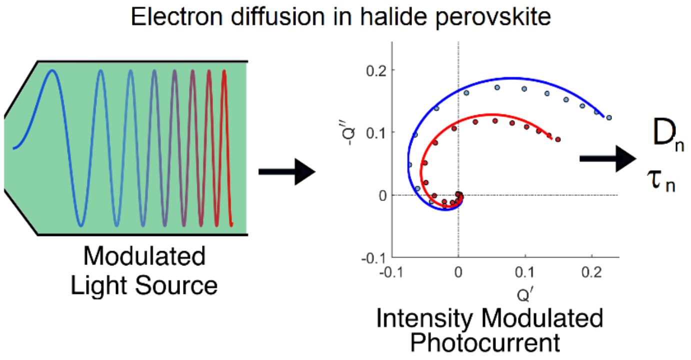

Abstract

Frequency resolved methods are widely used to determine device properties of perovskite solar cells. However, obtaining the electronic parameters for diffusion and recombination by impedance spectroscopy has been so far elusive, since the measured spectra do not present the diffusion of electrons. Here we show that Intensity Modulated Photocurrent Spectroscopy displays a high frequency spiraling feature determined by the diffusion-recombination constants, under conditions of generation of carriers far from the collecting contact. We present models and experiments in two different configurations: the standard sandwich-contacts solar cell device, and quasi-interdigitated back-contact (QIBC) device for lateral long-range diffusion. The results of the measurements produce the hole diffusion coefficient of $D_p = 0.029\ \mathrm{cm}^2/\mathrm{s}$ and lifetime of $\tau_p = 16\ \mu\mathrm{s}$ for one cell and $D_p = 0.76\ \mathrm{cm}^2/\mathrm{s}$, $\tau_p = 1.6\ \mu\mathrm{s}$ for the other. The analysis in the frequency domain is effective to separate the carrier diffusion (at high frequency) from the ionic contact phenomena at low frequency. This result opens the way for a systematic determination of transport and recombination features in a variety of operando conditions.

Metal halide perovskites (MHP) have raised enormous research efforts as a future high efficiency low-cost photovoltaic platform and also for various semiconductor electronics and photonics applications. Consequently, a priority of current research is the characterization of electronic parameters such as the electron diffusion coefficient, D_n, and the electron recombination lifetime, τ_n. There have been presented a large number of evaluations of the diffusion length $L_n = (D_n\tau_n)^{1/2}$ measured by time transient methods in the archetype perovskite solar cells (PSC) with methylammonium (MA) cation, namely $MAPbI_3$ and $MAPbBr_3$.[1,2] There have been also abundant determination of carrier mobilities by a range of techniques: Space-charge limited-current (SCLC), Hall effect, THz frequency measurements, etc. The results span a variety of values from D_n = 0.01 $cm^2\ s^{-1}$ to 4 $cm^2\ s^{-1}$.[3,4]

In this letter we address the observation of electronic diffusion characteristics in the framework of small perturbation frequency modulated techniques, that allow to study the full device operation in a wide range of scales from very low mHz frequencies to MHz phenomena. These methods yield us the important advantage that they can be applied in full efficient devices (in contrast to contactless methods such as THz spectroscopy) avoiding effects of ionic polarization that plague other techniques, as it has been well described recently,[5] provided that the diffusion effect is observed at high frequency, far from the low frequency ionic polarization. Therefore, it is important to find the spectral signatures of diffusion in PSCs.

As a reference, the diffusion of electrons was distinctly observed by Impedance Spectroscopy (IS)[6] and Intensity Modulated Photocurrent Spectroscopy[7] and these became dominant methods of analysis in dye solar cells. The diffusion effect is usually manifested as a 45° inclined line at high frequency in the complex plane representation of the spectra. This is the Warburg impedance with the square root dependence on the angular frequency as $Z(\omega) \propto (i\omega)^{-1/2}$, clearly indicating the presence of a diffusion transport resistance.[8] An enormous number of papers have analyzed the IS response of PSCs and such response has not been observed. The usual reason to explain the absence of such observation is that the transport resistance it too small due to the large electron mobility/diffusion coefficient, and becomes absorbed in the series resistance. Observations of low frequency Warburg elements in IS studies[9,10] have been attributed to ionic diffusion. There have been also a significant number of studies of MHP using IMPS,[11-16] but the spectral observation of Warburg features has not been achieved.

Often, the IMPS transfer function in MHP shows the curious feature that the spectra turn to real negative values (second quadrant) at high frequency, as indicated in Fig. 1. (It is different from the negative value observed at *very low frequency*.[17-19]) The high frequency feature has been often explained in the literature as the effect of *RC* attenuation,[7,11,14] that is, the large frequency negative feature is associated to the impedance of series and parallel elements in addition to diffusion. This type of effect is obviously uninteresting for the observation of diffusion. In any case, it provides a correction of the spectra by the impedance elements that can be measured independently. However, another effect associates a negative spiraling IMPS feature to the photocurrent created by carriers generated far from the collecting contact.[20,21] The observations of Fig. 1 indicate an opportunity where the diffusion-recombination effect dominates the frequency response of a PSC and enables the determination of the physical parameters. These experimental responses have been recently observed in a systematic fashion and related to negative transient photocurrent spikes.[22]

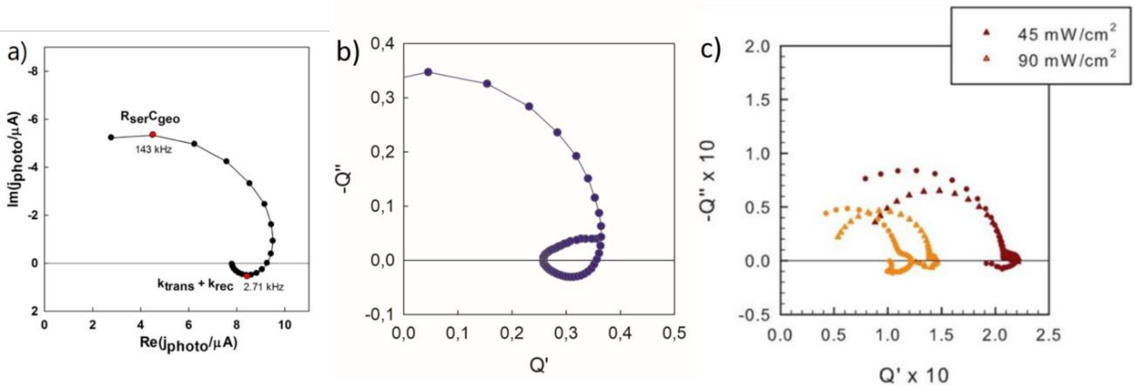

Figure 1. IMPS response for PSCs indicating an excursion to the second quadrant in the case of a and b, and staying in the first quadrant for c. a) Reproduced from [11]. b) Reproduced from [16]. c) Reproduced from [12].

Interestingly, the excursion to the second quadrant in Figure 1b, in which the real part of the IMPS transfer function becomes negative, is found in a configuration with a large perovskite layer that provokes a non-uniform generation profile. In this case, the generation profile is that represented in Figure 2a, where the generation of one kind of carriers is localized far away from their collecting contact. This is not the case of Figure 1c, where the thin film configuration allows the electron-hole pair generation to take place throughout the entire perovskite layer, and then the IMPS real part remains positive up to high frequency.

In this paper we will carry out a systematic investigation of models and experiments on the high frequency negative loop in the diffusion-recombination systems applied to halide perovskite solar cells. We derive the model for two independent experimental configurations, indicated in Fig 2: the standard sandwich solar cell for diffusion perpendicular to the electrodes, Fig. 2a, and a quasi-interdigitated back-contact (QIBC) for lateral diffusion, Fig. 2b.[23] This last structure has also been used by multiple groups for the fabrication of all back contacted solar cells with efficiencies up to 11.2%.[24-30] A number of papers have studied lateral diffusion of electronic carriers in perovskites, using time transient methods.[31-33] Excitation frequency-dependent photocurrent studies on QIBC devices have, however, never been performed, and could yield valuable insights on charge carrier dynamics for both a better understanding of intrinsic material and interface properties, as well as optimization of the back-contact structures for even higher efficiency solar cells. We show that electron diffusion coupled to recombination is clearly observed in both methods, and we provide a fitting method that allows us to extract the main parameters.

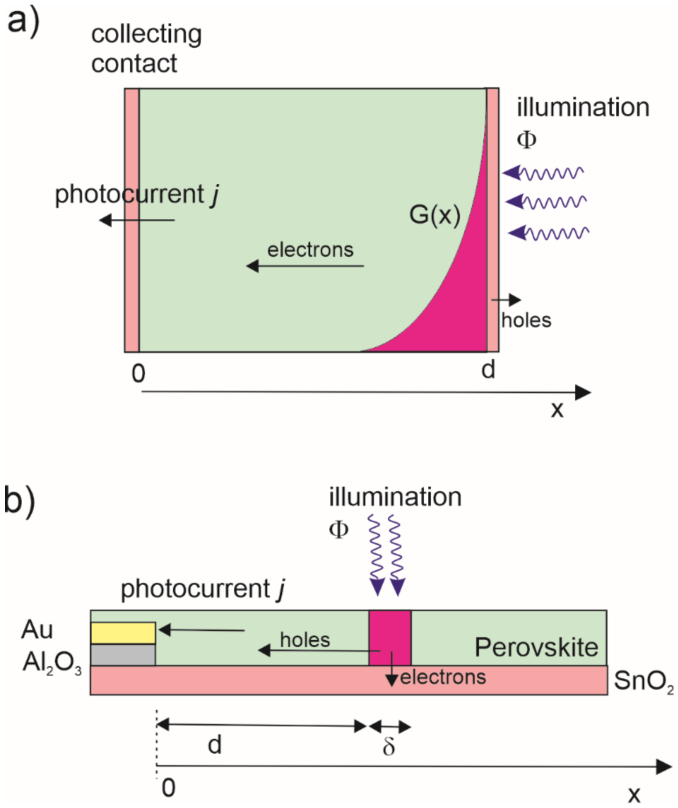

Figure 2. Scheme of the IMPS measurement for illumination far from the collecting contact. (a) The solar cell configuration. (b) Planar sample with lateral contact illuminated from above.

Method 1. Diffusion between parallel contacts.

The analysis of the IMPS spectra requires to solve the system of the scheme of Fig. 2a. Incident photon flux Φ arrives at the solar cell at $x = d$. The equation for the excess electron density n (over the equilibrium concentration n_0) is

$$\frac{\partial n}{\partial t} = D_n \frac{\partial^2 n}{\partial x^2} - \frac{n}{\tau_n} + G(x,t) \tag{1}$$

where $G(x) = \alpha\, \Phi \exp\,(\alpha(x-d))$ is an exponential profile of generation dependent on the absorption coefficient α. The boundary conditions at short-circuit conditions are $n(x=0) = 0$ and

$$\frac{\partial n}{\partial x}(x = d) = 0 \tag{2}$$

The photocurrent density j_e at the collecting contact at $x = 0$ is

$$j_e(x = 0) = +qD_n \frac{\partial n}{\partial x} \tag{3}$$

The IMPS transfer function $Q(\omega) = Q'(\omega) + iQ''(\omega)$ is obtained by the quotient of the small modulated input/output

$$Q = \frac{\tilde{J}_e}{q\tilde{\Phi}} \tag{4}$$

This problem is solved in Ref. [7] and a broad variety of illumination conditions are presented in [21]. For the sake of completion, we describe the solution in SI. The result is

$$Q(\omega) = \frac{1 - e^{-\alpha d}\left[e^{\frac{zd}{L_n}} + \left(\frac{z}{L_n\alpha} - 1\right)\sinh\left(\frac{zd}{L_n}\right)\right]}{\left[1 - \left(\frac{z}{L_n\alpha}\right)^2\right]\cosh\left(\frac{zd}{L_n}\right)} \tag{5}$$

where

$$z(\omega) = (1 + i\omega\tau_n)^{1/2} \tag{6}$$

The shapes of the IMPS spectra generated by Eq. (5) depend on the light absorbance mode and the diffusion-recombination features of the material. The physical parameters for absorbance and extraction affecting the form of the spectra are the light absorption length, α^{-1}, and the diffusion length, L_n, respectively. These parameters transform the spectral shape depending on whether they are shorter or longer than the cell thickness d, and the different kind of spectra that are obtained are shown in Figure 3. In the spectra we show the characteristic time constants[8] for diffusion across the layer thickness

$$\omega_d = \frac{D_n}{d^2} \tag{7}$$

and for recombination

$$\omega_{rec} = \tau_n^{-1} \tag{8}$$

Note the proportions between characteristic distances and frequencies

$$\frac{\omega_d}{\omega_{rec}} = \left(\frac{L_n}{d}\right)^2 \tag{9}$$

A Warburg-like spectral feature at high frequencies $(i\omega)^{-1/2}$ is obtained when the light is generated across the full thickness ($\alpha^{-1} > d$), either for short or long L_n (top row of Fig. 3). In the bottom rows, it is noted that looping spectra producing a negative Q' at high frequency (NHF) appear only when the absorption length is much shorter than the cell thickness. Another required condition for this feature is the diffusion length being longer than the absorption. These conditions are expressed respectively $\alpha^{-1} \ll d$, and $\alpha^{-1} < L_n$. Then, loops appear in the $\alpha^{-1} < d < L_n$ case and also in the $\alpha^{-1} < L_n < d$ case. This analysis confirms that the NHF loop is associated to collection of charges generated only far from the collecting contact. When the light is absorbed in a distance comparable to that of the cell (second row), no negative values of Q' are obtained but the spectra turn from Warburg like into a semicircle as the L_n increases.

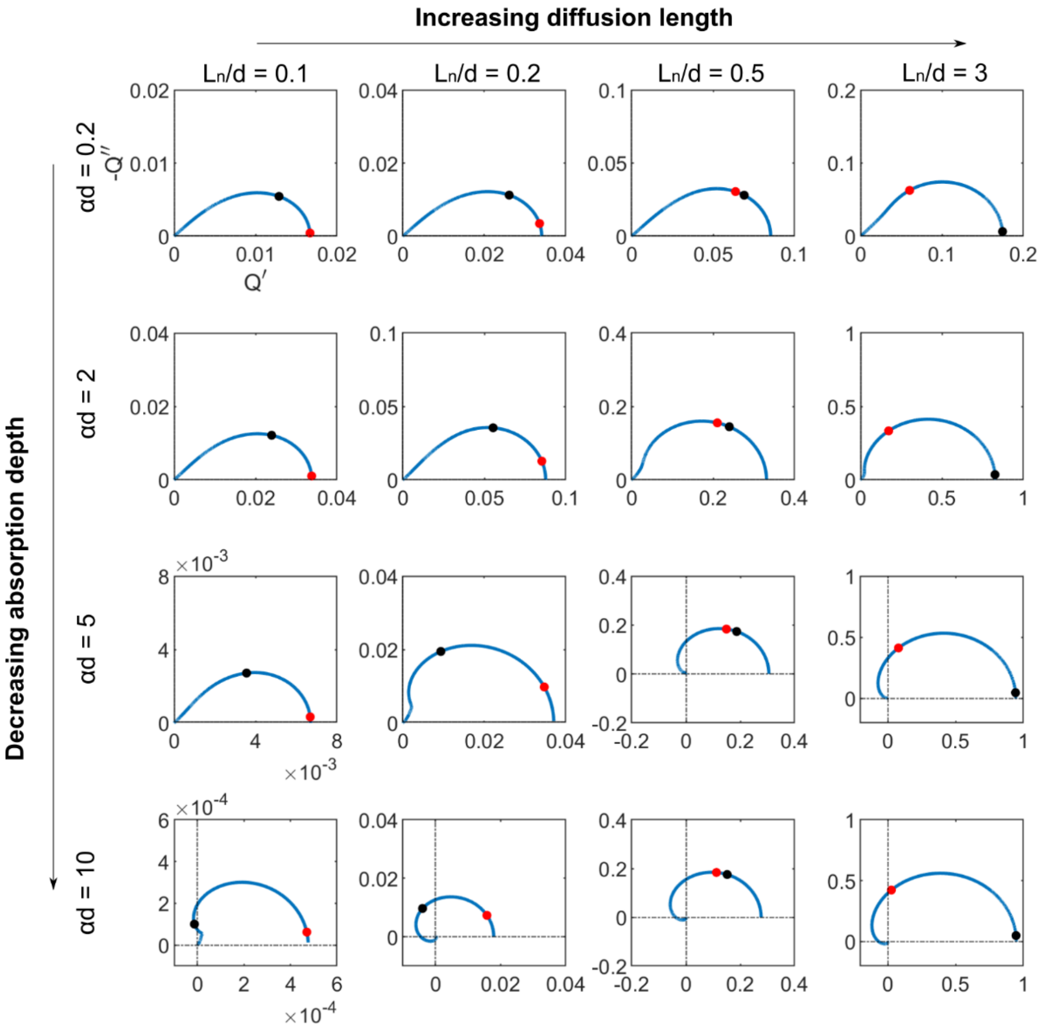

Figure 3. Complex plane plots of the IMPS transfer function for several relative values of light absorption distance and diffusion length. Rows are for equal absorption length and columns for equal diffusion length. Red points indicate the characteristic time constant for diffusion, $\omega_g = (\pi^2/2)D_n/d^2$, and the black ones are the characteristic time for recombination, $\omega_{rec} = 1/\tau_n$. No *RC* attenuation is considered.

To better appreciate the analytical shape of the function of interest we present in the Supporting Information some approximations that can be obtained when the diffusion length is longer that the cell thickness ($L_n > d$) and the light is completely absorbed in a short region. The high frequency limit is

$$Q(\omega) \approx \frac{2}{\left(1 - i\omega\tau_n \frac{1}{L_n^2\alpha^2}\right)} \exp\left(-\frac{d}{L_n}\sqrt{i\omega\tau_n}\right) \qquad (10)$$

The spectral dependences of this function are shown in Figure SI.1. The complex exponential function that depends on $\sqrt{i\omega\tau_n}$ is the one that loops and spirals into the negative Q' axis.

In order to understand the negative values of the real part of the transfer function Q, we calculated the excess charge carrier concentration $\tilde{n}$ along the cell associated to the small ac illumination, see the analytical expressions in the Supporting Information. We choose different representative regions of frequencies in the characteristic spectrum with the NHF loop, shown in Fig. 4.

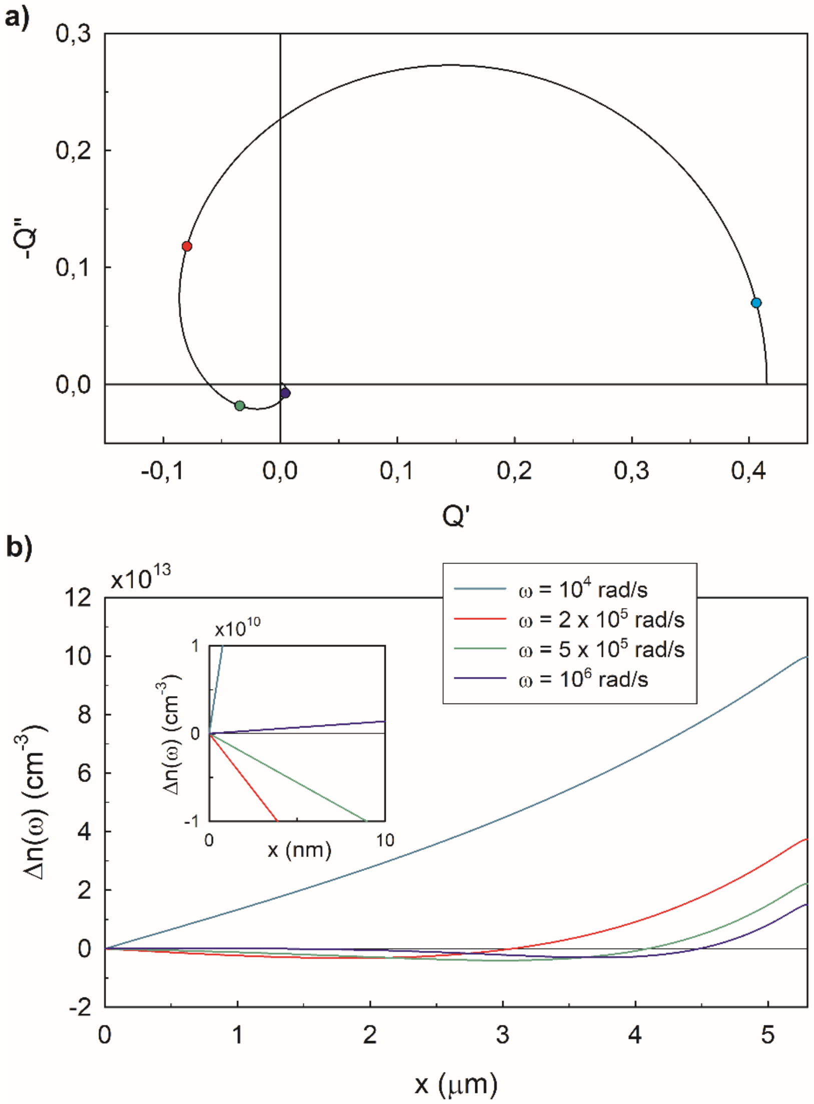

Figure 4. (a) IMPS complex plane plot for $\alpha d = 10$ and $L_n/d = 1/2$, indicating the angular frequencies for the concentration profiles in (b). (b) Plot of the spatial distribution of $\Delta n = \tilde{n}(\omega, x)$, the excess charge carrier concentration induced by an ac flux perturbation of $\tilde{\Phi} = 1.58 \cdot 10^{15}$ s^{-1}cm^{-2}, for an angular frequency representative of each quadrant, as indicated in (a), inset zooms the region close to the contact at $x = 0$.

The excess carrier concentration profiles at the frequencies of different quadrants, as indicated in Fig. 4a, are shown in Fig. 4b. The extracted current is proportional to the gradient of carrier concentration at the contact. We observe that the frequencies in the first and fourth quadrants give a positive current, which agrees with a positive real value of Q'. In contrast, for frequencies in the second and third quadrants, the gradient is negative, meaning that we have a negative current, and thus, a negative real value of Q'. In summary according to Fig. 4 the negative Q' occurs because the carriers generated at the contact decay rapidly at high frequency and make an upturn before the arrival to the collecting contact.

As mentioned earlier, it has been suggested in the literature that the additional impedances in the solar cell can produce a negative loop in the measured IMPS response, Q_{meas}. The previous transfer function due to diffusion only is modified as

$$Q_{meas}(\omega) = A(\omega)\, Q(\omega) \tag{11}$$

In the case of series resistance R_s and geometrical capacitance C_g, the attenuation factor $A(\omega)$ is[7,21]

$$A(\omega) = \frac{1}{1+i\omega R_s C_g} \tag{12}$$

The RC attenuation can produce a considerable effect in high frequencies, as it can be seen in Figure SI2. The RC attenuation with high RC values turns positive theoretical IMPS responses into the Q' negative axis as it is seen in Figure SI.2a. This effect makes the loop and Warburg IMPS responses undistinguished, whether light is completely absorbed or not. However, due to the fact that the RC values can be measured by impedance spectroscopy technique, the RC attenuation can be controlled and removed to obtain the pure diffusion features.

In order to observe the diffusion-recombination parameters we take the results of IMPS previously published[16] for a mesoporous carbon-based perovskite solar cell of $d = 5.3\ \mu\text{m}$ illuminated with different wavelengths, related to the transport of holes. The data clearly show a large NHF loop feature as observed in Figure 5. The fit to Eq. (5) describes well the experimental data, including the spiraling feature to the origin at high frequency. We obtain values of $\tau_p = 16\ \mu\text{s}$ for the lifetime and a diffusion coefficient of $D_p = 0.029\ \text{cm}^2/\text{s}$ for the blue light fitting and values of $\tau_p = 20\ \mu\text{s}$ and $D_p = 0.034\ \text{cm}^2/\text{s}$ for red light, which are in agreement with the values for perovskite solar cells in the literature.[3] These values produce diffusion lengths of $L_p = 2.6\ \mu\text{m}$ and $L_p = 2.2\ \mu\text{m}$. These diffusion lengths match with the predictions from Figure 3, where we expected a diffusion length comparable to the length of the perovskite layer for looping spectra. As the value of the lifetime is much larger than the RC factor, the attenuation is not highly relevant in this case. It introduces a relative difference in the estimated values lower than 5% .

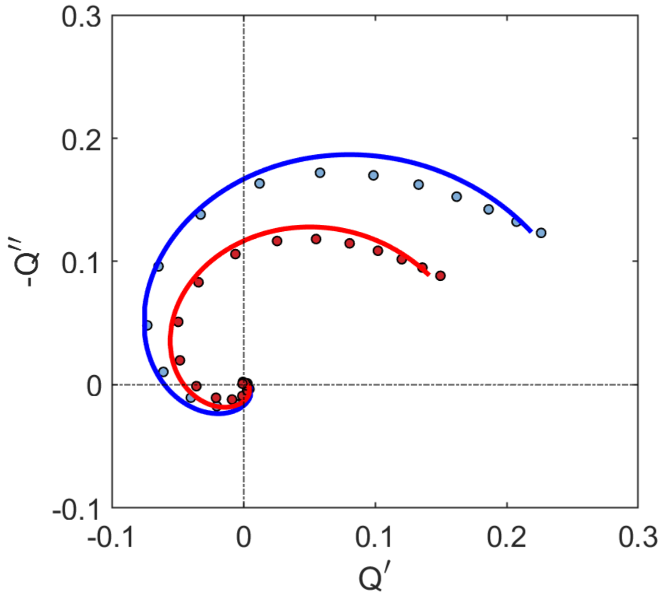

Figure 5. IMPS data (point) and fit (line) for a perovskite cell of 5.3 µm thickness illuminated with blue and red light, with estimated absorption length of 40 nm and 140 nm respectively.[34] The series resistance is 10 $\Omega\ cm^2$ and the geometrical capacitance is 36 nF cm^{-2} as determined by impedance spectroscopy. The effect of RC attenuation is negligible.

Method 2. Lateral diffusion

We consider the experimental configuration illustrated in Fig. 2b, measured on the quasi-interdigitated back-contact (QIBC) structure shown in Fig. 6. The QIBC configuration is particularly useful for the measurement of carrier diffusion, as upon local excitation of an electron-hole pair over either electrode, one carrier will be immediately extracted while the other will need to diffuse laterally towards its respective electrode over a distance much larger than the width of the excitation spot. Such measurements have been demonstrated in the past by Tainter et al.[23] It has also been shown by Lamboll et al. that is valid to treat diffusion as one-dimensional in photocurrent measurements on the QIBC device structure.[35]

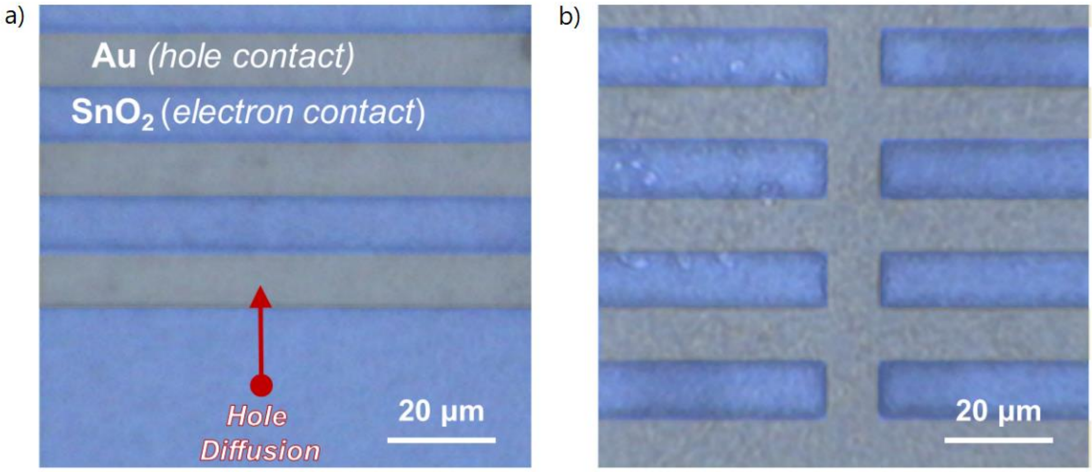

Figure 6. False-colour optical micrograph of the quasi-interdigitated back contact device structure used for measuring lateral diffusion. Here a pattern of an Al_2O_3/Au bilayer is formed on top of a continuous ITO/SnO_2 bilayer. A thin-film of perovskite is then deposited over the entire back-contact structure that remains visible under an optical microscope. Long-distance hole diffusion is measured by exciting carriers away from the last (hole-collecting) Au electrode (a) on the edge of the structure illustrated in (b).

Here a sample with a back contacted geometry is illuminated from above by a pulsed laser with a variable excitation frequency. Charges are generated in a spot of thickness δ at a distance d from the collecting contact, as illustrated in Fig. 2b and Fig. 6a. The photogenerated electrons are immediately extracted through the underlying SnO_2 layer, while the holes need to diffuse laterally over a distance d to reach the nearest gold electrode. The experimental setup is described in more detail in the Supplementary Information. Here we provide a theoretical model for this experiment. We solve Eq. (1) with the generation profile $G(x) = \beta^{-1}\Phi$,where β is an absorption coefficient, only for $d \leq x \leq d + \delta$, and $G(x) = 0$ elsewhere. The boundary condition is $n(x = 0) = 0$. This problem is solved in the SI and the result is

$$Q(\omega) = \frac{1}{\frac{L_p}{\beta z D_p}\sinh\left(\frac{zd}{L_p}\right) + \frac{1}{\beta\delta}e^{\frac{zd}{L_p}}} \tag{13}$$

The IMPS function is plotted for different cases of the diffusion length in Figure 7. Loops appear whatever the chosen diffusion length is. In the low diffusion length case, a shell shape is obtained. A small value of the EQE is obtained as the carriers are mainly recombined in the material. The IMPS function crosses over to the second quadrant with a complex exponential dependence like the dependences of the first method. When we increase the diffusion length, the EQE increases as the carriers easily diffuse in the sample. The shapes become longer than higher, but the function still leaves the first quadrant spiraling to the origin as in the other cases.

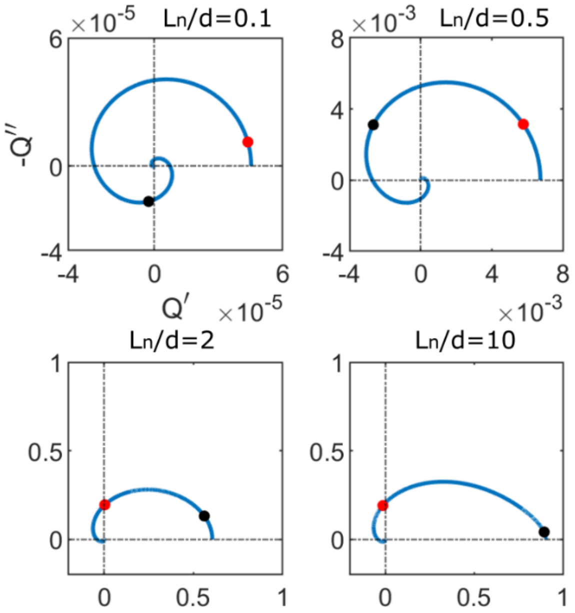

Figure 7: Complex plane IMPS function plots for different diffusion lengths. The absorption depth has been fixed to $\beta^{-1} = 0.01\ \mu m$ and the diffusion length also, $L_n = 1\ \mu m$. The cell thickness is considered to be the same as the absorption depth. The characteristic time constants are defined in Fig. 3.

For the analysis of the data the diffusion transfer function is complemented by other standard elements:[36] R_s series resistance, R_{HF} high-frequency resistance, C_g geometrical capacitance. The overall transfer function can then be written as in Eq. (11) with the attenuation factor:

$$A(\omega) = \left(1 + \frac{R_s}{R_{HF}} + i\omega R_s C_g\right)^{-1} \qquad (14)$$

The measured IMPS spectrum from the configuration in Fig. 2b exciting 10 μm away from the collecting electrode is shown in Fig. 8, along with a fit to the product of Equations (13) and (14). Importantly, in the regime of excitation far away from the collecting electrode and $L_p \approx d$ we can again clearly observe an NHF loop indicating a strong diffusive contribution to the IMPS spectrum. The fitting details are described in the Supplementary Information. From the fit we extract $L_p = 11$ μm, $\tau_p = 1.6$ μs and a corresponding $D_p = 0.76\ \mathrm{cm}^2/\mathrm{s}$. These values are once again consistent with those reported previously in literature, and the improvement in diffusivity can be attributed to the use of a triple cation, mixed halide perovskite in the back contacted configuration as opposed to $MAPbI_3$ in the sandwich structure. In particular the correspondent room-temperature hole mobility $\mu_p = 30\ \mathrm{cm}^2\ \mathrm{V}^{-1}\ \mathrm{s}^{-1}$ measured here shows good correspondence to the combined electron and hole mobility ($\mu = \mu_p + \mu_e$) obtained for $MAPbI_3$ polycrystalline thin films by THz spectroscopy, which also measures in-plane movement of charge carriers, where $\mu = 33$ cm^2 V^{-1} s^{-1}.[4] The hole mobility being higher by roughly a factor of two for the measurement in this study can once again be attributed to triple cation mixed halide perovskite composition used instead of MAPbI$_3$.

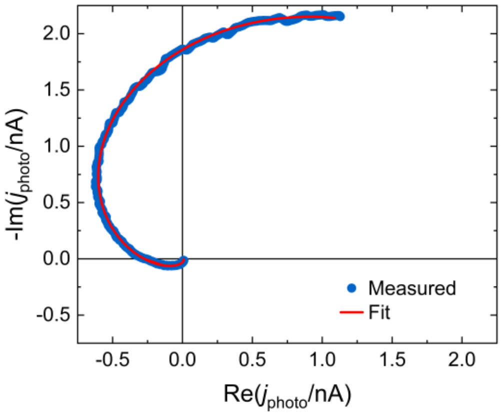

Figure 8. IMPS data (point) and fit (line) for a back contacted perovskite cell excited by a ~1 µm wide pulsed laser illumination spot 10 µm away from the nearest hole collecting electrode.

Now that we have completed the description of measurement and data analysis let us discuss the significance for a better understanding of halide perovskite solar cells. In Fig. 5 and 8 we have shown the measured data for the range of frequencies that obey the diffusion model. As mentioned, the data are affected by some additional electrical elements R_s, R_{HF} and C_g. These elements form part of a wider equivalent circuit that includes additional elements that describe also the low frequency data. The equivalent circuit for perovskite solar cells including the required elements has been discussed in other publications,[16,36] and a full spectrum showing the low frequency features is shown in Fig. SI.3 and SI.4. The remarkable fact is that the diffusion part of the spectra in Fig. 5 is nicely separated from the low frequency arcs that relate to surface recombination and ionic polarization. In other measurement methods for the diffusion parameters in a full device, for example the SCLC, it is unavoidable that measured dc current is influenced by the state of the contacts (especially by the application of large voltages).[5] The high frequency IMPS method has the unique feature that it is applied in an operating device but it is not strongly affected by the conditions of contacts. Nevertheless, the overall polarization can form an electrical field and charge extraction conditions, and produce modifications that modify the IMPS measurement. The method is then a powerful tool to investigate in situ the mechanisms of transport and recombination. An exploration of these more complex conditions is left for future investigations.

In summary, we have associated a negative loop spiraling to the origin of IMPS transfer function at high frequencies, to the generation of electronic carriers in a thin region and the subsequent transport across the sample thickness to the collecting contact. This spectrum occurs under the conditions (1) the absorption length is much shorter than the cell thickness and (2) is the diffusion length is longer than the absorption distance. We showed that the application of diffusion-recombination models enables a quantitative determination of the carrier diffusion coefficient and lifetime. This is the first consistent determination of electron diffusion by small amplitude spectral method, since these features have not been obtained in Impedance Spectroscopy and emerge in Intensity Modulated Photocurrent Spectroscopy.

Supporting Information

The Supporting Information is available free of charge at https://pubs.acs.org/doi/10.1021/acsenergylett.1c00871.

Calculation of IMPS function for sandwich configuration and for lateral transport, fitting of experimental data, spectral shapes of limiting functions, RC attenuation, full spectral shape, material preparation methods.

Acknowledgments

We thank Ministerio de Ciencia y Innovación (PID2019-107348GB-100) and the ERC (Grant No. 716471, ACrossWire). A.B. acknowledges FPI studentship funding from Ministerio de Ciencia e Innovación of Spain (BES-2017-080351). A.A acknowledges studentship funding from the Cambridge Trust and the Inlaks Shivdasani Foundation. H.A. acknowledges studentship funding from the EPSRC and the Winton Programme for the Physics of Sustainability. F.D. acknowledges funding from the Winton Program for the Physics of Sustainability and the DFG Emmy Noether Program.

References

(1) Stranks, S. D.; Eperon, G. E.; Grancini, G.; Menelaou, C.; Alcocer, M. J. P.; Leijtens, T.; Herz, L. M.; Petrozza, A.; Snaith, H. J. Electron-Hole Diffusion Lengths Exceeding 1 Micrometer in an Organometal Trihalide Perovskite Absorber, *Science* **2013**, *342*, 341-344.

(2) Dong, Q.; Fang, Y.; Shao, Y.; Mulligan, P.; Qiu, J.; Cao, L.; Huang, J. Electron-hole diffusion lengths; 175 μm in solution-grown $CH_3NH_3PbI_3$ single crystals, *Science* **2015**, *347*, 967-970.

(3) Herz, L. M. Charge-Carrier Mobilities in Metal Halide Perovskites: Fundamental Mechanisms and Limits, *ACS Energy Lett.* **2017**, *2*, 1539-1548.

(4) Xia, C. Q.; Peng, J.; Poncé, S.; Patel, J. B.; Wright, A. D.; Crothers, T. W.; Uller Rothmann, M.; Borchert, J.; Milot, R. L.; Kraus, H.; Lin, Q.; Giustino, F.; Herz, L. M.; Johnston, M. B. Limits to Electrical Mobility in Lead-Halide Perovskite Semiconductors, *J. Phys. Chem. Lett.* **2021**, *12*, 3607-3617.

(5) Le Corre, V. M.; Duijnstee, E. A.; El Tambouli, O.; Ball, J. M.; Snaith, H. J.; Lim, J.; Koster, L. J. A. Revealing Charge Carrier Mobility and Defect Densities in Metal Halide Perovskites via Space-Charge-Limited Current Measurements, *ACS Energy Lett.* **2021**, *6*, 1087-1094.

(6) Wang, Q.; Ito, S.; Grätzel, M.; Fabregat-Santiago, F.; Mora-Seró, I.; Bisquert, J.; Bessho, T.; Imai, H. Characteristics of high efficiency dye-sensitized solar cells, *J. Phys. Chem. B* **2006**, *110*, 19406-19411.

(7) Dloczik, L.; Ileperuma, O.; Lauerman, I.; Peter, L. M.; Ponomarev, E. A.; Redmond, G.; Shaw, N. J.; Uhlendorf, I. Dynamic Response of Dye-Sensitized Nanocrystalline Solar Cells: Characterization by Intensity-Modulated Photocurrent Spectroscopy, *J. Phys. Chem. B* **1997**, *101*, 10281-10289.

(8) Bisquert, J. Theory of the impedance of electron diffusion and recombination in a thin layer, *J. Phys. Chem. B* **2002**, *106*, 325-333.

(9) Bag, M.; Renna, L. A.; Adhikari, R. Y.; Karak, S.; Liu, F.; Lahti, P. M.; Russell, T. P.; Tuominen, M. T.; Venkataraman, D. Kinetics of Ion Transport in Perovskite Active Layers and Its Implications for Active Layer Stability, *J. Am. Chem. Soc.* **2015**, *137*, 13130-13137.

(10) Peng, W.; Aranda, C.; Bakr, O. M.; Garcia-Belmonte, G.; Bisquert, J.; Guerrero, A. Quantification of Ionic Diffusion in Lead Halide Perovskite Single Crystals, *ACS Energy Lett.* **2018**, *3*, 1477-1481.

(11) Pockett, A.; Eperon, G. E.; Peltola, T.; Snaith, H. J.; Walker, A. B.; Peter, L. M.; Cameron, P. J. Characterization of planar lead halide perovskite solar cells by impedance spectroscopy, open circuit photovoltage decay and intensity-modulated photovoltage/photocurrent spectroscopy, *J. Phys. Chem. C* **2015**, *119*, 3456–3465.

(12) Ravishankar, S.; Riquelme, A.; Sarkar, S. K.; Garcia-Batlle, M.; Garcia-Belmonte, G.; Bisquert, J. Intensity-Modulated Photocurrent Spectroscopy and Its Application to Perovskite Solar Cells, *The Journal of Physical Chemistry C* **2019**, *123*, 24995-25014.

(13) Ravishankar, S.; Aranda, C.; Boix, P. P.; Anta, J. A.; Bisquert, J.; Garcia-Belmonte, G. Effects of Frequency Dependence of the External Quantum Efficiency of Perovskite Solar Cells, *J. Phys. Chem. Lett.* **2018**, *9*, 3099-3104.

(14) Bernhardsgrütter, D.; Schmid, M. M. Modeling of Intensity-Modulated Photocurrent/Photovoltage Spectroscopy: Effect of Mobile Ions on the Dynamic Response of Perovskite Solar Cells, *J. Phys. Chem. C* **2019**, *123*, 30077-30087.

(15) Riquelme, A.; Bennett, L. J.; Courtier, N. E.; Wolf, M. J.; Contreras-Bernal, L.; Walker, A. B.; Richardson, G.; Anta, J. A. Identification of recombination losses and charge collection efficiency in a perovskite solar cell by comparing impedance response to a drift-diffusion model, *Nanoscale* **2020**, *12*, 17385-17398.

(16) Bou, A.; Pockett, A.; Raptis, D.; Watson, T.; Carnie, M. J.; Bisquert, J. Beyond Impedance Spectroscopy of Perovskite Solar Cells: Insights from the Spectral Correlation of the Electrooptical Frequency Techniques, *J. Phys. Chem. Lett.* **2020**, *11*, 8654-8659.

(17) Antuch, M.; Millet, P.; Iwase, A.; Kudo, A. The role of surface states during photocurrent switching: Intensity modulated photocurrent spectroscopy analysis of BiVO4 photoelectrodes, *Applied Catalysis B: Environmental* **2018**, *237*, 401-408.

(18) Rodríguez-Gutiérrez, I.; García-Rodríguez, R.; Rodríguez-Pérez, M.; Vega-Poot, A.; Rodríguez Gattorno, G.; Parkinson, B. A.; Oskam, G. Charge Transfer and Recombination Dynamics at Inkjet-Printed $CuBi_2O_4$ Electrodes for Photoelectrochemical Water Splitting, *J. Phys. Chem. C* **2018**, *122*, 27169-27179.

(19) Cardenas-Morcoso, D.; Bou, A.; Ravishankar, S.; García-Tecedor, M.; Gimenez, S.; Bisquert, J. Intensity-Modulated Photocurrent Spectroscopy for Solar Energy Conversion Devices: What Does a Negative Value Mean?, *ACS Energy Lett.* **2020**, *5*, 187-191.

(20) Vanmaekelbergh, D.; Iranzo Marín, F.; van de Lagemaat, J. Transport of photogenerated charge carriers through crystalline GaP networks investigated by intensity modulated photocurrent spectroscopy, *Berichte der Bunsengesellschaft fur Physical Chemie* **1996**, *100*, 616-626.

(21) Halme, J.; Miettunen, K.; Lund, P. Effect of Nonuniform Generation and Inefficient Collection of Electrons on the Dynamic Photocurrent and Photovoltage Response of Nanostructured Photoelectrodes, *J. Phys. Chem. C* **2008**, *112*, 20491-20504.

(22) Pockett, A.; Spence, M.; Thomas, S. K.; Raptis, D.; Watson, T.; Carnie, M. J. Beyond the First Quadrant: Origin of the High Frequency Intensity-Modulated Photocurrent/Photovoltage Spectroscopy Response of Perovskite Solar Cells, *Solar RRL* **2021**, *5*, 2100159.

(23) Tainter, G. D.; Hörantner, M. T.; Pazos-Outón, L. M.; Lamboll, R. D.; Āboliņš, H.; Leijtens, T.; Mahesh, S.; Friend, R. H.; Snaith, H. J.; Joyce, H. J.; Deschler, F. Long-Range Charge Extraction in Back-Contact Perovskite Architectures via Suppressed Recombination, *Joule* **2019**, *3*, 1301-1313.

(24) Jumabekov, A. N.; Della Gaspera, E.; Xu, Z. Q.; Chesman, A. S. R.; van Embden, J.; Bonke, S. A.; Bao, Q.; Vak, D.; Bach, U. Back-contacted hybrid organic–inorganic perovskite solar cells, *J. Mat. Chem. C* **2016**, *4*, 3125-3130.

(25) Hou, Q.; Bacal, D.; Jumabekov, A. N.; Li, W.; Wang, Z.; Lin, X.; Ng, S. H.; Tan, B.; Bao, Q.; Chesman, A. S. R.; Cheng, Y.-B.; Bach, U. Back-contact perovskite solar cells with honeycomb-like charge collecting electrodes, *Nano Energy* **2018**, *50*, 710-716.

(26) Jumabekov, A. N. Chemical passivation of the perovskite layer and its real-time effect on the device performance in back-contact perovskite solar cells, *Journal of Vacuum Science & Technology A* **2020**, *38*, 060401.

(27) DeLuca, G.; Jumabekov, A. N.; Hu, Y.; Simonov, A. N.; Lu, J.; Tan, B.; Adhyaksa, G. W. P.; Garnett, E. C.; Reichmanis, E.; Chesman, A. S. R.; Bach, U. Transparent Quasi-Interdigitated Electrodes for Semitransparent Perovskite Back-Contact Solar Cells, *ACS Applied Energy Materials* **2018**, *1*, 4473-4478.

(28) Hu, Y.; Adhyaksa, G. W. P.; DeLuca, G.; Simonov, A. N.; Duffy, N. W.; Reichmanis, E.; Bach, U.; Docampo, P.; Bein, T.; Garnett, E. C.; Chesman, A. S. R.; Jumabekov, A. N. Perovskite solar cells with a hybrid electrode structure, *AIP Advances* **2019**, *9*, 125037.

(29) Prince, K. J.; Nardone, M.; Dunfield, S. P.; Teeter, G.; Mirzokarimov, M.; Warren, E. L.; Moore, D. T.; Berry, J. J.; Wolden, C. A.; Wheeler, L. M. Complementary interface formation toward high-efficiency all-back-contact perovskite solar cells, *Cell Reports Physical Science* **2021**, *2*, 100363.

(30) Lin, X.; Lu, J.; Raga, S. R.; McMeekin, D. P.; Ou, Q.; Scully, A. D.; Tan, B.; Chesman, A. S. R.; Deng, S.; Zhao, B.; Cheng, Y.-B.; Bach, U. Balancing Charge Extraction for Efficient Back-Contact Perovskite Solar Cells by Using an Embedded Mesoscopic Architecture, *Adv. Energy Mater.* **2021**, 2100053.

(31) Yang, S. J.; Kim, M.; Ko, H.; Sin, D. H.; Sung, J. H.; Mun, J.; Rho, J.; Jo, M.-H.; Cho, K. Visualization and Investigation of Charge Transport in Mixed-Halide Perovskite via Lateral-Structured Photovoltaic Devices, *Adv. Func. Mater.* **2018**, *28*, 1804067.

(32) Liu, S.; Wang, L.; Lin, W.-C.; Sucharitakul, S.; Burda, C.; Gao, X. P. A. Imaging the Long Transport Lengths of Photo-generated Carriers in Oriented Perovskite Films, *Nano Letters* **2016**, *16*, 7925-7929.

(33) Snaider, J. M.; Guo, Z.; Wang, T.; Yang, M.; Yuan, L.; Zhu, K.; Huang, L. Ultrafast Imaging of Carrier Transport across Grain Boundaries in Hybrid Perovskite Thin Films, *ACS Energy Lett.* **2018**, *3*, 1402-1408.

(34) Sun, S.; Salim, T.; Mathews, N.; Duchamp, M.; Boothroyd, C.; Xing, G.; Sum, T. C.; Lam, Y. M. The origin of high efficiency in low-temperature solution-processable bilayer organometal halide hybrid solar cells, *Energy & Environmental Science* **2014**, *7*, 399-407.

(35) Lamboll, R. D.; Greenham, N. C. Reduced dimensionality in drift-diffusion models of back-contact solar cells and scanning photocurrent microscopy, *Journal of Applied Physics* **2017**, *122*, 133106.

(36) Guerrero, A.; Garcia-Belmonte, G.; Mora-Sero, I.; Bisquert, J.; Kang, Y. S.; Jacobsson, T. J.; Correa-Baena, J.-P.; Hagfeldt, A. Properties of Contact and Bulk Impedances in Hybrid Lead Halide Perovskite Solar Cells Including Inductive Loop Elements, *J. Phys. Chem. C* **2016**, *120*, 8023-8032.

Supporting Information

Extracting *In-Situ* Charge Carrier Diffusion Parameters in Perovskite Solar Cells with Light Modulated Techniques

Agustín Bou[a], Haralds Āboliņš,[b] Arjun Ashoka,[b] Héctor Cruanyes,[a] Antonio Guerrero,[a] Felix Deschler, [c]* Juan Bisquert [a]*

[a]Institute of Advanced Materials (INAM), Universitat Jaume I, Avda. Sos Baynat sn, 12006 Castelló, Spain

[b]Cavendish Laboratory, University of Cambridge, J.J. Thomson Avenue, CB3 0HE, Cambridge, United Kingdom

[c]Walter-Schottky-Institute, Physics Department, Technical University Munich, Am Coulombwall 4, Garching bei München, Germany

IMPS Function for sandwich solar cell configuration (Fig. 2a)

Carrier generation in the right side of the cell with an exponential profile has the expression

$$\tilde{G}(x,t) = \alpha\tilde{\Phi}(t)\exp\left(\alpha(x-d)\right) \tag{A1}$$

where $\tilde{\Phi}(t) = \tilde{\Phi}_0 \exp(i\omega t)$ is the small ac perturbation of the incident photon flux. The excess electron density has the form

$$\tilde{n}(x,t) = u(x,\omega)\exp(i\omega t) \tag{A2}$$

Equation 1 is reduced to the following expression

$$\frac{\partial^2 u}{\partial u^2} = \frac{z(\omega)^2}{L_n^2}u - \alpha\frac{\tilde{\Phi}_0}{D_n}\exp\left(\alpha(x-d)\right) \tag{A3}$$

with $z(\omega) = (1+i\omega\tau_n)^{1/2}$. The solution is

$$u(x,\omega) = A\exp\left(z\frac{x}{L_n}\right) + B\exp\left(-z\frac{x}{L_n}\right) + C\exp(+\alpha x) \tag{A4}$$

as it has been previously shown in literature.[1] A, B and C are constants that can be calculated with the use of the boundary conditions:

$$A + B = -C \tag{A5}$$

$$A\exp\left(z\frac{d}{L_n}\right) - B\exp\left(-z\frac{d}{L_n}\right) = -C\frac{\alpha L_n}{z}\exp(\alpha d) \tag{A6}$$

Therefore

$$A = -C\frac{z\exp\left(-z\frac{d}{L_n}\right)+\alpha L_n\exp(\alpha d)}{z\left[\exp\left(z\frac{d}{L_n}\right)+\exp\left(-z\frac{d}{L_n}\right)\right]} \tag{A7}$$

$$B = C\frac{-z\exp\left(z\frac{d}{L_n}\right)+\alpha L_n\exp(\alpha d)}{z\left[\exp\left(z\frac{d}{L_n}\right)+\exp\left(-z\frac{d}{L_n}\right)\right]} \tag{A8}$$

The C constant is obtained introducing the solution into the differential equation.

$$C = \frac{\alpha L_n^2(\tilde{\Phi}_0/D_n)}{z^2-\alpha^2L_n^2}\exp(-\alpha d) \tag{A9}$$

The IMPS transfer function is obtained with

$$\tilde{j}_e(x=0) = +qD_n\frac{\partial u}{\partial x} \tag{3}$$

$$Q = \frac{\tilde{j}_e}{q\tilde{\Phi}} \tag{4}$$

The excess electron density can be obtained by taking real part of the Equation A4.

IMPS Function for lateral transport configuration (Fig. 2b)

Similarly to the problem of the parallel contacts, we use Equation 1 for holes, with carrier generation in this case defined by:

$$\tilde{G}(x) = \begin{cases} 0 & 0 < x \leq d \\ \beta\tilde{\Phi} & d < x < d+\delta \\ 0 & d+\delta \leq x < +\infty \end{cases} \tag{A10}$$

Then, we have three separated regions (1, 2, 3 from right to left). To calculate the IMPS transfer function, we need to know the extracted current at the collecting point $x = 0$,

$$\tilde{j}_p(0) = qD_p\left.\frac{\partial\tilde{p}}{\partial x}\right|_{x=0} \tag{A11}$$

The small perturbation transform of equation 1 for regions 1 and 3 gives

$$s\tilde{p} = D_p\frac{\partial^2\tilde{p}}{\partial x^2} - \frac{\tilde{p}}{\tau_p} \tag{A12}$$

The solution for excess density of holes in region 1 is:

$$\tilde{p}(x) = Me^{x/L} + Ne^{-x/L} \tag{A13}$$

Given that the boundary condition at the collecting contact is $p(0) = 0$, this gives $N = -M$, and therefore

$$\tilde{p}(x) = M(e^{x/L} - e^{-x/L}) \tag{A14}$$

Substituting the value of $\tilde{p}(x)$ in equation A14 we get

$$L = \frac{L_p}{\sqrt{1+s\tau_p}} = \frac{L_p}{z} \tag{A15}$$

Similarly, the solution for excess density of holes in region 3 is:

$$\tilde{p}(x) = Re^{x/L} + Se^{-x/L} \tag{A16}$$

Here, as a boundary condition, we apply $\tilde{p}(+\infty) = 0$, which gives $R = 0$, and the excess hole density is

$$\tilde{p}(x) = Se^{-x/L} \tag{A17}$$

Assuming uniform density at the generation spot, $\tilde{p}(d) = \tilde{p}(d + \delta)$, we get

$$S = \left(e^{d/L} - e^{-d/L}\right) e^{\frac{d+\delta}{L}} M \tag{A18}$$

And solving small perturbation transform of equation 1 in the illuminated region 2, we get:

$$M = \frac{\beta\delta}{2\left(s\delta \sinh\left(\frac{dz}{L_p}\right) + \frac{1}{\beta\delta} e^{\frac{dz}{L_p}}\right)} \tilde{\Phi} \tag{A19}$$

Which gives the extracted current:

$$\tilde{j}_p(0) = qD_p \frac{\partial\tilde{p}}{\partial x}\bigg|_{x=0} = 2q \frac{zD_p}{L_p} M = \frac{zD_p}{L_p} \frac{\beta\delta}{s\delta \sinh\left(\frac{dz}{L_p}\right) + \frac{1}{\beta\delta} e^{\frac{dz}{L_p}}} q\tilde{\Phi} \tag{A20}$$

In this case, the definition of the IMPS transfer function Q will be slightly different from Equation 4, since the illuminated and collecting areas are not the same. Therefore, we will define it as:

$$Q = \frac{a}{\delta} \frac{\tilde{j}_e}{q\tilde{\Phi}} = k \frac{\tilde{j}_e}{q\tilde{\Phi}} \tag{A21}$$

Where a and δ are the collecting and illumination transversal length, respectively. Since k is an experimental factor that depends on the configuration, we calculate the IMPS transfer function for $k = 1$ in equation (16). In practice a normalizing factor in Q can be used as a fitting parameter, since obtaining the EQE is not a priority in this configuration.

Fitting the IMPS Function for sandwich solar cell configuration (Fig 2a)

The RC attenuation $A(\omega)$ describes that the diffusion is accompanied by a larger equivalent circuit.

$$Q_{meas}(\omega) = A(\omega)Q(\omega) \tag{15}$$

For the sandwich solar cell configuration, the series resistance and the geometrical capacitance can be measured via Impedance Spectroscopy. The absorbance length is obtained from bibliographic sources.[2] The list of fitting parameters, used for the elaboration of Fig. (5), is indicated in Table S1.

Table S1. Parameters used in IMPS fitting function in Fig. (5) for sandwich solar cell configuration.

Light	α^{-1} (nm)	d (µm)	R_S (Ω cm^2)	C_g (nF/cm^2)
Blue	40	5.3	10	3.6
Red	140			

Fitting the IMPS Function for lateral transport configuration (Fig. 2b)

In addition to attenuation, two more fitting parameters had to be introduced. Firstly, since the photocurrent amplitude for IMPS in the lateral transport configuration was measured in arbitrary units, a normalization factor N had to be introduced such that

$$Q_{meas}(\omega) = N \times A(\omega)\, Q(\omega). \tag{A21}$$

Secondly, in order to account for possible anomalous diffusions effects[3] a power law in frequency is introduced such that

$$Q_{meas}(i\omega) = Q_{meas}[(i\omega)^p]. \tag{A22}$$

The full list of fitting parameters extracted of Fig. 8 can be found in Table S2 below.

Table S2. Parameters extracted in IMPS fitting function in Fig. (8) for the lateral transport configuration.

N	p	R_S (Ω cm^2)	R_3 (Ω cm^2)	C_g (μF/cm^2)	L_p (µm)	D_p (cm^2/s)
3.4×10^5	1.26	19	3.8	1.1	11	0.76

Spectral Shapes of the Limiting Functions

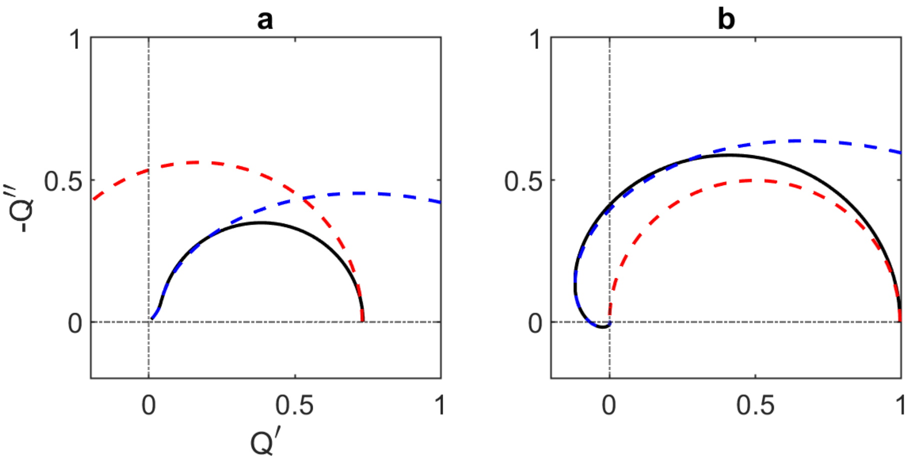

Figure SI.1. Complex plane plots of the IMPS transfer function (black line) for $L_n = 10d$ and different absorption lengths (a) $\alpha d = 4/3$ and (b) $\alpha d = 10$. The limiting functions are represented in the high frequency limit (blue dashed line) and in the low frequency limit (red dashed line). No *RC* attenuation is considered.

To better appreciate the analytical shape of the function of interest we present some approximations that can be obtained when the diffusion length is longer that the cell thickness ($L_n < d$) and the light is completely absorbed in a short region. The high frequency limit is

$$Q(\omega) \approx 2\,\frac{\exp\left(-\frac{d}{L_n}\sqrt{i\omega\tau_n}\right)-\frac{1}{2}\exp(-\alpha d)\left(1+\frac{1}{L_n\alpha}\sqrt{i\omega\tau_n}\right)}{\left(1-i\omega\tau\frac{1}{L_n^2\alpha^2}\right)} \tag{A26}$$

It represents a positive arc as it is shown in Figure SI.1a. The low frequency limit is

$$Q(\omega) \approx 2\,\frac{1-\exp(-\alpha d)\left(1+\frac{d}{\alpha L_n^2}(1+i\omega\tau_n)\right)}{\left(2+\frac{d^2}{L_n^2}-\frac{d^2}{L_n^4\alpha^2}\right)+i\omega\tau\left(\frac{d^2}{L_n^2}+\frac{2d^2}{L_n^4\alpha^2}\right)} \tag{A27}$$

This function forms a semicircle that starts in the negative axis. As the absorption length becomes shorter, $\alpha d \gg 1$ the terms with the negative exponential become irrelevant. The limiting functions for high and low frequency turn into the following expressions, respectively:

$$Q(\omega) \approx \frac{2}{\left(1-i\omega\tau_n\frac{1}{L_n^2\alpha^2}\right)}\exp\left(-\frac{d}{L_n}\sqrt{i\omega\tau_n}\right) \tag{A28}$$

$$Q(\omega) \approx \frac{2}{\left(2+\frac{d^2}{L_n^2}-\frac{d^2}{L_n^4\alpha^2}\right)+i\omega\tau_n\left(\frac{d^2}{L_n^2}+\frac{2d^2}{L_n^4\alpha^2}\right)} \tag{A29}$$

The spectral dependences of these functions are shown in Figure SI.1b. The complex exponential function that depends on $\sqrt{i\omega\tau_n}$ is the one that loops and spirals into the negative Q' axis.

The RC attenuation effect

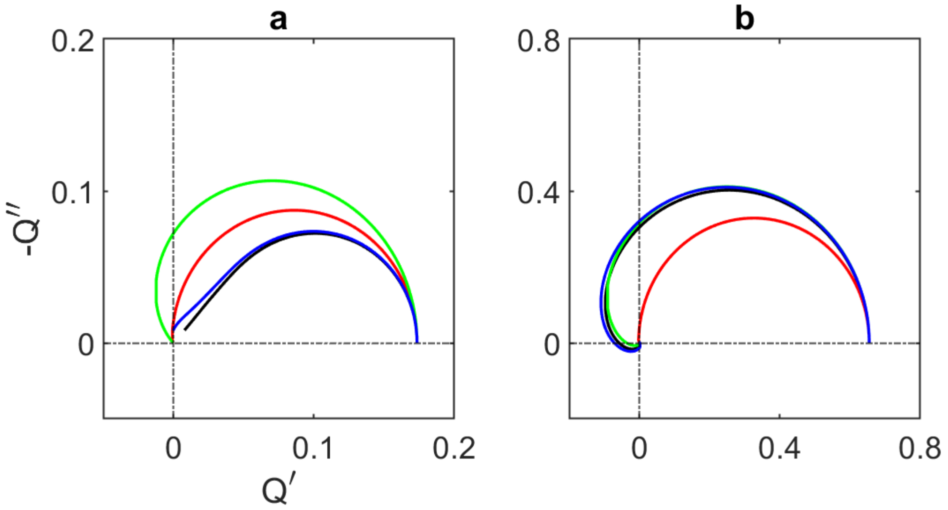

Figure SI.2. Complex plane plots of the simulated IMPS transfer function considering RC attenuation in different absorption and diffusion lengths (Eq.12,13). The black line is the theoretical IMPS transfer function ($RC = 0$), the red line is for a high RC factor ($RC = 10^2\tau_n$), the green line is for an intermediate value ($RC = \tau_n$) and the blue line represents the low limit value ($RC = 10^{-2}\tau_n$). (a) Cell distance $d = 10^{-6}$μm, diffusion coefficient of $D = 0.001\ \mathrm{cm}^2/\mathrm{s}$, absorption length of $\alpha d = 4/3$ and recombination lifetime $\tau_n = 1$ μs. (b) absorption length of $\alpha d = 10$ and lifetime 10 μs.

Measured IMPS Function for all the whole measured frequency range

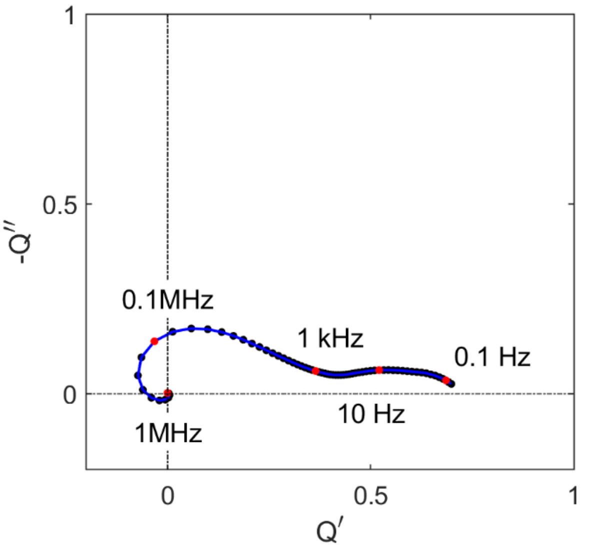

Figure SI.3. Complex plane plot of the measured IMPS transfer function as fitted in Fig. 5 for blue light. Measurements are shown for a wider frequency range down to 0.1 Hz. Red points denote specific frequencies as written.

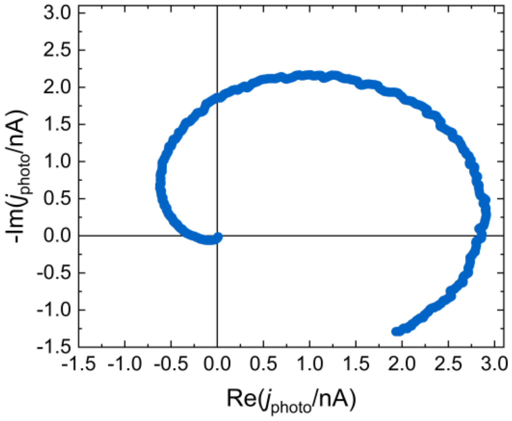

Figure SI.4. Complex plane plot of the measured IMPS transfer function as fitted in Fig. 8. Measurements are shown for a wider frequency range down to 5 Hz.

Methods

Interdigitated back contact solar cell fabrication

ITO was deposited by sputter coating 150 nm on SiO2 (10 µm thick) on Si chips. SnO_2 was deposited by diluting a colloidal dispersion (15% in H_2O, purchased form Alfa Aesar) to 2% and spincoating for 30 s at 3000 rpm and baking on a hot plate at 150 °C for 30 min. An insulating layer of AlO_x (150nm) was deposited by atomic layer deposition on the chips. The quasi-interdigitated electrode pattern was written using e-beam lithography. After development, Cr/Au (2/70 nm) was deposited by thermal evaporation followed by lift-off. The chips were then placed in the TMAH-based AZ726 MIF developer, which etched the AlO_x not covered by the electrodes, leaving the Au electrodes electrically insulated whilst exposing the SnO_2

The organic cations (FAI and MABr) were purchased from GreatCell solar, the lead compounds (PbI_2 and $PbBr_2$) were purchased from TCI and the CsI was purchased from Sigma Aldrich. The mixed cation perovskite solution was prepared by mixing FAI (1 M), MABr (0.2 M), PbI_2 (1.1 M) and $PbBr_2$ (0.2 M) in anhydrous DMF:DMSO 4:1 (v:v). After that, 5% of 1.5 M CsI was added to the prepared mixed cation perovskite solution to achieve triple cation perovskite solution. Before depositing perovskite the patterned electrode substrate was cleaned with UV-ozone treatment for 15 min. The film perovskite was spin-coated with a two-step program at 1000 and 6000 rpm for 10s and 20s respectively. During the second step, 100 µl of antisolvent anhydrous chlorobenzene was dropped on the substrate, 5 second before the end of program. After spin-coating, the substrate was annealed on a hotplate at 100 °C for 1h. The spin-coating and annealing steps were performed in a N2-filled glovebox.

IMPS measurement in lateral transport configuration

A HP 8116A 50 MHz programmable function generator was used to generate two synchronous signals - one with a 50% duty cycle which allowed for comfortable reference signal phase locking with the lock-in amplifier and a second TTL signal with an on-time of < 40ns and with voltage limits set to appropriately trigger the laser system. The laser system used was a Pico Quant picosecond pulsed diode laser driver PDL 800-D with a LDH405 pulsed laser diode head (405 nm excitation wavelength, pulse length of 20ps) to appropriately excite above the bandgap of perovskite being studied. A Zurich Instruments HF2LI 50 MHz Lock-in Amplifier was used for the lock-in amplification of the current signal from the device and the HF2 LabOne software was used for frequency, lock-in signal and phase acquisition. The stage on which the sample was placed, and the confocal microscope was part of a WITec alpha 300 s setup. The incident power over the range of repetition rates studied was between 7nW and 5uW and the photocurrent extracted had an expected linear dependence of the average power on frequency. The maximum fluence studied (at 2MHz) by the air objective focused 1.5um laser spot was about 300 W/cm^2. The excitation frequency was swept between 20 kHz to 500 kHz.

References

1. Dloczik, L.; Ileperuma, O.; Lauerman, I.; Peter, L. M.; Ponomarev, E. A.; Redmond, G.; Shaw, N. J.; Uhlendorf, I., Dynamic Response of Dye-Sensitized Nanocrystalline Solar Cells: Characterization by Intensity-Modulated Photocurrent Spectroscopy. *The Journal of Physical Chemistry B* **1997**, *101*, 10281-10289.
2. Sun, S.; Salim, T.; Mathews, N.; Duchamp, M.; Boothroyd, C.; Xing, G.; Sum, T. C.; Lam, Y. M., The Origin of High Efficiency in Low-Temperature Solution-Processable Bilayer Organometal Halide Hybrid Solar Cells. *Energy & Environmental Science* **2014**, *7*, 399-407.
3. Bisquert, J.; Compte, A., Theory of the Electrochemical Impedance of Anomalous Diffusion. *Journal of Electroanalytical Chemistry* **2001**, *499*, 112-120.

Chapter 4

Publication 3

Limited information of impedance spectroscopy about electronic diffusion transport: The case of perovskite solar cells

Bou, A.; Pockett, A.; Cruanyes, H.; Raptis, D.; Watson, T.; Carnie, M. J.; Bisquert, J. Limited information of impedance spectroscopy about electronic diffusion transport: The case of perovskite solar cells, *APL Materials*, **2022**, *10*, 051104.

Candidate's Contribution

Nature of Contribution	Extent of Contribution
• Measured all the experimental data • Performed the simulations • Did the conceptualization of the work • Wrote the first manuscript and build the figures • Answered the referees' questions	90%

Introduction

This work models the IS, IMPS and IMVS responses of perovskite solar cells. It demonstrates that, in the case of non-uniform generation profiles, the trace of electron diffusion can be visible in light-modulated techniques, while hidden in voltage modulation techniques. The models are supported by experimental data, which fulfil the relation between the three techniques.

Published Manuscript

Limited Information of Impedance Spectroscopy about Electronic Diffusion Transport: The Case of Perovskite Solar Cells

Agustín Bou,[1*] Adam Pockett,[2] Héctor Cruanyes,[1] Dimitrios Raptis,[2] Trystan Watson,[2] Matthew J. Carnie[2] and Juan Bisquert[1*]

[1] Institute of Advanced Materials (INAM), Universitat Jaume I, 12006 Castelló, Spain

[2] SPECIFIC, Materials Research Center, College of Engineering, Swansea University, Swansea SA1 8EN, United Kingdom

Corresponding authors: Agustín Bou acatala@uji.es and Juan Bisquert bisquert@uji.es

Abstract

Impedance Spectroscopy (IS) has proven to be a powerful tool for the extraction of significant electronic parameters in a wide variety of electrochemical systems, such as solar cells or electrochemical cells. However, this has not been the case of perovskite solar cells which have the particular ionic-electronic combined transport that complicates the interpretation of experimental results due to an overlapping of different phenomena with similar characteristic frequencies. Therefore, the diffusion of electrons is indistinguishable on IS and there appears the need to use other small perturbation experimental techniques. Here we show that voltage-modulated measurements do not provide the same information as light-modulated techniques. We investigate the responses of perovskite solar cells to IS and Intensity Modulated Photocurrent and Photovoltage Spectroscopies (IMPS and IMVS). We find that the perturbations by light instead of voltage can uncover the electronic transport from other phenomena, resulting in a loop in the high-frequency region of the complex planes of the IMPS and IMVS spectra. The calculated responses are endorsed by experimental data that reproduce the expected high frequency loops. We finally discuss the requirement to use a combination of small perturbation techniques for a successful estimation of diffusion parameters of perovskite solar cells.

Impedance Spectroscopy (IS) has been a valuable technique for the analysis of the electrical response of a wide variety of semiconductor devices,[1-5] and specifically solar cells.[6-7] In fact, IS has led to the determination of carrier diffusion and recombination, charge transfer coefficient and carrier lifetimes in silicon solar cells,[8] dye sensitized solar cells[9-10] and organic solar cells.[6, 11] This important technique has also been widely used for the characterization of Perovskite Solar Cells (PSC).[12-14] Although the IS characteristics of PSC display a rich diversity of features,[15] the interpretation of such spectra is not straightforward and the extraction of important parameters, such as the electronic carrier diffusion, has not been achieved.

One of the reasons for the complex interpretation of IS data on PSC is the influence of ionic motion inside the perovskite layer. The mobile ions can cause interface polarization,[16] affecting the charge transfer rates or inducing capacitive accumulation of electronic carriers. These phenomena affect the IS spectra hindering the electronic information that is coupled with ionic phenomena and preventing the extraction of electronic information. However, the combination of IS and other small perturbation techniques has demonstrated to be effective in the understanding of PSCs.[17-19] Recently it was shown that electron diffusion parameters can be extracted from Intensity-Modulated Photocurrent Spectroscopy (IMPS).[20] However, this is not possible with voltage-modulated techniques such as IS.

Here we want to explain why voltage-modulated measurements do not have the same information as light-modulated techniques. For that purpose, we calculate the response of charge carrier diffusion for one voltage-modulated technique, the IS, and two light-modulated techniques, the IMPS and the Intensity-Modulated photo-Voltage Spectroscopy (IMVS). From these results, we conclude that while in IS both the perturbation and the response take place at the same contact, in IMPS and IMVS it is possible to apply the perturbation far from the collecting contact of one of the charge carriers, disclosing the diffusion of these particles along the film.

Following the methods that have been used for the calculation of the transfer functions of IS, IMPS and IMVS,[20-23] we solve the conservation equation in the frequency domain. The equation for carrier density $n(x,t)$ including recombination and Beer-Lambert generation is as follows

$$\frac{\partial n}{\partial t} = D_n \frac{\partial^2 n}{\partial x^2} - \frac{n - n_0}{\tau_n} + \alpha \Phi(t) e^{\alpha(x-d)} \tag{1}$$

where D_n is the diffusion coefficient, n_0 is the equilibrium density under dark conditions, τ_n is the recombination lifetime, d is the active layer thickness, and α is the light absorption coefficient.

Since the solution has been already derived in the above references, we skip the calculation details and directly show the solutions for the three techniques, in order to focus on the relationship between the solutions that provides new physical insight. We follow the notation used in ref [22], where the transfer functions have been expressed in terms of three characteristic frequency parameters that determine all possible spectral shapes. The solution of Eq. (1) in the frequency domain for the IS is

$$Z(\omega) = R_d \left(\frac{\omega_d}{p}\right)^{1/2} coth\left(\left(\frac{p}{\omega_d}\right)^{1/2}\right) \tag{2}$$

where R_d is the diffusion resistance, p is defined as

$$p = i\omega + \omega_{rec} \tag{3}$$

and the two characteristics frequencies are defined as

$$\omega_d = \frac{D_n}{d^2} \tag{4}$$

$$\omega_{rec} = {\tau_n}^{-1} \tag{5}$$

The solution of Eq. (1) in the frequency domain for the IMPS is

$$Q(\omega) = \frac{F(\omega)}{\cosh\left[\left(\frac{p}{\omega_d}\right)^{1/2}\right]} \tag{6}$$

and for IMVS it is

$$W(\omega) = R_d \frac{F(\omega)}{\left(\frac{p}{\omega_d}\right)^{1/2} \sinh\left[\left(\frac{p}{\omega_d}\right)^{1/2}\right]} \tag{7}$$

The transfer functions of IMPS and IMVS have a common factor $F(\omega)$ and is defined as

$$F(\omega) = \frac{1 - e^{-\alpha d}\left\{e^{(p/\omega_d)^{1/2}} + \left[\left(\frac{p}{\omega_\alpha}\right)^{1/2} - 1\right]\sinh\left[\left(\frac{p}{\omega_d}\right)^{1/2}\right]\right\}}{\left[1 - \frac{p}{\omega_\alpha}\right]} \tag{8}$$

The absorption coefficient α occurs in Eq. (8) and enables to define the third frequency ω_α, as

$$\omega_\alpha = D_n \alpha^2 \tag{9}$$

The extraction of diffusion parameters from the IS is done via the high frequency part of the spectra. There appears a 45º line and a turnover followed by an impedance arc that allows to extract the diffusion resistance R_d,[23] and the diffusion frequency ω_d.[24] This method was widely exploited to obtain the electron diffusion coefficient and electron recombination lifetime in dye-sensitized solar cells.[25-27]

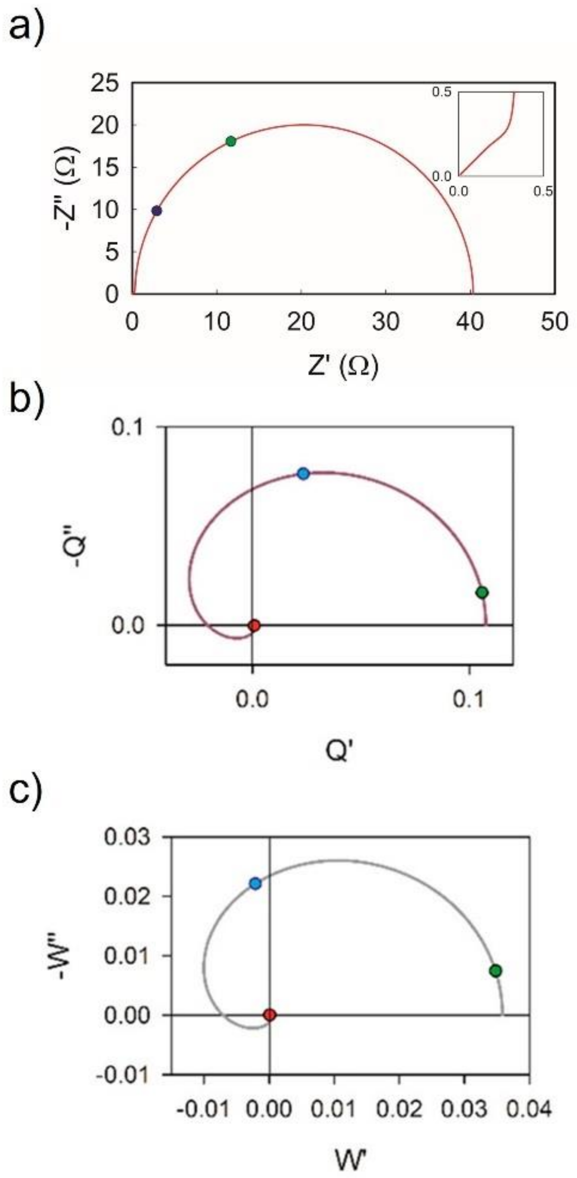

Figure 1. (a) IS, (b) IMPS and (c) IMVS spectra for typical values of a carbon-based perovskite solar cell. The values of the parameters are $R_d = 1\Omega$, $\omega_d = 1.2 \times 10^5\ \mathrm{s}^{-1}$ (green), $\omega_\alpha = 1 \times 10^5\ \mathrm{s}^{-1}$ (red), and $\omega_{rec} = 5 \times 10^4\ \mathrm{s}^{-1}$ (blue). The inset in (a) shows the IS spectrum at high frequency.

Here we calculate in Fig. 1 the different spectra with the characteristics of carbon-based perovskite solar cells.[19] In Figure 1a we see that the 45° line of Eq. (2) indicating the transport resistance appears at very high frequency but with very small values, due to the high diffusion coefficient of PSC.[28-29] Hence, it has not been possible to distinguish conclusively electron diffusion from other phenomena via the impedance spectra in perovskite solar cells.

However, if we look at the common factor $F(\omega)$ of IMPS and IMVS, the diffusion frequency ω_d appears coupled with ω_α. This opens a door to an alternative pathway to the extraction of diffusion and recombination parameters via light-modulated techniques. In Figure 1b and 1c we calculate the IMPS and IMVS spectra for the typical frequency values of carbon-based perovskite solar cells.[19] The coupling of both ω_d and ω_α results in a looping spiral at high frequency crossing the real and/or imaginary axes and going through several quadrants, as shown previously in refs. [20] and [22].

Following these results, we aim to prove these theoretical predictions by the measurement of the three distinct frequency domain small perturbation methods of PSC. However, we note that the appearance of the looping spectra in IMPS and IMVS spectra is not a guaranteed result, and neither is the coupling between the frequencies ω_d and ω_α. It has been demonstrated that the loop at high frequency depends on the relation between these frequencies.[22] This means, experimentally, that the generation inside the perovskite film needs to be non-uniform, i.e., the absorber has to be longer than the absorption length.[20] Therefore, we have chosen carbon-based perovskite solar cells with perovskite film thicknesses above 1 µm and a blue light illumination source which has a short absorption length.[30]

We have measured IS, IMPS and IMVS at open circuit conditions for a variety of light intensities. The region of interest inside the spectra is in the high frequency region. Therefore, we have used a Zahner system for the IS that allows up to 10 MHz bias perturbation. However, the results at such high frequencies using standard set-ups have been proven to be obscured by instrument limitations. Therefore, we have chosen a previously used technique capable of solving these problems and obtaining satisfactory results.[31] To facilitate the correct measurement at high frequencies, our experimental system uses a current amplifier that introduces a series resistances of 50 Ω to the extracted current in the IMPS measurements.

We have obtained the expected results for the entirety of the different conditions used, i.e., IS spectra that remain in the positive real part of the complex plane, while the IMPS and IMVS stable responses looped at high frequency crossing the imaginary axis. To illustrate this, we have put together three representative spectra in Figure 2. The rest of the measured spectra can be found in the SI.

We see in Figure 2a that the IS spectrum draws only a positive real arc where the Warburg element shown in the inset in Figure 1a cannot be distinguished. This can be caused by the interference of other equivalent circuit elements that are orders of magnitude larger than the diffusion resistance.[12, 15] Contrarily, both the IMPS and IMVS spectra cross the second quadrant in Figures 2b and 2c, respectively, clearly showing the effects of diffusion. For the sake of clarity, we show the three spectra in a normalized complex plane plot, Fig. 2c, where the shape of the different techniques can be clearly distinguished.

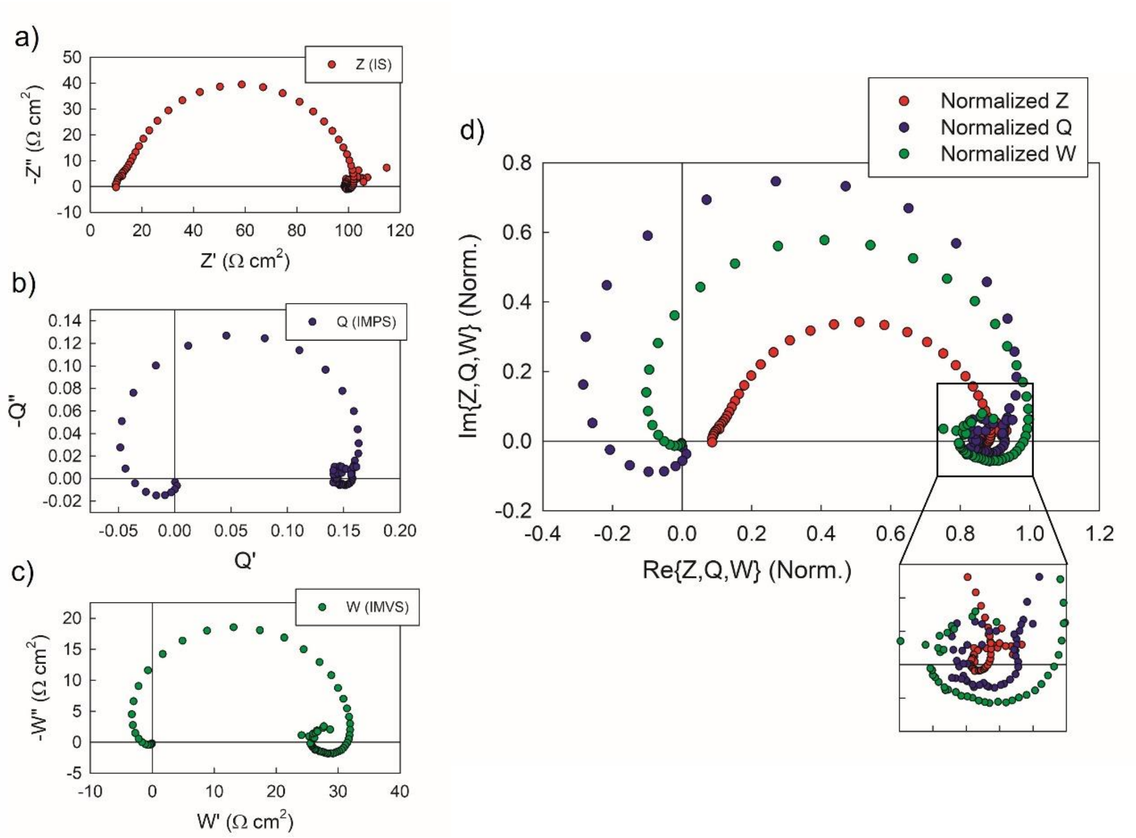

Figure 2. Experimental complex plane plots of the (a) IS, (b) IMPS and (c) IMVS for a carbon-based perovskite solar cell. (d) shows the three normalized spectra together.

In the combined plot of Figure 2d, we see there is a relation in the responses of the three techniques, both in the number of features and in the spectral shape. Previous works have already explained the relation of the three techniques.[19, 32-33] The relation between IMPS and IMVS transfer functions must give the IS transfer function as follows

$$Z(\omega) = \frac{W(\omega)}{Q(\omega)} \tag{10}$$

However, none of the previous has treated spiral IMPS and IMVS spectra due to ω_d and ω_α coupling. From the expressions of Eqs. (6) and (7), the factor $F(\omega)$, which is the cause of the looping spectra, is cancelled by the division, and the IS transfer function is free of this factor. This is a demanding experimental test since the spiraling of the light-modulated spectra of IMPS and IMVS must disappear in the division of Eq. (10). We must show experimentally that the $F(\omega)$ factor is cancelled.

As mentioned earlier, the experimental set-ups for IMPS and IMVS is different from the one we have used for IS. Therefore, the quotient must be corrected by displacing the points in the complex plane point 50 Ω leftwards in the real axis. For further checking that this method is correct, we have introduced additional series resistances to the system, proving that the effect of the series resistance in the quotient between $W(\omega)$ and $Q(\omega)$

produces a displacement to the right. This is clearly seen in Figure 3a, where the subsequent addition of a series resistances moves the experimental points of W/Q to the right side of the complex plane. The corrected spectra in Figure 3b show that the experimental quotient (color points) gives a similar response to the experimental IS measured directly (black points). In fact, the looping into the second quadrant gets cancelled, therefore proving that the factor $F(\omega)$ including the ω_α does not appear neither in the IS response nor in the quotient. We note that the resulting quotient crosses the real axis into the fourth quadrant at high frequency, which we think is likewise caused by the experiment.

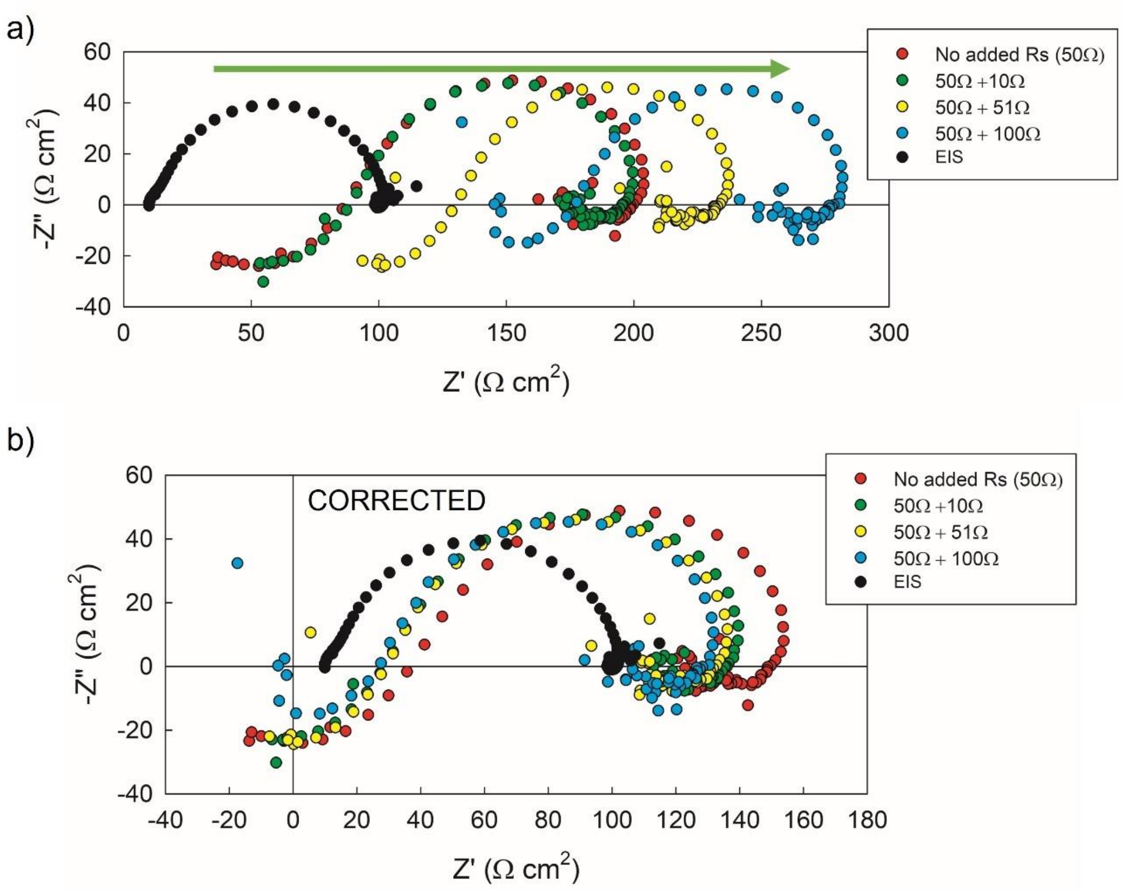

Figure 3. Experimental complex plane plots of the directly measured IS (black points) and the experimental quotient of IMPS and IMVS given by Eq. (10) (coloured points). The IMPS and IMVS measurements include a series resistance of 50 Ω from the experimental set-up plus added resistances as indicated in the legend. (a) shows the quotients as it is while (b) shows the corrected spectra by moving leftwards the corresponding series resistance value.

Figure 3 confirms that the attainment of diffusion parameters cannot be achieved only by IS, since it is hidden by other phenomena. Therefore, it is convenient to use a combination of techniques, which will allow a further extraction of operation parameters. IS is still an important technique, since the series resistance and bulk capacitance obtained at high frequency affect the IMPS response.[20] Hence, a full analysis of perovskite devices requires the utilization of more than one frequency technique with both light and voltage perturbations. In fact, the addition of time-dependent techniques with similar perturbations could bring light on the high frequency response of IMPS and IMVS.[34-36]

In conclusion, although the experimental extraction of diffusion parameters via IS has been achieved in other kind of devices, such as dye-sensitized solar cells, it is not normally possible in perovskite solar cells, due to the infimum feature that it leaves in the IS spectra. However, the obtention of diffusion parameters can be achieved via light-modulated techniques due to the larger spectral trace that is due to the coupling of diffusion and absorption parameters in the high frequency part of the experimental IMPS and IMVS spectra.

Supporting Information:

The Supporting Information includes the experimental details regarding both device fabrication and characterization methods, and additional IS, IMPS and IMVS spectra at different illumination conditions.

Acknowledgments

We thank Generalitat Valenciana for the project PROMETEO/2020/028. A.B. and H.C. acknowledge FPI studentships funding from Ministerio de Ciencia e Innovación of Spain (BES-2017- 080351 and PRE2020-095374),

References

1. Lasia, A., Electrochemical Impedance Spectroscopy and Its Applications; Springer, 2014.

2. Orazem, M. E.; Tribollet, B., Electrochemical Impedance Spectroscopy, Second Edition; Wiley, 2017.

3. Bredar, A. R. C.; Chown, A. L.; Burton, A. R.; Farnum, B. H., Electrochemical Impedance Spectroscopy of Metal Oxide Electrodes for Energy Applications. ACS Appl. Ener. Mater. **2020**, 3, 66-98.

4. Wu, Z.; Liu, P.; Qu, X.; Ma, J.; Liu, W.; Xu, B.; Wang, K.; Sun, X. W., Identifying the Surface Charges and Their Impact on Carrier Dynamics in Quantum-Dot Light-Emitting Diodes by Impedance Spectroscopy. Advanced Optical Materials **2021**, 9, 2100389.

5. Taibl, S.; Fafilek, G.; Fleig, J., Impedance Spectra of Fe-Doped Srtio3 Thin Films Upon Bias Voltage: Inductive Loops as a Trace of Ion Motion. Nanoscale **2016**, 8, 13954-13966.

6. Fabregat-Santiago, F.; Garcia-Belmonte, G.; Mora-Seró, I.; Bisquert, J., Characterization of Nanostructured Hybrid and Organic Solar Cells by Impedance Spectroscopy. Phys. Chem. Chem. Phys. **2011**, 13, 9083–9118.

7. von Hauff, E., Impedance Spectroscopy for Emerging Photovoltaics. J. Phys. Chem. C **2019**, 123, 11329-11346.

8. Mora-Seró, I.; Garcia-Belmonte, G.; Boix, P. P.; Vázquez, M. A.; Bisquert, J., Impedance Spectroscopy Characterisation of Highly Efficient Silicon Solar Cells under Different Light Illumination Intensities. Energy & Environmental Science **2009**, 2, 678-686.

9. Fabregat-Santiago, F.; Bisquert, J.; Cevey, L.; Chen, P.; Wang, M.; Zakeeruddin, S. M.; Grätzel, M., Electron Transport and Recombination in Solid-State Dye Solar Cell with Spiro-Ometad as Hole Conductor. Journal of the American Chemical Society **2009**, 131, 558-562.

10. Wang, Q.; Moser, J.-E.; Grätzel, M., Electrochemical Impedance Spectroscopic Analysis of Dye-Sensitized Solar Cells. The Journal of Physical Chemistry B **2005**, 109, 14945-14953.

11. Arredondo, B.; Romero, B.; Del Pozo, G.; Sessler, M.; Veit, C.; Würfel, U., Impedance Spectroscopy Analysis of Small Molecule Solution Processed Organic Solar Cell. Solar Energy Materials and Solar Cells **2014**, 128, 351-356.

12. Guerrero, A.; Garcia-Belmonte, G.; Mora-Sero, I.; Bisquert, J.; Kang, Y. S.; Jacobsson, T. J.; Correa-Baena, J.-P.; Hagfeldt, A., Properties of Contact and Bulk Impedances in Hybrid Lead Halide Perovskite Solar Cells Including Inductive Loop Elements. J. Phys. Chem. C **2016**, 120, 8023-8032.

13. Pockett, A.; Eperon, G. E.; Peltola, T.; Snaith, H. J.; Walker, A. B.; Peter, L. M.; Cameron, P. J., Characterization of Planar Lead Halide Perovskite Solar Cells by Impedance Spectroscopy, Open Circuit Photovoltage Decay and Intensity-Modulated Photovoltage/Photocurrent Spectroscopy. J. Phys. Chem. C **2015**, 119, 3456–3465.

14. Zarazua, I.; Bisquert, J.; Garcia-Belmonte, G., Light-Induced Space-Charge Accumulation Zone as Photovoltaic Mechanism in Perovskite Solar Cells. The Journal of Physical Chemistry Letters **2016**, 7, 525-528.

15. Guerrero, A.; Bisquert, J.; Garcia-Belmonte, G., Impedance Spectroscopy of Metal Halide Perovskite Solar Cells from the Perspective of Equivalent Circuits. Chemical Reviews **2021**, 121, 14430–14484.

16. Ravishankar, S.; Almora, O.; Echeverría-Arrondo, C.; Ghahremanirad, E.; Aranda, C.; Guerrero, A.; Fabregat-Santiago, F.; Zaban, A.; Garcia-Belmonte, G.; Bisquert, J., Surface Polarization Model for the Dynamic Hysteresis of Perovskite Solar Cells. The Journal of Physical Chemistry Letters **2017**, 8, 915-921.

17. Parikh, N.; Narayanan, S.; Kumari, H.; Prochowicz, D.; Kalam, A.; Satapathi, S.; Akin, S.; Tavakoli, M. M.; Yadav, P., Recent Progress of Light Intensity-Modulated Small Perturbation Techniques in Perovskite Solar Cells. physica status solidi (RRL) – Rapid Research Letters **2021**, n/a, 2100510.

18. Ravishankar, S.; Aranda, C.; Sanchez, S.; Bisquert, J.; Saliba, M.; Garcia-Belmonte, G., Perovskite Solar Cell Modeling Using Light and Voltage Modulated Techniques. J. Phys. Chem. C **2019**, 123, 6444-6449.

19. Bou, A.; Pockett, A.; Raptis, D.; Watson, T.; Carnie, M. J.; Bisquert, J., Beyond Impedance Spectroscopy of Perovskite Solar Cells: Insights from the Spectral Correlation of the Electrooptical Frequency Techniques. J. Phys. Chem. Lett. **2020**, 11, 8654-8659.

20. Bou, A.; Āboliņš, H.; Ashoka, A.; Cruanyes, H.; Guerrero, A.; Deschler, F.; Bisquert, J., Extracting in Situ Charge Carrier Diffusion Parameters in Perovskite Solar Cells with Light Modulated Techniques. ACS Energy Lett. **2021**, 2248-2255.

21. Halme, J.; Miettunen, K.; Lund, P., Effect of Nonuniform Generation and Inefficient Collection of Electrons on the Dynamic Photocurrent and Photovoltage Response of Nanostructured Photoelectrodes. J. Phys. Chem. C **2008**, 112, 20491-20504.

22. Bisquert, J.; Janssen, M., From Frequency Domain to Time Transient Methods for Halide Perovskite Solar Cells: The Connections of Imps, Imvs, Tpc, and Tpv. The Journal of Physical Chemistry Letters **2021**, 12, 7964-7971.

23. Bisquert, J., Theory of the Impedance of Electron Diffusion and Recombination in a Thin Layer. The Journal of Physical Chemistry B **2002**, 106, 325-333.

24. Janssen, M.; Bisquert, J., Locating the Frequency of Turnover in Thin-Film Diffusion Impedance. The Journal of Physical Chemistry C **2021**, 125, 15737-15741.

25. Wang, Q.; Ito, S.; Grätzel, M.; Fabregat-Santiago, F.; Mora-Seró, I.; Bisquert, J.; Bessho, T.; Imai, H., Characteristics of High Efficiency Dye-Sensitized Solar Cells. J. Phys. Chem. B **2006**, 110, 19406-19411.

26. Bisquert, J.; Fabregat-Santiago, F.; Mora-Seró, I.; Garcia-Belmonte, G.; Giménez, S., Electron Lifetime in Dye-Sensitized Solar Cells: Theory and Interpretation of Measurements. J. Phys. Chem. C **2009**, 113, 17278–17290.

27. Martinson, A. B. F.; Goes, M. S.; Fabregat-Santiago, F.; Bisquert, J.; Pellin, M. J.; Hupp, J. T., Electron Transport in Dye-Sensitized Solar Cells Based on Zno Nanotubes: Evidence for Highly Efficient Charge Collection and Exceptionally Rapid Dynamics. The Journal Physical Chemistry A **2009**.

28. Stranks, S. D.; Eperon, G. E.; Grancini, G.; Menelaou, C.; Alcocer, M. J. P.; Leijtens, T.; Herz, L. M.; Petrozza, A.; Snaith, H. J., Electron-Hole Diffusion Lengths Exceeding 1 Micrometer in an Organometal Trihalide Perovskite Absorber. Science **2013**, 342, 341-344.

29. Johnston, M. B.; Herz, L. M., Hybrid Perovskites for Photovoltaics: Charge-Carrier Recombination, Diffusion, and Radiative Efficiencies. Acc. Chem. Res. **2016**, 49, 146-154.

30. Park, N.-G., Perovskite Solar Cells: An Emerging Photovoltaic Technology. Materials Today **2015**, 18, 65-72.

31. Pockett, A.; Spence, M.; Thomas, S. K.; Raptis, D.; Watson, T.; Carnie, M. J., Beyond the First Quadrant: Origin of the High Frequency Intensity-Modulated Photocurrent/Photovoltage Spectroscopy Response of Perovskite Solar Cells. Solar RRL **2021**, 5, 2100159.

32. Bertoluzzi, L.; Bisquert, J., Investigating the Consistency of Models for Water Splitting Systems by Light and Voltage Modulated Techniques. The Journal of Physical Chemistry Letters **2017**, 8, 172-180.

33. Alvarez, A. O.; Ravishankar, S.; Fabregat-Santiago, F., Combining Modulated Techniques for the Analysis of Photosensitive Devices. Small Methods **2021**, n/a, 2100661.

34. Pockett, A.; Raptis, D.; Meroni, S. M. P.; Baker, J.; Watson, T.; Carnie, M., Origin of Exceptionally Slow Light Soaking Effect in Mesoporous Carbon Perovskite Solar Cells with Ava Additive. J. Phys. Chem. C **2019**, 123, 11414-11421.

35. Krückemeier, L.; Krogmeier, B.; Liu, Z.; Rau, U.; Kirchartz, T., Understanding Transient Photoluminescence in Halide Perovskite Layer Stacks and Solar Cells. Adv. Energy Mater. **2021**, 11, 2003489.

36. Kirchartz, T.; Márquez, J. A.; Stolterfoht, M.; Unold, T., Photoluminescence-Based Characterization of Halide Perovskites for Photovoltaics. Adv. Energy Mater. **2020**, 10, 1904134.

Supporting Information

Limited Information of Impedance Spectroscopy about Electronic Diffusion Transport: The Case of Perovskite Solar Cells

Agustín Bou,[1*] Adam Pockett,[2] Héctor Cruanyes,[1] Dimitrios Raptis,[2] Trystan Watson,[2]
Matthew J. Carnie[2] and Juan Bisquert[1*]

[1] Institute of Advanced Materials (INAM), Universitat Jaume I, 12006 Castelló, Spain

[2] SPECIFIC, Materials Research Center, College of Engineering, Swansea University, Swansea SA1 8EN, United Kingdom

Corresponding authors: Agustín Bou acatala@uji.es and Juan Bisquert bisquert@uji.es

Experimental Methods

Materials: PbI_2 (99%, Sigma-Aldrich), MAI (CH_3NH_3I, anhydrous, Dyesol), 5-ammonium valeric acid iodide (5-AVAI, Dyesol) and γ-Butyrolactone (Sigma Aldrich) were used as received for preparation of perovskite precursors. Stacks were prepared using the following: anhydrous 2-propanol (IPA, 99.5%), carbon paste (Gwent electronic materials), ZrO_2 paste (Solaronix), TiO_2 paste (30NR-D, Dyesol), terpineol (95%, Sigma-Aldrich), and titanium diisopropoxide bis (acetylacetonate) (TAA, 75% in IPA, Sigma-Aldrich).

Device fabrication: The FTO substrate was initially patterned with a Nb:YVO4 laser (532nm), then cleaned with a solution of Hellmanex in deionised water, rinsed with acetone, IPA, and finally plasma cleaned in an O_2 atmosphere for 5 min. A compact TiO_2 blocking layer was sprayed with a solution of 10% Titanium di-isopropoxide bis (acetylacetonate) in IPA on the FTO substrate, which was kept at 300 ^oC on a hot plate. Mesoporous layers of TiO_2, ZrO_2, and carbon were sequentially screen printed. The annealing of each layer occurred at 550 ^oC for TiO_2, and 400 ^oC for ZrO_2 and carbon. The ZrO2 layer was printed three times to increase thickness with drying at 100 ^oC for each layer. The paste for the TiO_2 layer was diluted in terpineol in a 1:1 ratio by weight. The other pastes were used as bought. The precursor perovskite solution was synthesized by dissolving 0.439 of PbI_2, 0.1514 of MAI and 0.0067 g of 5-AVAI in 1 ml γ-butyrolactone at 60 ^oC. 25 μL of the solution was drop casted on the 1 cm^2 active area of the cells through the carbon layer. Allowing 10 minutes time for the solution to percolate throughout the stack, the devices were annealed in a fan oven for 1 h at 50 ^oC. The finished solar cells were then exposed to 70% relative humidity at 40 °C for 24 hours to induce a recrystallisation and then dried in a vacuum oven before measuring to reach their final efficiency.

Films thicknesses were measured with a DEKTAK 150 profilometer system and found as follows (average values):

- TiO2=0.8 µm, ZrO2=4.5 µm, total stack= 19.5 µm

Characterization: Electrochemical impedance spectroscopy (EIS) measurements were performed on unmasked devices under 470 nm LED illumination using a Zahner CIMPS-X photoelectrochemical workstation. Measurements were performed at open-circuit with an AC amplitude of 10 mV over the frequency range 10 MHz to 1 Hz.

IMPS/IMVS measurements were performed using a custom built system described in **ref**.[1] A 470 nm LED (Broadcom) was driven directly from the sinusoidally modulated voltage output of an Agilent 33522B waveform generator (WFG). To provide an additional higher intensity DC offset a 470 nm LED (Thorlabs) was driven by a Thorlabs LEDD1B driver. The total DC intensity was adjusted to give a 1 Sun equivalent Jsc from the device under test, and the AC intensity was adjusted to be approximately 5% of this intensity. A silicon reference photodiode (Newport 818-UV) was used to calibrate the light intensity. Lower intensities were achieved using a series of calibrated neutral density filters.

For IMPS measurements the photocurrent response of the cell under test was connected to the input of a lock-in amplifier (Stanford Research Systems SR865A), via a Femto DHPCA 100 transimpedance amplifier (TIA). A voltage bias was applied to the device through a DC bias tee to hold the cell at open-circuit. For IMVS measurements the cell was connected directly to the lock-in amplifier input (10 MΩ input impedance). Measurements were performed over the frequency range 4 MHz to 1 Hz.

The attenuation and phase shift of the modulated LED illumination at high frequency was measured using a high bandwidth, small area PIN photodiode (Hamamatsu S5971) via the TIA. At each frequency, the amplitude of the modulated voltage signal from the WFG was increased until the amplitude of the LED illumination matched the predetermined value (5% of DC intensity). The phase shift of the WFG to lock-in reference signal was also adjusted to ensure that the lock-in was measuring in phase with the modulated light intensity (rather than the LED driving signal). Hardware was controlled by custom LabView software.

Additional Simulations

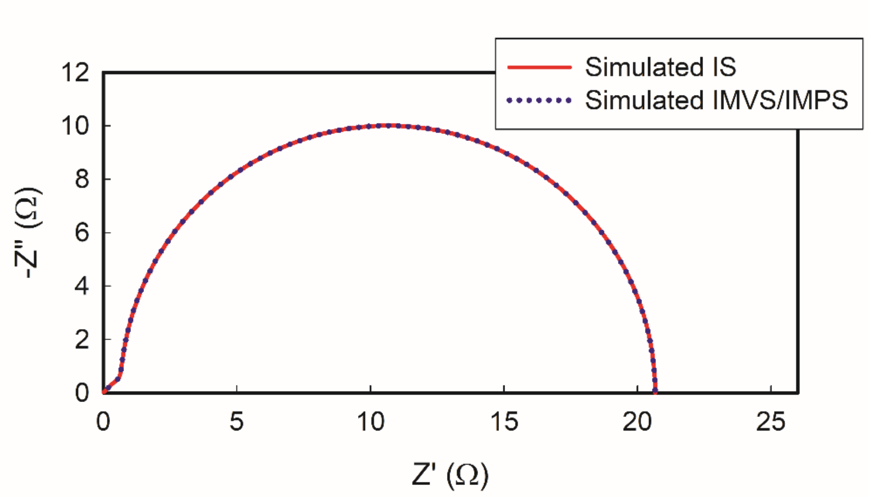

Figure S1. Simulated complex plane plot of both the IS of the diffusion-recombination and the ratio of the IMVS and IMPS given by Eq. 10

J-V characteristics

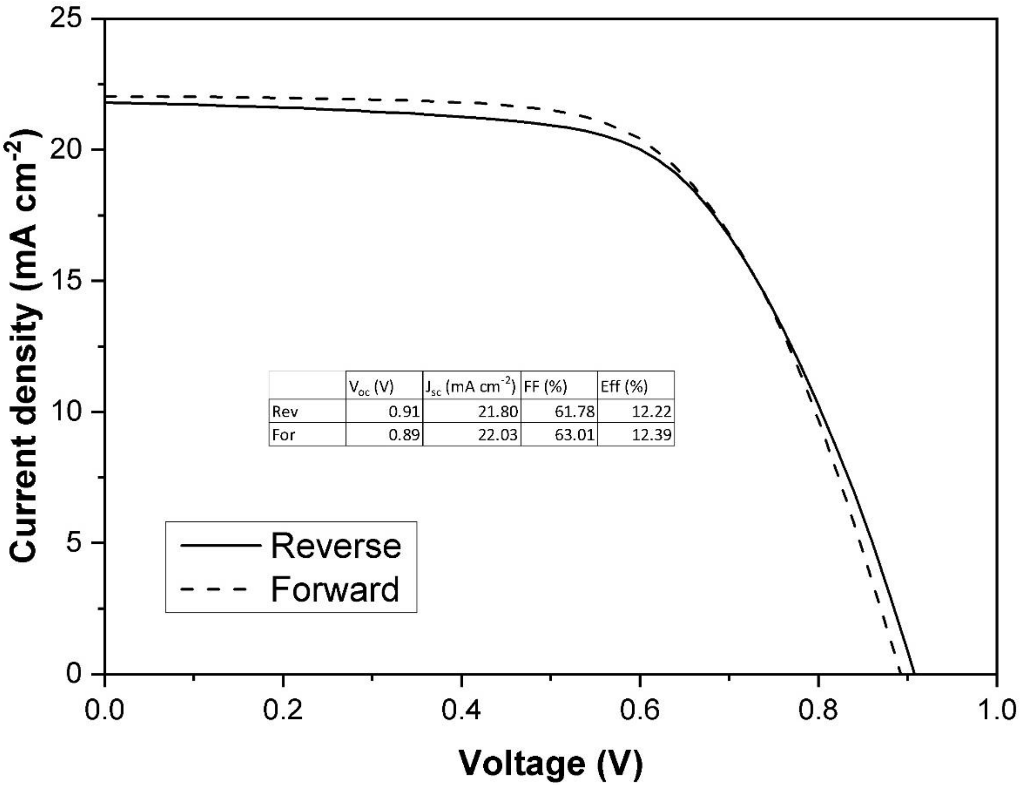

	V_{oc} (V)	J_{sc} (mA cm^{-2})	FF (%)	Eff (%)
Rev	0.91	21.80	61.78	12.22
For	0.89	22.03	63.01	12.39

Figure S2. Current-Voltage characteristics of the measured carbon-based perovskite solar cell.

IS, IMPS and IMVS spectra at different illumination intensities

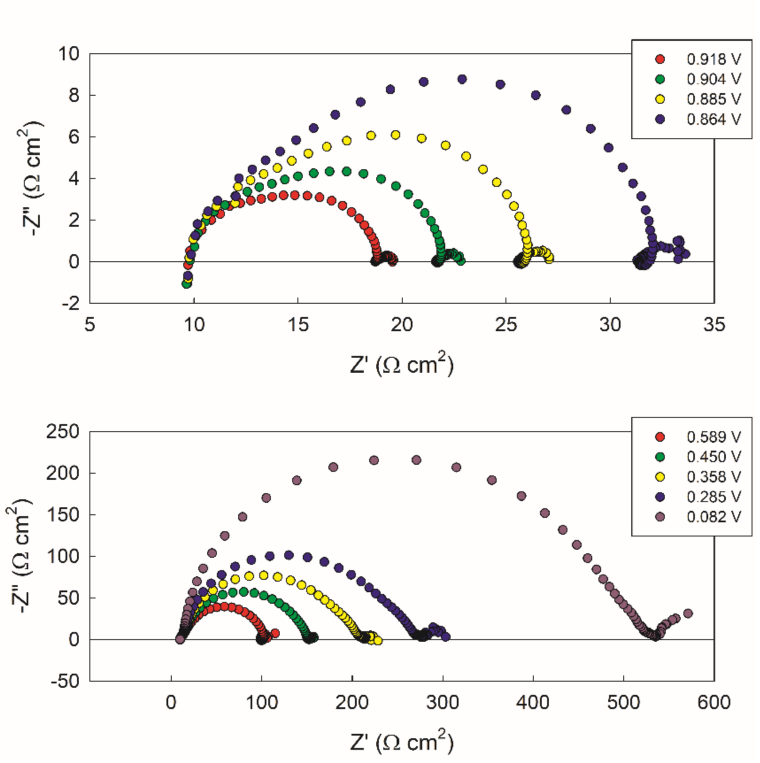

Figure S3. IS complex plane plots for a carbon solar cell at open circuit voltage and at different light intensities from 1sun (highest V_{OC}) to 0.01 sun (lowest V_{OC})

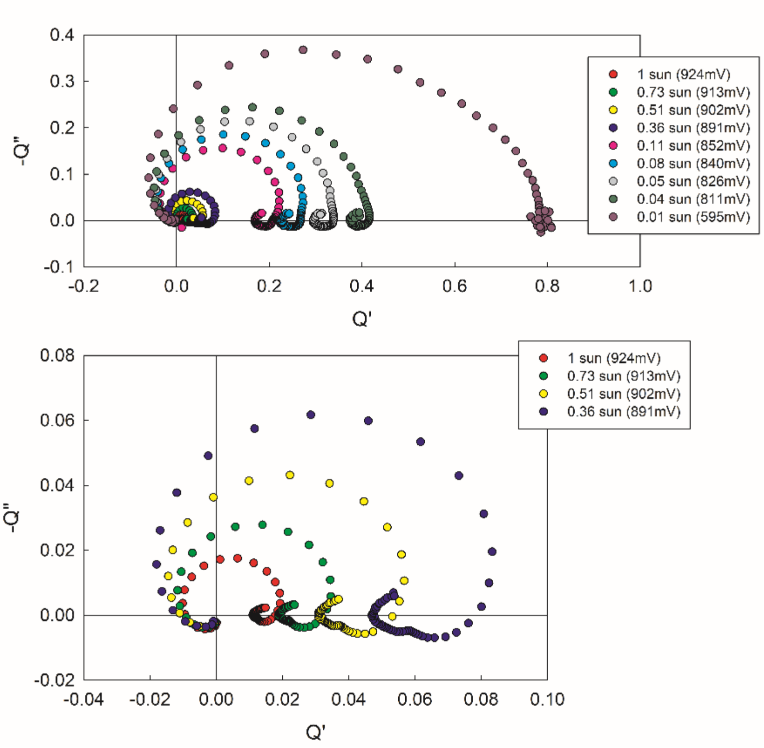

Figure S4. IMPS complex plane plots for a carbon solar cell at open circuit voltage and at different light intensities from 1sun (highest V_{OC}) to 0.01 sun (lowest V_{OC})

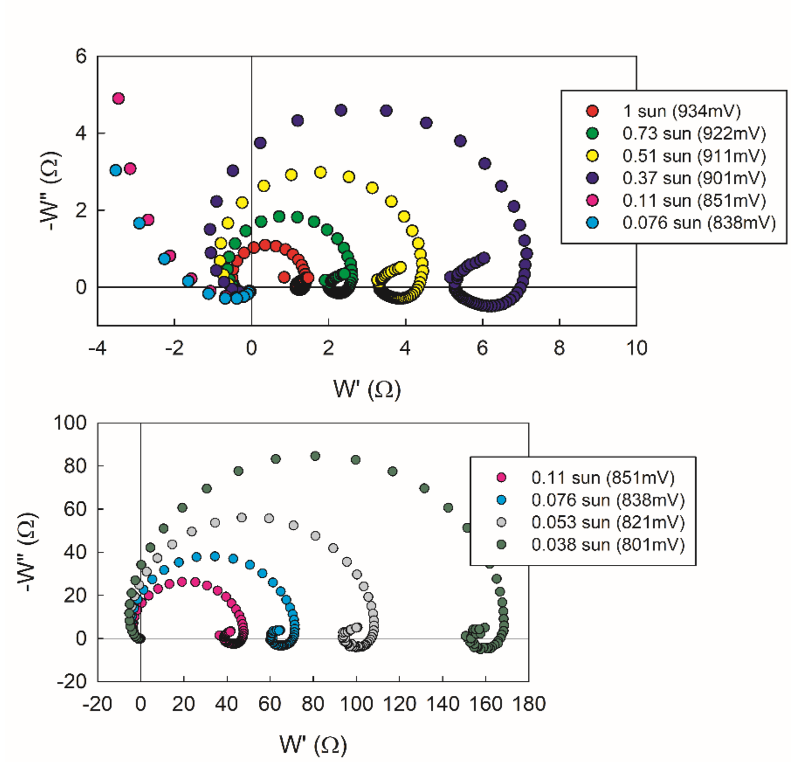

Figure S5. IMVS complex plane plots for a carbon solar cell at open circuit voltage and at different light intensities from 1sun (highest V_{OC}) to 0.038 sun (lowest V_{OC})

References

1. Pockett, A.; Spence, M.; Thomas, S. K.; Raptis, D.; Watson, T.; Carnie, M. J., Beyond the First Quadrant: Origin of the High Frequency Intensity-Modulated Photocurrent/Photovoltage Spectroscopy Response of Perovskite Solar Cells. *Solar RRL* **2021**, *5*, 2100159.

Chapter 5

Publication 4

Impedance Spectroscopy Dynamics of Biological Neural Elements: From Memristors to Neurons and Synapses

Bou, A.; Bisquert, J. Impedance Spectroscopy Dynamics of Biological Neural Elements: From Memristors to Neurons and Synapses, *The Journal of Physical Chemistry B*, **2021**, 125, 9934–9949.

Candidate's Contribution

Nature of Contribution	Extent of Contribution
• Calculated the Hodgkin-Huxley model impedance response • Performed the simulations and build the figures for the Hodgkin-Huxley model • Wrote the part of the manuscript and revised the rest	45%

Introduction

This work studies theoretically the IS response of neural elements, with the aim of knowing the experimental responses to be sought in artificial devices that seek to copy these biological elements. The work derivates the equivalent circuits from basic elements, such as memristors, to other complicated neuron models, finding similarities with the responses of perovskite devices.

Published Manuscript

Impedance spectroscopy dynamics of biological neural elements: from memristors to neurons and synapses

Agustín Bou, Juan Bisquert*

Institute of Advanced Materials (INAM), Universitat Jaume I, 12006 Castelló, Spain

Email: bisquert@uji.es

Abstract

Understanding the operation of neurons and synapses is essential to reproduce biological computation. Building artificial neuromorphic networks opens the door to a new generation of faster and low energy consuming electronic circuits for computation. The main candidates to imitate the natural biocomputation processes, such as the generation of action potentials and spiking, are memristors. Generally, the study of the performance of material neuromorphic elements is done by the analysis of time transient signals. Here, we present an analysis of neural systems in the frequency domain by the technique of the small amplitude ac impedance spectroscopy. We start from the constitutive equations for the conductance and memory effect, and we derive and classify the impedance spectroscopy spectra. We first provide a general analysis of a memristor and demonstrate that this element can be expressed as a combination of simple parts. In particular we derive a basic equivalent circuit where the memory effect is represented by a RL branch. We show that this ac model is quite general and describes the inductive/negative capacitance response in many systems such as halide perovskites and organic LEDs. Thereafter we derive the impedance response of the integrate-and-fire exponential adaptative neuron model, that introduces a negative differential resistance and a richer set of spectra. Based on these insights, we provide an interpretation of the varied spectra that appear in the more general Hodgkin-Huxley neuron model. Our work provides important criteria to determine the properties that must be found in material realizations of neuronal elements. This approach has the great advantage that the analysis of highly complex phenomena can be based purely on the shape of experimental impedance spectra, avoiding the need for specific modelling of rather involved material processes that produce the required response.

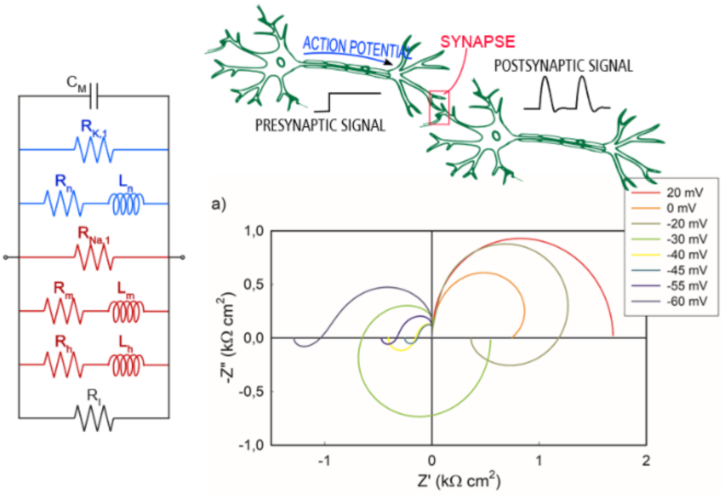
C_M
$R_{K,1}$
R_n
L_n
$R_{Na,1}$
R_m
L_m
R_h
L_h
R_l
ACTION POTENTIAL
SYNAPSE
POSTSYNAPTIC SIGNAL
PRESYNAPTIC SIGNAL
a)
20 mV
0 mV
-20 mV
-30 mV
-40 mV
-45 mV
-55 mV
-60 mV
1,0
0,5
0,0
-0,5
-1,0
-Z'' (kΩ cm²)
-1
0
1
2
Z' (kΩ cm²)

Contents

1. Introduction

Biological intelligence co-localizes memory and computing, enabling the brain to carry out robust and efficient parallel computation with extremely low-power consumption. Neuromorphic networks consist of large arrays of nanoscale inorganic and hybrid materials components. They can reach high levels of integration density to provide compact low power electronic circuits for autonomous intelligence adapted to buildings, vehicles, and equipment.[1-6] These bioinspired artificial computation networks open the opportunity to overcome the "Von-Neumann bottleneck" related to the time and energy spent transporting data between memory and processor.[7]

Neurons and synapses are the main elements of biological computation. Neurons operate by gating mechanisms controlled by voltage-gated ion channels that modify the membrane potentials. Voltage-gated sodium channels are proteins which transfer sodium ions across the membrane depending on the electrochemical potential gradient controlled by the transmembrane difference of ion concentration. Opening of the sodium channel results in an increased electrochemical potential inside the membrane and leads to depolarization. When the potential exceeds a positive threshold value there is a positive feedback of Na^+ influx that provokes a large depolarization burst termed the action potential. At the same time voltage-gated potassium channels become activated and produce an outward flux of K^+ that leads to the repolarization completing a negative feedback loop. Neurons realize communication with these electrical signals by receiving trains of voltage spikes at synapses, integrating these inputs, and firing spikes consisting of repetitive action potentials in turn. The synapses are able to change the strength of connectivity, what regulates biological learning, memory and analog computation. The synchronicity of spike trains produces either potentiation or depression of synaptic weights, in the spike-timing dependent plasticity which occurs as a short time plasticity or long-time plasticity mechanism, according to the duration of the change. Additional mechanisms of learning are the Hebbian correlational learning, reinforcement, habituations, and others.

Understanding the mechanisms of generation of action potentials, spiking, and the adjustment of the weights of connections in time-dependent plasticity and learning mechanisms are the basic building blocks to realize the neuromorphic computation. For the construction of neural networks, it is necessary to build basic material components and circuits that emulate the underlying biophysical switching mechanisms of neurons and synapses and reproduce their detailed real-time dynamics.[2,8-10] The temporal response of the electrical signal in terms of the biological structure has been well described by a variety of models, from the integrate-and-fire model to the Hodgkin-Huxley model.[11-13] These models provide a fundamental target reference to reproduce the time dynamics with material components. There have been intensive efforts to build an electronic device with properties similar to the Hodgkin–Huxley axon, such as the neuristor.[14]

In order to obtain a fundamental understanding of the dynamic response of neurons and synapses, here we propose that important insight can be gained by analyzing the candidate material elements in the frequency domain, as outlined in Figure 1.

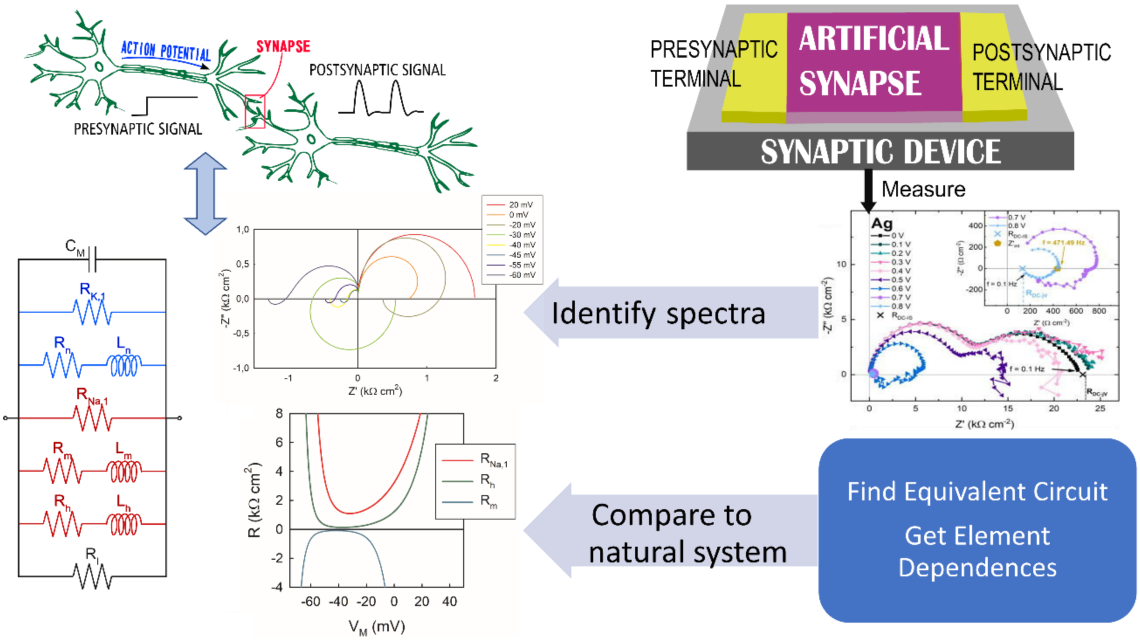

Figure 1. Scheme for the IS analysis of artificial synaptic devices (right) with respect to the response of the natural synapsis (left).

In the next Section we explain important basic aspects of the technique of impedance spectroscopy (IS) and lay out the general tasks of the method proposed. Thereafter we will follow a ladder of increasing complexity, starting with the analysis of elementary memristors, and then addressing the IS response of the models for neurons, first for the two variable adaptative integrate-and-fire model, and then for the four-dimensional Hodgkin-Huxley model that describes the operation of neuron spiking by the concerted actions of the sodium and potassium ion channels.

2. Impedance spectroscopy

2.1. Introduction to impedance spectroscopy

The technique of small amplitude IS is widely used in electrochemistry and material science to determine the electrical response of a system.[15,16] It is an important tool for the characterization of emergent solar cells[16,17] and perovskite solar cells.[18-20] It is also used for many applications in biophysics[21,22] such as research in cells[23], antimicrobials,[24] medicine and healthcare,[25,26] and biosensorics.[27] The impedance of the intrinsic neuronal response determines the cooperation in a network.[28]

The impedance is measured by a small perturbation over a steady state at angular frequency ω, and it can be presented in terms of the real and imaginary parts

$$Z(\omega) = Z'(\omega) + iZ''(\omega) \tag{1}$$

The complex capacitance $C(\omega)$ is defined from the impedance as

$$C(\omega) = \frac{1}{i\omega Z(\omega)} \tag{2}$$

It can be separated into real and imaginary parts as

$$C(\omega) = C'(\omega) - iC''(\omega) \tag{3}$$

When we study the impedance response of any system, we aim to find the equivalent circuit (EC) that best describes the impedance spectra generated by the system, for extracting all the information provided by the spectra. Therefore, figuring out which is the EC of the system we are studying is key for having a satisfactory analysis and a proper interpretation of the measurements. IS gives insight about physical properties and mechanisms: given a type of spectra and EC model, one can learn about the system that generated it.

The impedance measured in a system is not constant and the spectra evolve as we change the applied voltage. This is not a problem since a single EC with variable elements is able to reproduce a wide variety of spectra as we will see in Section 2.2. These variable elements hold valuable information about the operation of the systems, therefore knowing which is the dependence of the elements with voltage is key to uncover internal mechanisms.

In order to clarify this method, we show an example of measured impedance spectra in a perovskite solar cell at different applied voltages from a previous work in Figure 2a.[29] This set of spectra are fitted with the EC shown in Figure 2c. It is observed that the elements of the circuit are not constant, in fact the vary with the applied voltage. Figure 2b shows the exponential variation of both resistances and the inductor with voltage, which is a common behavior in solar cell devices.

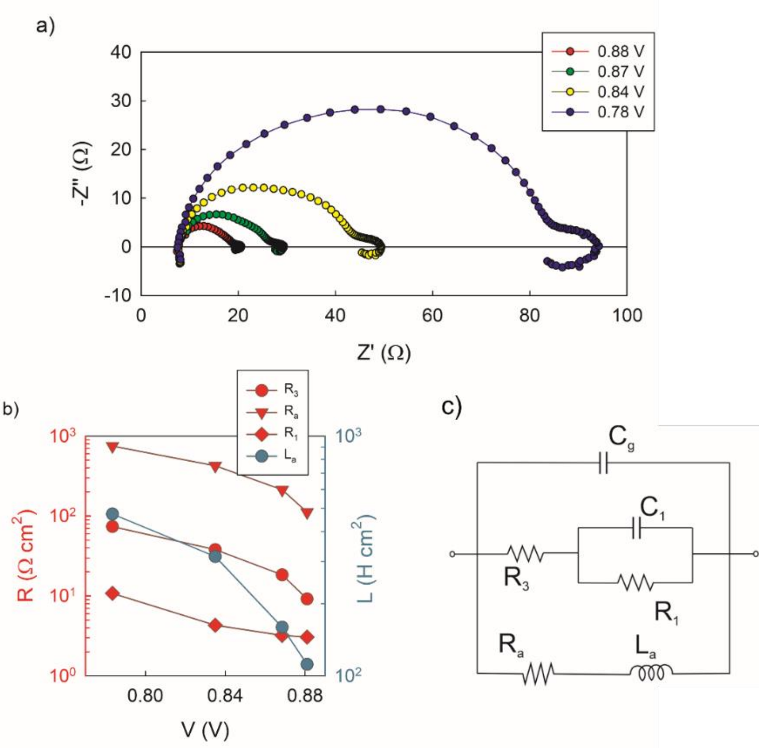

Figure 2. (a) Impedance complex plane plot of a perovskite solar cell at different applied voltages fitted with the same EC. (b) Extracted resistances from (a) fitting showing an exponential dependence. Adapted from [29].

When a satisfactory EC model has been found, one has to take into account that there are several alternative arrangements that describe the same model.[30] The selection of the EC needs to be done on the basis of the physical interpretation of the elements and the experimentation of a variety of samples with different morphologies and materials combinations.

2.2. IS model with capacitor and inductor

We show a complete analysis of an EC containing a capacitor and an inductor. It will be shown later that this model is representative of a simple memristor, and of interest for the subsequent analysis of neuron models. In this section, we will see the shape of the spectra depending on the values of the elements of the circuit. Later, we will do a further analysis considering the parameters of the kinetic models, which govern the elements of the circuit. A full interpretation of EC and model parameters is presented in SI.

The circuit that we are going to use is represented in Figure 3. The impedance generated by this circuit is

$$Z(\omega) = \left[{R_b}^{-1} + C_m s + (R_a + L_a s)^{-1}\right]^{-1} \tag{4}$$

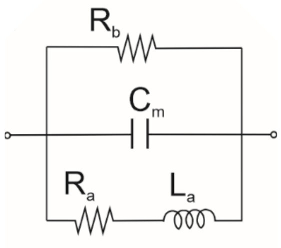

Figure 3. Equivalent circuit with an inductor and a capacitor, representative of a memristor.

The circuit is able to generate a wide variety of spectra, depending on the relation between the elements of the circuit.

The dc resistance of the circuit, which is a key parameter for the shape of the spectra can be calculated as

$$R_{dc} = \left(\frac{1}{R_a} + \frac{1}{R_b}\right)^{-1} \tag{5}$$

First of all, we consider the case where both resistances in the EC are positive. Therefore, R_{dc} will be positive. In this case we have two possibilities depending on whether the spectra cross the real axis or not. These spectra are shown in Figure 4 indicating the relation between some of the elements and the time constant τ_k, characteristic of the RL branch and defined as

$$\tau_k = \frac{L_a}{R_a} \tag{6}$$

When τ_k is greater than the product $R_a C_m$ we get a spectrum of the type of Figure 4a, i.e. an arc in the first quadrant that loops into the fourth quadrant. Otherwise, we obtain the spectrum in Figure 4b, an arc in the first quadrant that can loop or not, but never goes into the fourth quadrant.

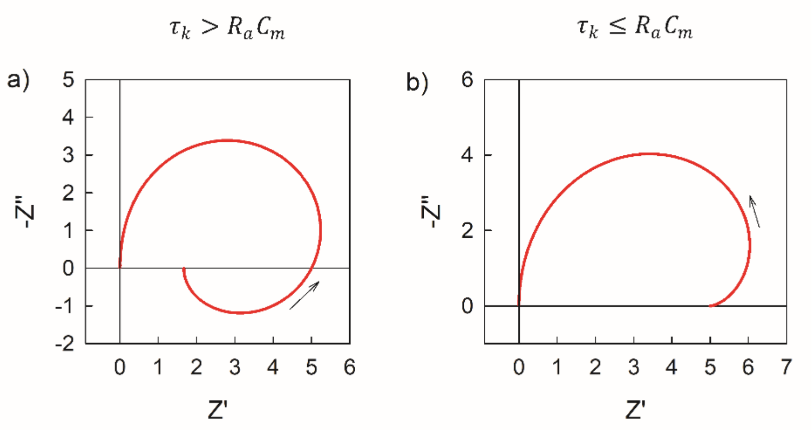

Figure 4. Complex plane impedance spectra for EC in Figure 3. (a) R_a= 2, R_b = 10, C_m= 10, L_a= 200. (b) R_a= 10, R_b = 10, C_m= 10, L_a= 1000. The arrow indicates the direction of increasing frequency.

We now look at the conditions for having a positive dc resistance but a spectrum that crosses the imaginary axis. This means that there will be a region where the real part of the impedance is negative, although the total resistance of the circuit R_{dc} is positive. The condition for the impedance to cross the imaginary axis is:

$$-R_a > R_b \tag{7}$$

This means that one or both the resistances must be negative. However, to maintain the condition that the dc resistance is positive, we need one of the resistances to be positive. This kind of spectra have a part of the real impedance in the real negative side, although the impedance at zero frequency is positive. This is defined by Koper as the "hidden negative impedance"[31-33] and it is a condition for the generation of spiking signals. Therefore, we show three examples of this kind of spectra in Figure 5 since the observation of a spectrum of this kind is key to build artificial synaptic devices.

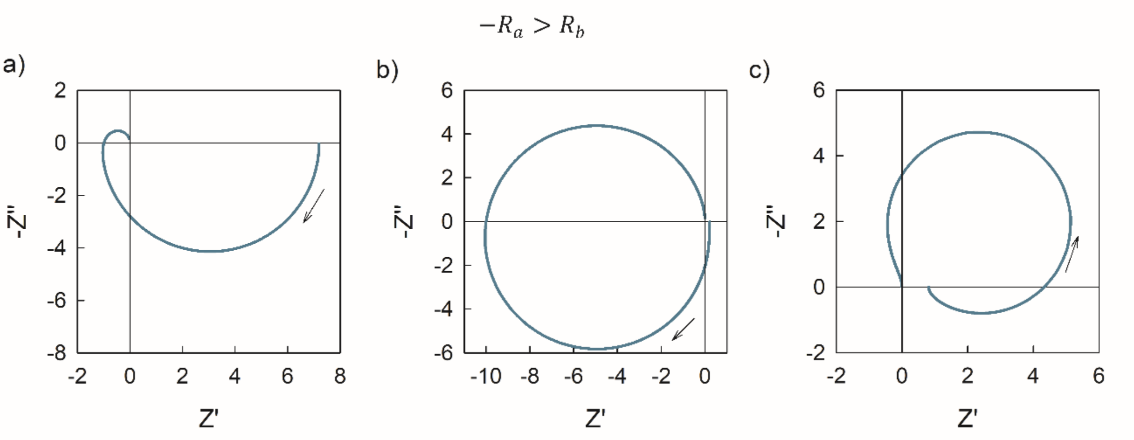

Figure 5. Complex plane impedance spectra for EC in Figure 3, where the dc resistance is $R_{dc} > 0$, and the condition for "hidden negative impedance" is satisfied. (a) R_a= 0.8, R_b = -9, R_{dc} = 7.2, C_m= 10, L_a= 80. (b) R_a= 0.2, R_b = -5, R_{dc} = 0.2083, C_m= 10, L_a= 20. (c) R_a= 0.5, R_b = -1.3, R_{dc} = 0.81, C_m= 100, L_a= 50. The arrow indicates the direction of increasing frequency.

Finally, we show two examples of spectra with negative R_{dc}, which means that the impedance at zero frequency will be negative. As we can see in Figure 6, this can be achieved with only one of the resistances being negative. As in Figure 4, when $\tau_k > R_a C_m$ (Figure 6a) the real axis is crossed, otherwise (Figure 6b) it is not.

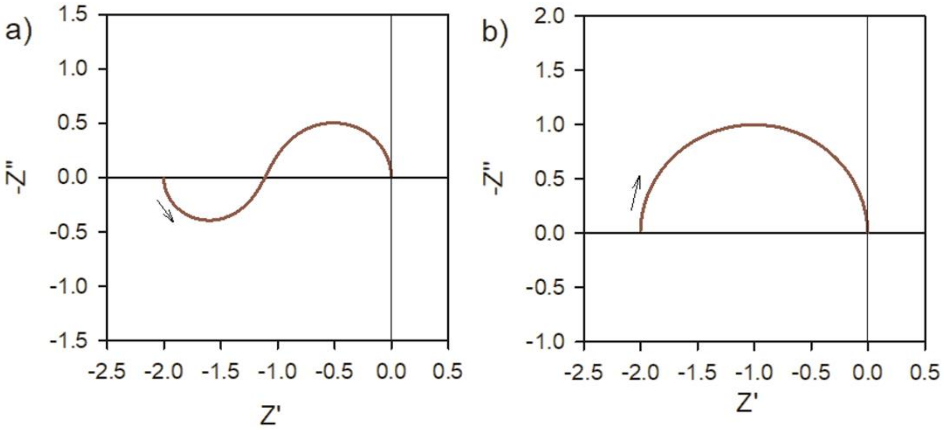

Figure 6. Complex plane impedance spectra for EC in Figure 3, with $R_{dc} < 0$. (a) R_a= 2, R_b = -1, R_{dc} = -2, C_m= 10, L_a= 200. (b) R_I = 1, R_a= 2, R_b = -1, R_{dc} = -2, τ_m= 100, τ_k= 10. The arrow indicates the direction of increasing frequency.

As we have seen in the different figures, the spectral features generated by the circuit in Figure 3 are diverse. The model takes different possible shapes according to the impedance parameters. The classification of patterns depending on physical parameters will be made in Section 3 where we attach specific meaning to the EC elements based on a physical model.

2.3. Impedance spectroscopy as a tool to emulate natural neural elements

The principal feature of the technique of IS is that the frequency is scanned over many decades and the consequent spectral response of the impedance provides specific information about the dominant resistive-capacitive processes in the sample. Traditionally IS gives insight about physical properties: given a type of spectra and EC model, what can we learn from the system that generated it?

In this paper we aim to establish the dominant IS characteristics of biological neural elements for computation, learning and artificial intelligence. The identification of impedance behavior provides a benchmark for the construction of material devices with the dynamical properties akin to natural neurons. In particular here we find inspiration in the theory of electrochemical oscillations based on impedance criteria that has been developed by Koper, using the methods of electrical control engineering.[31,34] It is remarkable that from the shape of experimental impedance spectra one may analyze extremely complex phenomena without the need for specific modelling of highly involved material processes that produce the physical response of interest.

Based on the operational understanding at the EC level we can ensure that an artificial system delivers the same operation as the natural system to copy. Then, for the construction of a device that can perform an artificial neuron we need a system that reproduces the frequency domain behavior of the target application. We can measure the impedance of the device and identify the possible similarities with the impedance response of the natural system, finding responses with similar ECs. We can adjust the different internal kinetic elements until we obtain the specific desired outcome.

At the single device level, we can obtain deep insight about the required responses. At present extensive data on IS of neurons is not available but the desired frequency domain response can be obtained by the analysis of the models that reproduce the natural neuron response in the time domain, such as the adaptative integrate-and-fire model and the Hodgkin-Huxley model.

A scheme of the method that is to be followed for the analysis of artificial synaptic devices is shown in Figure 1. Here, in the left we have represented the natural presynaptic neurons and a synapse with the spiking postsynaptic responses. Below, we represent the catalogue of spectra produced by the EC generated by the Hodgkin-Huxley model as well as the values of the variable resistances of the model. Knowing the possible shapes of the spectra, we need to measure impedances in our pretended neuronal devices and just identify the shapes found in the natural systems. Furthermore, we need to find an EC similar to that of the natural system and get similar dependences.

In the case of electrochemical oscillations and similar systems, the impedance response is associated to negative differential resistance (NDR) elements and also negative capacitance and inductive features. The pioneering work of Chua and coworkers[35,36] showed that the spiking of neurons operates in unstable regions according to the bifurcation theory that can be visualized by the stability criteria of impedance and admittance ("the edge of chaos"). A better comprehension of the dynamic role of these unfamiliar negative elements may form an important tool for the rapid diagnostic and assessment of the properties of materials systems that are candidate to artificial neurons. Our method relies on a classification of ECs associated to neuron models.

In an artificial spiking neural networks, the analog signals collected from the environment need to be converted into spiking signals with dynamic oscillation frequencies.[8] In synapses the input frequency of the signal modulates the conductivity.[37] In neurons the spike frequency increases with increased stimulus strength.[9] The connection between the output spiking frequency and the internal characteristic frequencies in the EC of the neuron must hold a deep connection. The dynamic spiking behavior under various input signals, such as rectangular, triangular, and sinusoidal pulses, needs to be investigated based on EC properties. One expects to find universality close to a critical point of the dynamical system, but not close to a fixed point. This topic is left for future investigations.

3. Memristors

3.1. Fundamental properties of memristors

At the present time the main resource for building neuromorphic networks are memristors.[38-40] A memristive device is a two-terminal structure that undergoes a voltage-controlled conductance change.[41] When the memristor is adapted as a neuron it has to integrate a pulse train and generate a voltage spike when a certain voltage is exceeded. On the other hand, for the use of a memristor as a synapse, it has to be programmed at distinct non-volatile resistive states to support spike timing dependent plasticity.[42-44] [45]

There is a wide variety of types of memristor suitable for bioinspired computation networks including silicon oxides,[46] silicon nitrides[47] and metal oxides.[48,49] The hybrid and organic electronics materials provide mechanical flexibility and bio-compatibility, enabling the formation of neuromorphic systems that can be smoothly interfaced to biological interfaces for the reception of stimuli.[4,50,51] The metal halide perovskites[52-57] is an emergent class of photovoltaic materials that have the advantage of easy fabrication and the property of mixed ionic-electronic conductor, with strong hysteresis effects induced by the slow ion motions. This ionic adaptation to external stimulus opens a significant opportunity to replicate the switching responses occurring in ionic channels of biological neural units. In practice, however, emulating the neurons, synapses, and their networks using ionic-electronic elements is extraordinarily challenging, due to the involved structure and multifunctionality of the biological elements, with highly complex responses that are usually studied in the time domain.

3.2. Basic kinetic equations of a general memristor

The memristor is a resistive element where the resistance depends on the history of one or more of the state variables of the system. The state variables are those variables necessary to determine the future behaviour of a system when the present state of the system and the inputs are known.[58] In the context of memristors a state variable is associated with the device material internal elements and its operation. The state variables must not be influenced independently by external variables such as a voltage or current applied to a third terminal.[59]

In terms of voltage u, current I, and the internal variable w, the current-voltage characteristic is therefore determined by two constitutive equations of the type[41]

$$I = G(w,u)u \tag{8}$$

$$\tau_k \frac{dw}{dt} = g(w,u) \tag{9}$$

Here, τ_k is a time constant for the relaxation of state variable w to an equilibrium dictated by the value of u. In the standard definition of a memristor the characteristic current-voltage shape when excited by a bipolar periodic stimulus (that goes from positive to negative voltage) is a pinched hysteresis loop that occurs in the first and the third quadrants of the I-u plane, passing through the origin since $I = 0$ at $u = 0$.

Often in the literature the denomination of an ideal memristor (in which the state variable is the voltage flux) is applied only to systems that have the only equilibrium point $\dot{w} = 0$ at the origin at $u = 0$,[59] as in Eq. (22) below. In order to investigate the IS characteristics here we take the more general denomination associated to memristors, in which $g(w, u) = 0$ allows other operation points along the current-voltage curve.

When the system is left to a steady state (a stable point) we obtain a curve $\bar{I} = G(\bar{u})\bar{u}$ according to the applied voltage, where the overbar denotes the value at steady state. An example is shown later in Eq. (29). Now we investigate the dynamics at a specific point.

To calculate the impedance response of the general model in Eqs. (8) and (9) we expand the terms for a small perturbation at steady state, indicating the small perturbation value by a tilde. We also take the Laplace transform of Eq. (9), $d/dt \to s$, where $s = i\omega$ in terms of the angular frequency ω of the small perturbation. We get a set of linear equations that contain the local information of the system:

$$\tilde{I} = G_w \bar{u}\, \tilde{w} + (\bar{G} + G_u \bar{u})\tilde{u} \tag{10}$$

$$\tau_k s \tilde{w} = g_w \tilde{w} + g_u \tilde{u} \tag{11}$$

The subscript denotes the partial derivative. The Eqs. (10) and (11) are also used in bifurcation theory to find the stability properties of the fixed points, as we comment on later in Eq. (35).

In order to obtain an EC representation of the dynamic of the system, let us define the following electrical elements, two resistances

$$R_b = (\bar{G} + G_u \bar{u})^{-1} \tag{12}$$

$$R_a = -\frac{g_w}{G_w g_u \bar{u}} \tag{13}$$

and an inductor

$$L_a = \frac{\tau_k}{G_w g_u \bar{u}} \tag{14}$$

We obtain the impedance

$$Z(\omega) = \frac{\tilde{u}}{\tilde{I}} = \left[{R_b}^{-1} + (R_a + L_a s)^{-1}\right]^{-1} \tag{15}$$

The EC formed by a resistive branch and RL branch is indicated in Figure 7A.

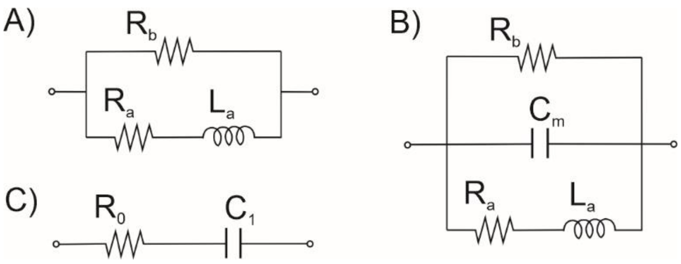

Figure 7. Equivalent circuits for general memristor models.

Now we introduce another factor to the constitutive equations. This is not included in the canonical definition of the memristor; however, it is very relevant for IS studies since in many material systems the variation of voltage is influenced by the charging of capacitors in addition to the conduction currents.

We extend the previous model as follows

$$\tau_m \frac{du}{dt} = R_I[I - G(w,u)u] \tag{16}$$

$$\tau_k \frac{dw}{dt} = g(w,u) \tag{17}$$

The charging capacitance is

$$C_m = \frac{\tau_m}{R_I} \tag{18}$$

and the impedance becomes

$$Z(\omega) = \left[{R_b}^{-1} + C_m s + (R_a + L_a s)^{-1}\right]^{-1} \tag{19}$$

The charging feature adds the capacitive line in the EC, as shown in Figure 7B.

We suggest the EC of Figure 7B as the reference behaviour for memristor dynamics, which is of the same type as the one in Figure 3. In the literature we find that this circuit was first described for a model of hydrogen oscillations on a platinum electrode,[31] what indicates that the model in Eqs. (16) and (17) is quite general and has been expressed in electrochemistry. We will see another version of this model corresponding perfectly to an integrate-and-fire neuron in the next section. If the charging is extremely fast ($\tau_m \to 0$) then the model returns to Eq. (8) and the capacitor effect vanishes.

Our analysis of the small ac perturbation shows that the memristor can be represented by a combination of standard circuit elements. In contrast to the original suggestion,[38] the memristor cannot be considered a fundamental circuit element in equal footing to resistance, capacitor and inductor, at least for the small ac impedance response. This problem has been discussed before.[60]

It is important to emphasize the dynamic response associated to the memory effect in this model, that can be seen in Figure 4. In principle the model indicates a single regular relaxation with a resistance R_b. However, it is clear that the dc resistance is smaller, since the parallel branch R_a reduces the final resistance. The memory effect associated to the w-equation in the memristor is indicated by the inductor. At high frequency the impedance of the inductor is very large and R_a does not contribute to the response. However, when the frequency is reduced, this branch becomes active and reduces the overall resistance of the system, by the loop in the fourth quadrant. A full analysis of hysteresis in current-voltage curves in this model has been presented recently.[61]

3.3. *Lead halide perovskite memristor and other material systems with inductive memristor behaviour*

An example of the characteristic action of a perovskite memristor is shown in Figure 8. When the voltage is scanned over a certain threshold there is a transition to a lower resistance state, while the initial high conductance resistance can be recovered by a reverse scan.

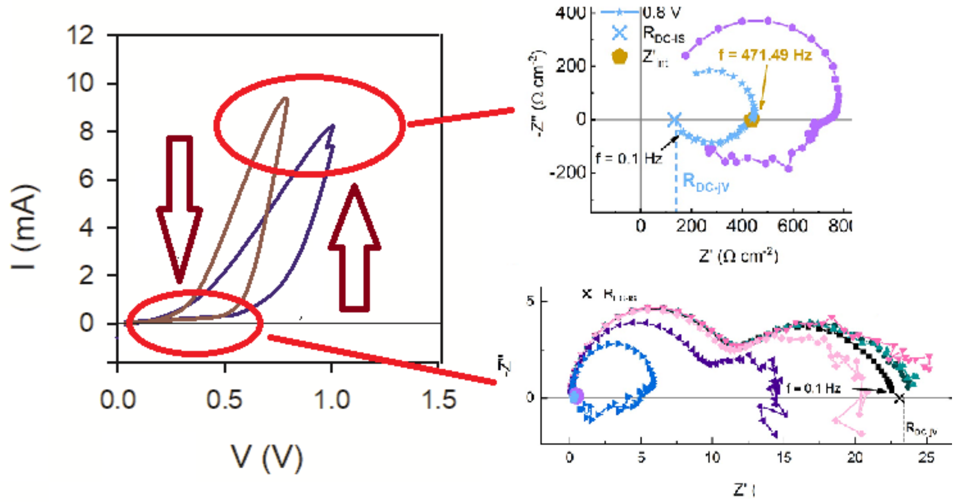

Figure 8. (a) Current-voltage curve of a FTO / PEDOT:PSS / 2D Ruddlesden-Popper perovskite/Ag (15 nm)/Au (85 nm) memristor device showing the transition from High Resistance State to Low Resistance State. (b) IS spectra evolution of the memristor at representative voltages. Reproduced from [33].

The spectrum of Figure 4a traces an arc in the fourth quadrant related to the action of the positive inductor element. This feature is very characteristic of lead halide perovskite solar cell impedance results, and has been reported in many publications.[62,63] The impedance patterns for a metal halide perovskite memristor around the transition state are shown in Figure 8b.[33] Before the onset of the high conduction state the impedance plot displays the typical two *RC* arcs of the perovskite solar cells.[64] Near the threshold voltage the memristive behaviour dominates the impedance, the former low frequency arc is transformed to the arc in the fourth quadrant by the action of the inductive element, that is associated to the effect of vacancies arriving to the electrode surface.[54]

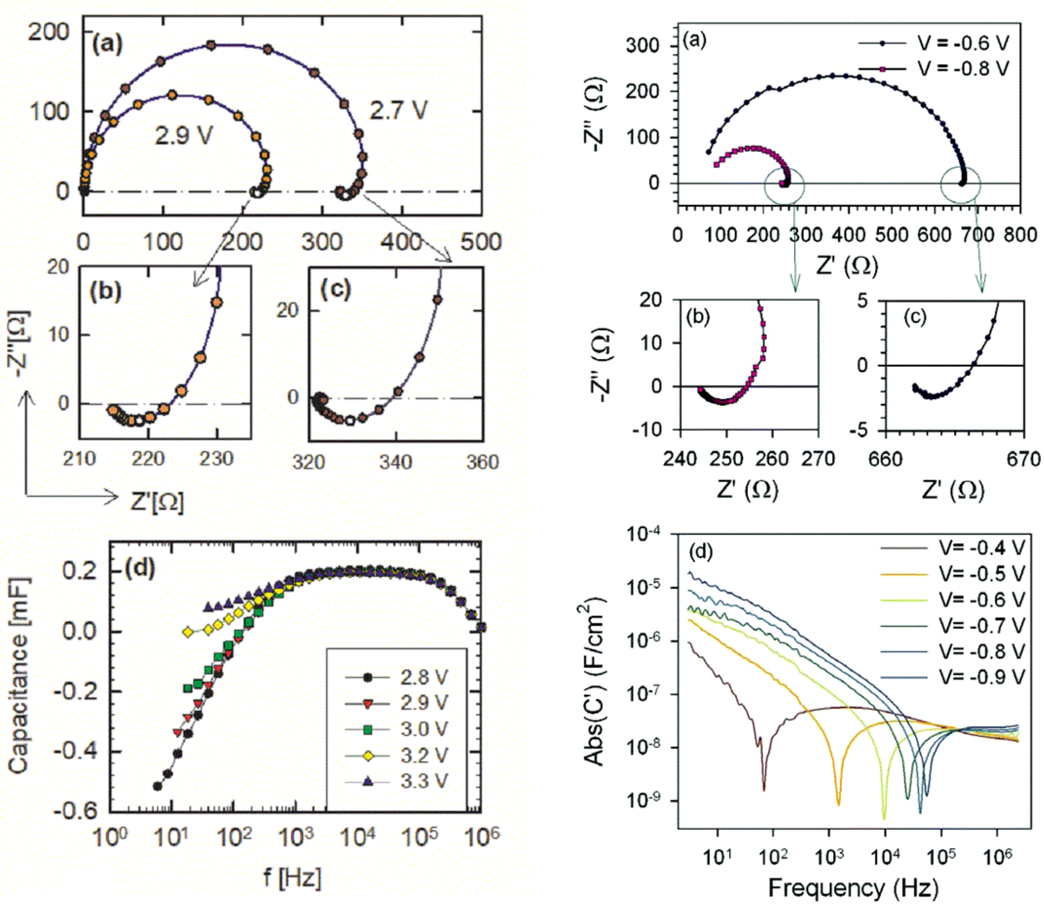

Figure 9. Left column. Results of the measurement of an ITO/PEDOT/superyellow/Ba/Al organic LED device. (a) Impedance plots for different bias voltages. (b) and (c) show a magnification of the observed inductive behavior at 2.9 V and 2.7 V, respectively. (d) Capacitance versus frequency for various bias voltages indicating a region of negative capacitance. Reproduced from [65]. Right column. Impedance spectra for a CdS/CdTe solar cell. (a–c) Complex plane plot of the impedance at two different forward bias in dark conditions. The frequency range employed in the measurement was 1 MHz to 0.1 Hz. (d) Absolute value of capacitance vs frequency at forward bias. Reproduced from [66].

It is interesting to remark that the inductor features shown in Figures 4 and 8 are not related to any magnetic properties. The behaviour of Figure 4a appears in a general type of “internal relaxation model”, in which the externally measured variable is coupled to a state variable, which relaxes to a pseudo-equilibrium state determined by the external variable. The first analysis of the relaxation impedance is due to Göhr and Schiller in a model for electrochemical reaction in which the rate constant *k* obeys a relaxation equation.[67]

A recent model was described in Ref. [68] to explain the inductive behaviour of lead halide perovskites.[62,63,69,70] In that model the external voltage V applied to the solar cell reaches equilibrium influenced by the relaxation of an internal surface voltage that is slowed down by ionic motion. It generates an EC including the *RL* branch of Figure 3. This model gives important insights to the hysteresis of current-voltage curves observed in perovskite solar cells.[71,72] In this system the inductor branch is associated to deleterious surface recombination that becomes active at low frequency, reducing the efficiency of the solar cell.[63] Additional examples of the general EC with inductor associated to interfacial electronic phenomena are sown in Figure 9 for the measurements of an OLED device[65] and a CdS/CdTe solar cell.[66] The inductive loop is also observed in a variety of material platforms that have the common property of a memory effect in current-potential curves due to internal ion motion, associated to polarization within the film, e.g., metal oxides[73] and in $LiNbO_2$ memristors.[74]

The denomination of “negative capacitance” requires clarification, since it is a general feature, widely observed in emerging solar cells and other electronic devices.[62,63,66,72] The responses of Figure 4, and the experimental observations in Figures 8 and 9, contain a positive inductor, not a negative capacitor. However, in the impedance analysis it is useful to plot the capacitance (Eq. 2) vs. the frequency, according to the above definitions $C'(\omega) = \mathrm{Re}[1/i\omega Z(\omega)]$, as shown in Figure 9. In this plot the positive inductor *RL* line certainly displays a negative capacitance effect, Figure 9d, which is the reason to the denomination of “negative capacitance”.

On the other hand the memristors are often associated with a negative resistance.[60] The analysis of Figure 4 is restricted to positive circuit elements while the effect of a NDR will be discussed below in relation with the neuron models.

3.4. Capacitive memristor

The EC in Figure 7B is quite general, based on a broad definition of kinetic equations in the time domain. But it is not the only possible dynamical behaviour of a memristor in the frequency domain. In fact, there is a variety of mechanisms under the denomination of memristive devices that require different characterization techniques.[40,75]

We analyze the famous HP titanium-dioxide memristor,[39,40] where the memristive property is the variation of dopants concentration in a semiconductor film. The model is defined by the following equations including materials constants R_{on}, R_{off}, D, μ

$$u = R_0(w)I \tag{20}$$

$$R_0(w) = (R_{on} - R_{off})\frac{w}{D} + R_{off} \tag{21}$$

$$\frac{dw}{dt} = \mu\frac{R_{on}}{D}I \tag{2}$$

Eq. (21) defines the function $G(w) = {R_0}^{-1}$ in Eq. (8). For the small signal ac perturbation, we obtain Eq. (10) and

$$s\tilde{w} = \mu \frac{R_{on}}{D} \tilde{I} \tag{23}$$

Therefore, the impedance is

$$Z(\omega) = R_0 + \frac{1}{C_1 s} \tag{24}$$

where the capacitor has the value

$$C_1 = \frac{D}{\bar{I} G_w \mu R_{on}} \tag{25}$$

The EC is shown in Figure 7C. The difference with respect to the initial model B is that the relaxation of the internal variable in Eq. (22) depends on current rather than on voltage, which causes a capacitive rather than inductive response for the internal variable. Therefore, there is a contrast between voltage- and current-controlled memristor according to the fundamental EC response. At the present time the generality of such classification is not known, and it appears an important topic for future investigations.

4. Adaptative exponential integrate-and fire model

4.1. Kinetic model

In the integrate-and-fire models the membrane capacitor of the neuron is charged by external stimulus. When the voltage reaches a certain threshold, the capacitor is discharged, producing an action potential and then the voltage is reset to the rest value.

This type of models has the advantage that they can be solved mathematically, and they have been used to analyse the emergent states in networks of neurons. The simplest model is formed by charging an RC circuit and subsequent voltage reset. The dynamics can be enriched by features approaching the more complete multichannel Hodgkin-Huxley model, that will be discussed in the next section. In particular, an action potential produces a refractory period in which the neuron cannot be stimulated. These delays influence the neuron firing patterns. They can be described by an adaptation current that is fed back to the voltage with time constant τ_k and a resistance R_a.[12] These models can successfully emulate spatiotemporal integration of input signals and the firing functions of biological neurons.

Here we analyze the impedance response of the integrate-and-fire Adaptative Exponential model (AdEx)[76-82] that is able to reproduce many electrophysiological features seen in real neurons with a few parameters that have a physiological interpretation. This model neuron has been realized using perovskite memristors.[37]

The voltage in the membrane u changes with time by a conductance function $f(u)$, a resistor R_l and a response time τ_m, with charging capacitance in Eq. (18). The current I

is coupled to an internal adaptation current w that is driven by the departure from the rest potential u_{rest}. The model equations are

$$\tau_m \frac{du}{dt} = f(u) - R_I w + R_I I(t) \tag{26}$$

$$\tau_k \frac{dw}{dt} = \frac{1}{R_a}(u - u_{rest}) - w \tag{27}$$

The model consists of a dynamical system formed by two equations with the general structure of the memristor in Eqs. (16) and (17). The mechanism of adaptation current is the state variable of the memristor. On the other hand, Eqs. (26) and (27) have a direct relation to a number of models for bursting oscillations in electrochemical cells.[83,84]

The function $f(u)$ can be found experimentally from the measurement of neuron discharges.[12] It is $f(u_{rest}) = 0$ and increases rapidly after a threshold voltage θ_{th} that launches an action potential. In particular the adaptative exponential (AdEx) integrate-and-fire model uses the expression[85] shown in Figure 10a

$$f(u) = -(u - u_{rest}) + \Delta_T \exp\left(\frac{u-\theta_{th}}{\Delta_T}\right) \tag{28}$$

where Δ_T is a “sharpness parameter”. The exponential term approximates the operation of sodium channel, that launches the action potential. The model is composed of two currents in parallel, the passive current associated to the function $f(u)$, and the adaptation current w. The Eqs. (26) and (28) establish the subthreshold dynamics of the model. Once the vertical voltage rise is achieved, the spike is obtained by a reset of the voltage $u \rightarrow u_{rest}$ and an increase of the adaptation current $w \rightarrow w + b$.

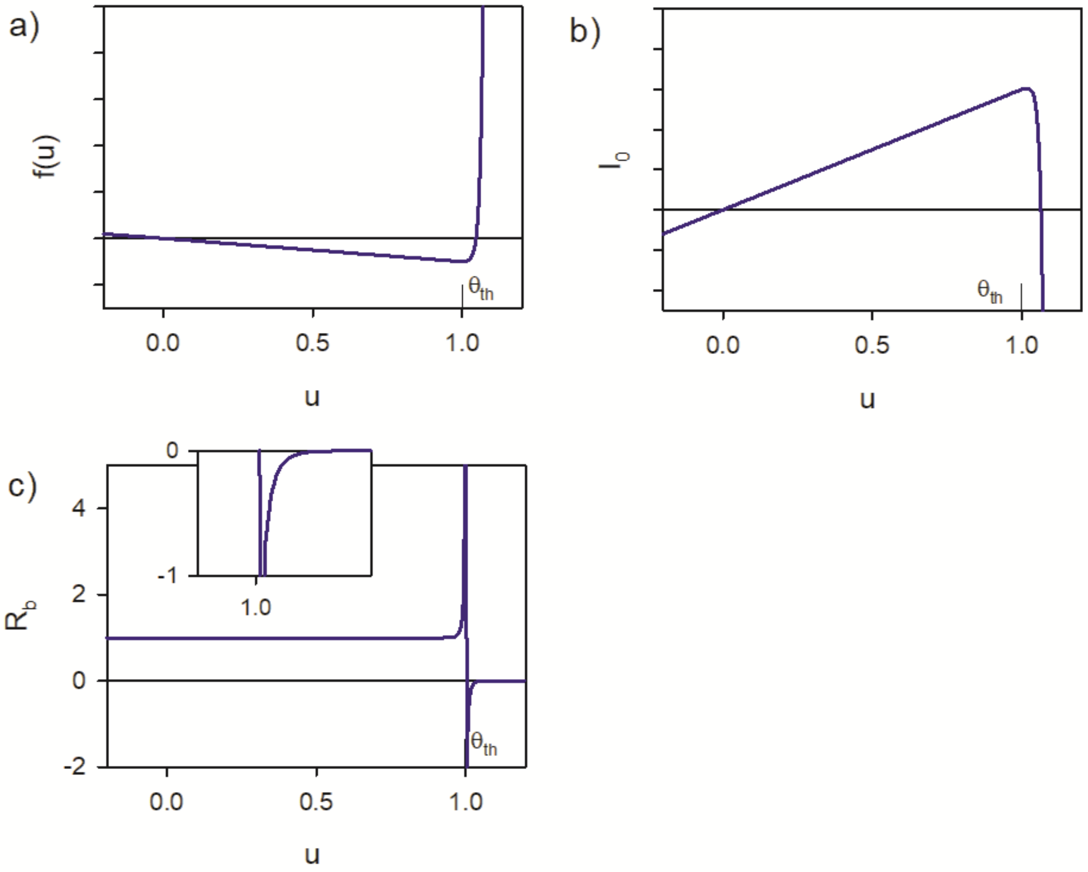

Figure 10. Voltage dependence of quantities in the AdEx model with $u_{rest}= 0$. (a) The function $f(u)$. (b) The stationary current-voltage curve. (c) Resistance R_b, the inset shows the negative values at $u > \theta_{th}$.

The fixed points are obtained setting time-derivatives $\dot{u} = 0$ and $\dot{w} = 0$ at an external current I_0. The steady-state current-voltage corresponds to the set of fixed points:

$$I_0 = \left(\frac{1}{R_a} + \frac{1}{R_I}\right)(u - u_{rest}) - \frac{\Delta_T}{R_I} \exp\left(\frac{u-\theta_{th}}{\Delta_T}\right) \tag{29}$$

The result is shown in Figure 10b. The plot displays a clear NDR feature at $u > \theta_{th}$, corresponding to the initiation of the neuron spike.

4.2. Impedance response

We now calculate the ac impedance response. The small perturbation of Eqs. (26) and (27) at a voltage point $\bar{u}$ gives the equations

$$\tau_m s\tilde{u} = f'\tilde{u} - R_I\widetilde{w} + R_I\tilde{I} \tag{30}$$

$$\tau_k s\widetilde{w} = \frac{1}{R_a}\tilde{u} - \widetilde{w} \tag{31}$$

where

$$f'(\bar{u}) = -1 + \exp\left(\frac{\bar{u}-\theta_{th}}{\Delta_T}\right) \tag{32}$$

The solution to the impedance is given in Eq. (19). The EC parameters have the values

$$R_b(\bar{u}) = -\frac{R_I}{f'} = \frac{R_I}{1-\exp\left(\frac{\bar{u}-\theta_{th}}{\Delta_T}\right)} \tag{33}$$

$$L_a = R_a\tau_k \tag{34}$$

Importantly, according to Eq. (33), the resistance R_b makes a transition from positive to negative values close to $u = \theta_{th}$, which originates the NDR in Figure 10c.

The fixed points of the system are given in Eq. (29). To study their stability, we calculate the Jacobian matrix for a small perturbation around the fixed point at $\bar{u}$:

$$\begin{pmatrix} f'/\tau_m & -R_I/\tau_m \\ 1/(R_a\tau_k) & -1/\tau_k \end{pmatrix} \tag{35}$$

Obtaining the eigenvectors, we find the two necessary and sufficient conditions for stability

$$\lambda_+ + \lambda_- = -\frac{1}{R_bC_m} - \frac{R_a}{L_a} < 0 \tag{36}$$

and

$$\lambda_+\lambda_- = \frac{R_a}{L_aC_m}\frac{1}{R_{dc}} > 0 \tag{37}$$

These can also be expressed, respectively, as

$$\frac{\tau_m}{\tau_k} > f'(\bar{u}) \tag{38}$$

$$\frac{R_I}{R_a} > f'(\bar{u}) \tag{39}$$

The low frequency dc resistance is

$$R_{dc} = \left(\frac{1}{R_a} + \frac{1}{R_b}\right)^{-1} \tag{40}$$

The second condition of stability (39) corresponds to

$$R_{dc} > 0 \tag{41}$$

The impedance model corresponds to the EC in Figure 7B. Since $f' = -1$ for most of the subthreshold region, the stability is warranted by Eqs. (38) and (39) and the impedance spectra correspond to those in Figure 4.

Let us analyze in more detail the inductive feature in Figure 4a. The resistance at the intercept $Z'' = 0$ has the value

$$R_{Z''=0} = \frac{R_b}{1+R_aR_bC_m/L_a} = \frac{R_b}{1+\frac{R_b\tau_m}{R_I\,\tau_k}} \tag{42}$$

The spectrum in Figure 4a reflects the two-step relaxation in the model. Normally u is the fast variable and w shows a slow relaxation associated to the memory effect. Then assuming $\tau_m \ll \tau_k$, the impedance response of the system shows a fast relaxation in the high frequency arc and the real part of the impedance reaches R_b. Then, the slow variable sets in and reduces the dc resistance to the lower R_{dc} value, as commented previously. More rigorously, the condition that $R_{Z''=0} > R_{dc}$ is given by

$$\frac{R_I}{R_a} > \frac{\tau_m}{\tau_k} \tag{43}$$

which corresponds to the condition expressed in figure 4 for the AdExp model specifically. This expression indicates the transition from Figure 4a to Figure 4b when the negative capacitance feature in the fourth quadrant disappears. The condition (43) also indicates the appearance of a Hopf bifurcation when the current is increased, whereas in the opposite case the system undergoes a saddle-node bifurcation.[77] The impedance spectra in the transition zone are shown in the experimental examples of Figure 9.

4.3. The impedance spectra for negative resistance values

The classification of characteristic impedance spectra for negative R_b has been shown in Figure 5. The condition in Eq. (43) also indicates which of the conditions of stability (38) and (39) is broken first. If (43) is satisfied, then there is a region where the two parallel currents compete, being R_b negative but R_{dc} still positive, in the potential range determined by the condition

$$\frac{R_I}{R_a} > f'(\bar{u}) = -\frac{R_I}{R_b} > \frac{\tau_m}{\tau_k} \tag{44}$$

This region produces the impedance pattern of Figure 5 defined before as a “hidden negative impedance”.[31] Here the complex $Z(\omega)$ encircles the origin and the imaginary part of the impedance has a zero value at finite frequency of negative real part. This is a signal of the Hopf instability, as mentioned earlier.

Figure 5 shows the impedance spectra in the presence of a true NDR. These patterns are well documented in the literature of electrochemical oscillations, in the case of oscillations induced by a Hopf bifurcation under potentiostatic control.[86,87] Different examples of the spectra for formaldehyde oxidation are shown in Figure 11. These impedance patterns are also very typical for electrochemical passivation and corrosion.[88,89]

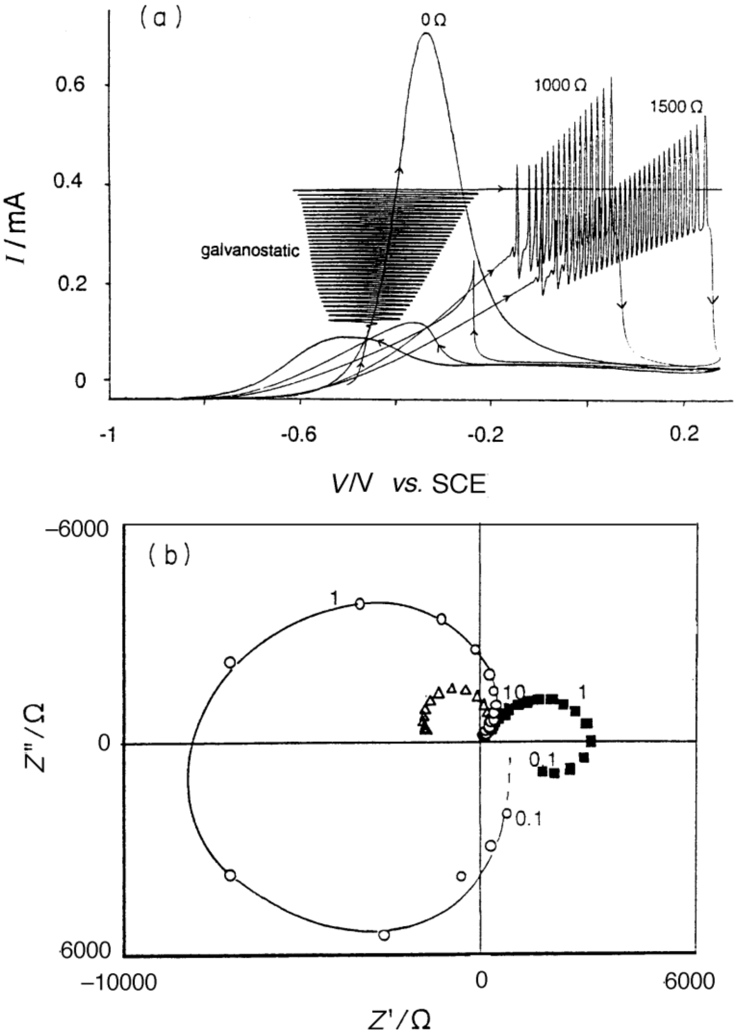

Figure 11. a) Voltammogram of 0.1 M HCHO in 0.1 M NaOH for a 0, 1000 and 1500 Ω external resistance (internal cell resistance ca. 95 Ω). Scan rate 10 mV s^{-1}, 3000 rev min^{-1}. Amperogram taken at 0.01 mA s^{-1}. (b) Impedance diagrams taken at -0.50 V (■), -0.45 V (○), -0.35 V (Δ). Indicated frequencies in Hz. Reproduced from [87].

Figure 12 indicates the impedance spectrum when the *RL* elements are both negative. This is not a case that emanates from the AdEx model, but it is also interesting since it occurs naturally in the sodium channel of the Hodgkin-Huxley model discussed below.

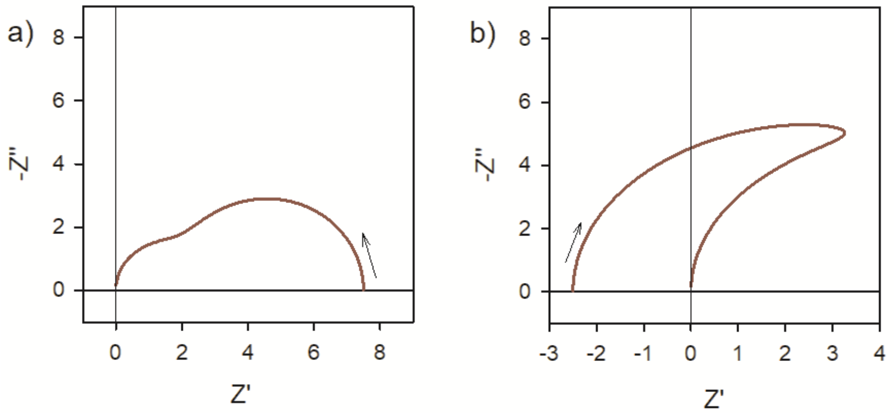

Figure 12. Complex plane impedance spectra of the AdEx model, $R_a < 0$ and $L_a < 0$. (a) R_I = 1, R_a= -5, R_b = 3, R_{dc} = 7.5, τ_m= 10, τ_k= 100, L_a= -500. (b) R_I = 10, R_a= -2, R_b = 10, R_{dc} = -2.5, τ_m= 10, τ_k= 100, L_a= -200. The arrow indicates the direction of increasing frequency.

The transient response to a current step in the time domain is represented in Figure 13. Figure 13a shows a damped oscillation, while Figure 13b corresponding to the hidden negative resistance shows a periodic amplification correspondent to negative damping.

A complete study of the oscillations, spiking dynamics and bifurcations of the AdEx model depending on the external current I is presented by Touboul et al.[77]

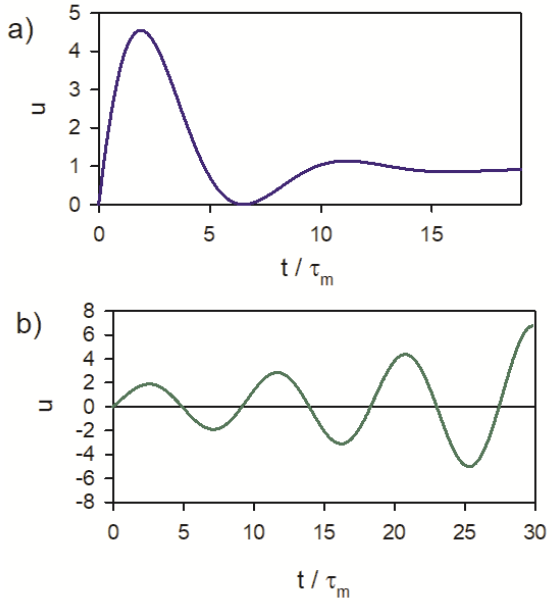

Figure 13. Transient voltage in the AdEx model after a small perturbation constant current onset at $t = 0$. (a) R_I = 5, R_a= 1, R_b = 10, τ_m= 10, τ_k= 100. (b) R_I = 1, R_a= 0.2, R_b = -5, R_{dc} = 0.2083, τ_m= 10, τ_k= 100.

5. Hodgkin-Huxley squid giant axon model

5.1. Kinetic model

Finally, we aim to calculate the impedance response from the Hodgkin-Huxley dynamical model for the squid giant axon membrane.[11] This is a landmark model that is extremely accurate for describing neuron dynamics. A development of the small perturbation ac model was presented by Chua and coworkers in order to investigate the stability conditions.[35,36] Here we aim to understand the main impedance responses and provide an interpretation based on the simpler models that have been analyzed earlier in this paper, namely the memristor and the adaptative integrate-and-fire neuron.

The original H-H model follows different current and voltage references from those usually adopted in the literature.[90,91] Therefore, we rewrite the H-H equations such that they comply with this convention, i.e., current direction from inside to outside the membrane and voltage polarity positive inside and negative outside, as shown in Figure 14a. Moreover, we consider the membrane potential as it is, and we do not use the original transformation, where the origin is taken at the resting potential of the membrane ($V_M = V_r$).

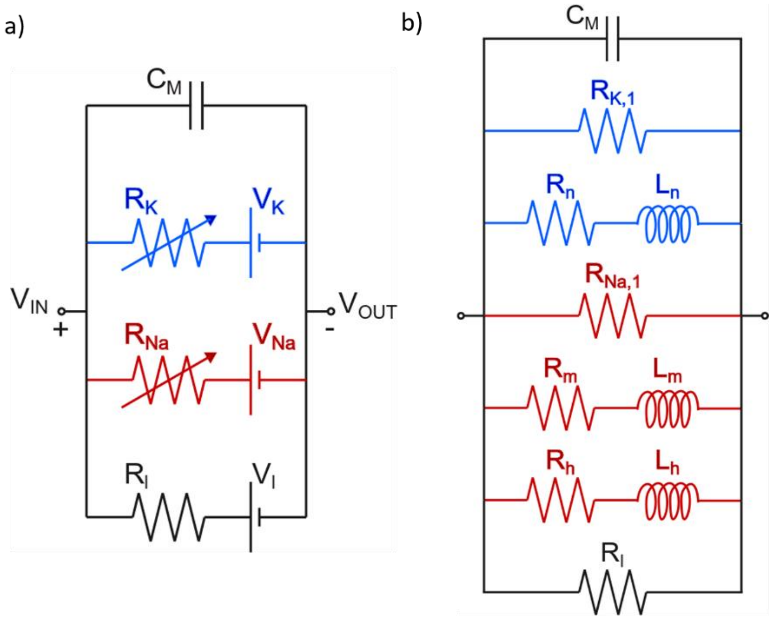

Figure 14. a) Hodgkin-Huxley electrical model for the squid giant axon membrane consisting of variable resistances in the ion channels as defined in the original publication. b) Equivalent circuit for the Hodgkin-Huxley model for small ac voltage perturbations. The potassium channel components are indicated in blue, and the sodium elements in red.

The electrical circuit of the membrane, shown in Figure 14a, has four different branches that correspond to the membrane capacitance, the potassium ions channel, the sodium ions channel, and the leakage current, respectively. As noted in Figure 14a, the resistances across the potassium (R_K) and sodium (R_{Na}) channels are not constant, but they depend both on time and voltage, reflecting the complex dynamics in response to external inputs. The model provides complete kinetic equations for the different channels, therefore we will be able to develop the small ac EC elements at a fixed point, using the same method applied in the previous examples.

The current through the membrane can be written as the addition of the four contributions in Figure 14a

$$I_M = I_C + I_K + I_{Na} + I_l \tag{45}$$

The currents obey the expressions:

$$I_C = C_M \frac{dV_M}{dt} \tag{46}$$

$$I_K = \frac{1}{R_K}(V_M - V_K) \tag{47}$$

$$I_{Na} = \frac{1}{R_{Na}}(V_M - V_{Na}) \tag{48}$$

$$I_l = \frac{1}{R_l}(V_M - V_l) \tag{49}$$

Here, the membrane voltage V_M is defined as

$$V_M = V_{IN} - V_{OUT} \tag{50}$$

and the other voltages follow the polarity indicated in Figure 14a, and they have the values $V_K = -77$ mV, $V_{Na} = 50$ mV and $V_l = -54.387$ mV. Each of these voltages relate to the membrane voltages that cancel the current in each channel. We consider a resting potential of $V_r = -65$ mV, which corresponds to the resting potential at a temperature of $T = 6.3$ °C.[11] The resting potential is the voltage at which there is no current through the membrane. The membrane capacitance C_M has a value of 1 μFcm^{-2} and the leakage resistance is 3.33 kΩcm^2.

The potassium resistance is described by the following expression

$$\frac{1}{R_K} = \frac{1}{R_{K0}} n^4 \tag{51}$$

where $R_{K0} = 27.78$ Ωcm^2 is the minimum value of the resistance and n is a dimensionless potassium gate-activation variable that takes values from 0 to 1, and satisfies the following equation:

$$\frac{dn}{dt} = \alpha_n(1 - n) - \beta_n n \tag{52}$$

Here, the transfer rate coefficients α_n and β_n are time independent and voltage dependent by:

$$\alpha_n = \frac{0.01(10 - V')}{e^{\frac{10 - V'}{10}} - 1} \tag{53}$$

$$\beta_n = \frac{0.125}{e^{\frac{V'}{80}}} \tag{54}$$

where α_n and β_n are in ms^{-1} and $V' = V_M - V_r$ is in mV.

The sodium resistance is described by a similar expression:

$$\frac{1}{R_{Na}} = \frac{1}{R_{Na0}} m^3 h \tag{55}$$

In the same way as before, $R_{Na0} = 8.33\ \Omega\text{cm}^2$ is the minimum value of the sodium resistance. However, the sodium channel has two gate-activation variables m and h. They both are dimensionless and take values from 0 to 1, and similarly to the variable n, they are described by the equations:

$$\frac{dm}{dt} = \alpha_m(1-m) - \beta_m m \tag{56}$$

$$\frac{dh}{dt} = \alpha_h(1-h) - \beta_h h \tag{57}$$

Again, α_m and β_m are time independent and voltage dependent. Their voltage dependence is given by:

$$\alpha_m = \frac{0.1(25-V')}{e^{\frac{25-V'}{10}}-1} \tag{58}$$

$$\beta_m = \frac{4}{e^{\frac{V'}{18}}} \tag{59}$$

α_h and β_h are voltage dependent, too, by the equations:

$$\alpha_h = \frac{0.07}{e^{\frac{V'}{20}}} \tag{60}$$

$$\beta_h = \frac{1}{e^{\frac{30-V'}{10}}+1} \tag{61}$$

All the transfer rate coefficients are in ms^{-1} and $V' = V_M - V_r$ is in mV.

We can rewrite the equations (47) and (48) of the currents across the two ion channels as

$$I_K = \frac{1}{R_{K0}} n^4 (V_M - V_K) \tag{62}$$

$$I_{Na} = \frac{1}{R_{Na0}} m^3 h (V_M - V_{Na}) \tag{63}$$

5.2. Impedance response

From these equations we can calculate the ac impedance response of the H-H model across each branch. The small perturbation and Laplace transform of equations (46), (62), (63) and (49) give the equations:

$$\tilde{I}_C = sC_M \tilde{V}_M \tag{64}$$

$$\tilde{I}_K = \frac{1}{R_{K0}} 4\bar{n}^3 (\bar{V}_M - V_K)\tilde{n} + \frac{1}{R_{K0}} \bar{n}^4 \tilde{V}_M \tag{65}$$

$$\tilde{I}_{Na} = \frac{1}{R_{Na0}} 3\bar{m}^2\bar{h}(\bar{V}_M - V_{Na})\tilde{m} + \frac{1}{R_{Na0}}\bar{m}^3(\bar{V}_M - V_{Na})\tilde{h} + \frac{1}{R_{Na0}}\bar{m}^3\bar{h}\tilde{V}_M \tag{66}$$

$$\tilde{I}_l = \frac{1}{R_l}\tilde{V}_M \tag{67}$$

Here, in equations (65) and (66), the perturbed variables $\tilde{n}$, $\tilde{m}$ and $\tilde{h}$ appear. We can calculate them from the small perturbation and Laplace transform from equations (52), (56) and (57):

$$s\tilde{n} = \left[\frac{\partial\bar{\alpha}_n}{\partial V_M}(1-\bar{n}) - \frac{\partial\bar{\beta}_n}{\partial V_M}\bar{n}\right]\tilde{V}_M - (\bar{\alpha}_n + \bar{\beta}_n)\tilde{n} \tag{68}$$

$$s\tilde{m} = \left[\frac{\partial\bar{\alpha}_m}{\partial V_M}(1-\bar{m}) - \frac{\partial\bar{\beta}_m}{\partial V_M}\bar{m}\right]\tilde{V}_M - (\bar{\alpha}_m + \bar{\beta}_m)\tilde{m} \tag{69}$$

$$s\tilde{h} = \left[\frac{\partial\bar{\alpha}_h}{\partial V_M}(1-\bar{h}) - \frac{\partial\bar{\beta}_h}{\partial V_M}\bar{h}\right]\tilde{V}_M - (\bar{\alpha}_h + \bar{\beta}_h)\tilde{h} \tag{70}$$

From the combination of equations (64-70), we derive the impedance given by

$$Z = \frac{\tilde{V}_M}{\tilde{I}_M} = \frac{\tilde{V}_M}{\tilde{I}_C + \tilde{I}_K + \tilde{I}_{Na} + \tilde{I}_l} \tag{71}$$

Rearranging all the terms obtained, we can get an expression for impedance with the following elements:

$$Z = \frac{\tilde{V}_M}{\tilde{I}_M} = \left[sC_M + \frac{1}{R_{K,1}} + \frac{1}{R_n + sL_n} + \frac{1}{R_{Na,1}} + \frac{1}{R_m + sL_m} + \frac{1}{R_h + sL_h} + \frac{1}{R_l}\right]^{-1} \tag{72}$$

The EC generated by this impedance is shown in Figure 14b, and the values of the voltage-dependent elements are detailed as follows:

$$R_{K,1}(\bar{V}_M) = \frac{R_{K0}}{\bar{n}^4} \tag{73}$$

$$R_n(\bar{V}_M) = \frac{R_{K0}}{4\bar{n}^3(\bar{V}_M - V_K)\tau_n\left[\frac{\partial\bar{\alpha}_n}{\partial V_M}(1-\bar{n}) - \frac{\partial\bar{\beta}_n}{\partial V_M}\bar{n}\right]} \tag{74}$$

$$L_n(\bar{V}_M) = R_n\tau_n \tag{75}$$

$$R_{Na,1}(\bar{V}_M) = \frac{R_{Na0}}{\bar{m}^3\bar{h}} \tag{76}$$

$$R_m(\bar{V}_M) = \frac{R_{Na0}}{3\bar{m}^2\bar{h}(\bar{V}_M - V_{Na})\tau_m\left[\frac{\partial\bar{\alpha}_m}{\partial V_M}(1-\bar{m}) - \frac{\partial\bar{\beta}_m}{\partial V_M}\bar{m}\right]} \tag{77}$$

$$L_m(\bar{V}_M) = R_m\tau_m \tag{78}$$

$$R_h(\bar{V}_M) = \frac{R_{Na0}}{\bar{m}^3(\bar{V}_M - V_{Na})\tau_h\left[\frac{\partial\bar{\alpha}_h}{\partial V_M}(1-\bar{h}) - \frac{\partial\bar{\beta}_h}{\partial V_M}\bar{h}\right]} \tag{79}$$

$$L_h(\bar{V}_M) = R_h\tau_h \tag{80}$$

The different relaxation time constants τ_i of each activation-gate variable are defined as

$$\tau_i = \frac{1}{\alpha_i + \beta_i} \tag{81}$$

These results correspond to those obtained by Chua et al.[35] with a different voltage reference.

5.3. Interpretation of the impedance spectra

We aim to analyse impedance spectra in the region where the real part of the impedance takes negative values, since this is the requirement for inducing oscillations and spiking. This occurs between $V_M = -42.99$ mV and $V_M = -60.25$ mV. In Figure 15, we show a set of impedance complex plots of the full model of Figure 14b for representative voltage values above this range (Figure 15a,b), in this range (Figure 15b,c,d) and below it (Figure 15d).

The negative value of the real part of the impedance is clearly observed at frequencies different from zero, it is therefore a “hidden negative impedance”. The values close to the voltage range limit have only a small region in the negative area, while the intermediate values have most of the spectrum at the negative part, Figure 15c.

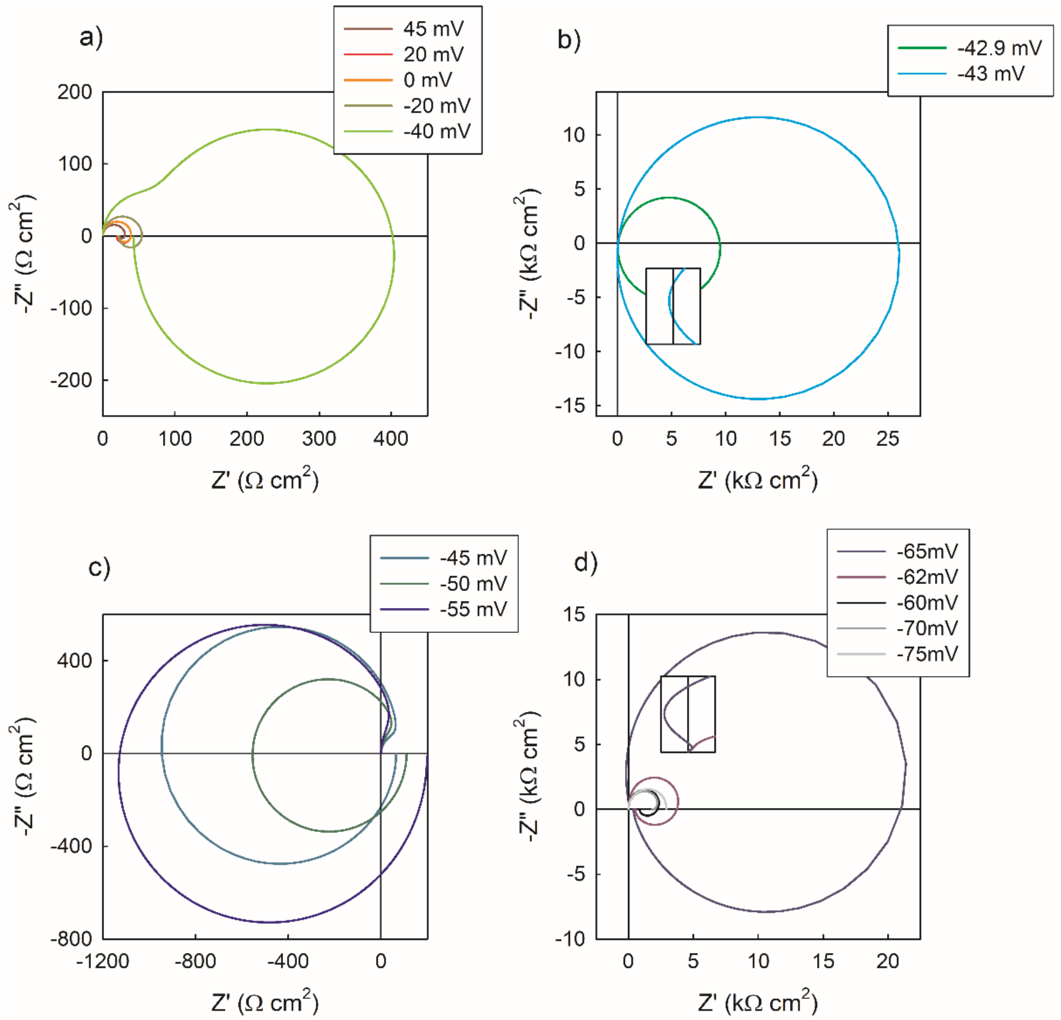

Figure 15. Impedance complex plane plots for voltages a) above the upper limit of the negative impedance region, b) around the upper limit $V_M = -42.99\, mV$, c) in the negative impedance region and d) around the lower limit $V_M = -60.25\, mV$.

In order to better understand the EC and the wide diversity of characteristic impedance spectra obtained for the Hodgkin-Huxley model, and compare it with other systems with similar ECs, we now analyze the impedance response of the individual K and Na channels that compose the model.

We first look at the spectra generated by the potassium channel with the constant elements C_M and R_l. The partial EC is represented in Figure 16a, and it is equivalent to the general memristor EC previously described in Figure 7B. Figures 16b and 16c show the values of the circuit elements generated by the potassium channel for the voltage range spanning from V_K to V_{Na}. The graphs show that the resistances have relatively low values compared to the leakage resistance (3.33 kΩ) for voltages above the resting potential V_r. Below this value, both resistances start to increase until they take huge values. The same happens in the case of the inductor in Figure 16c.

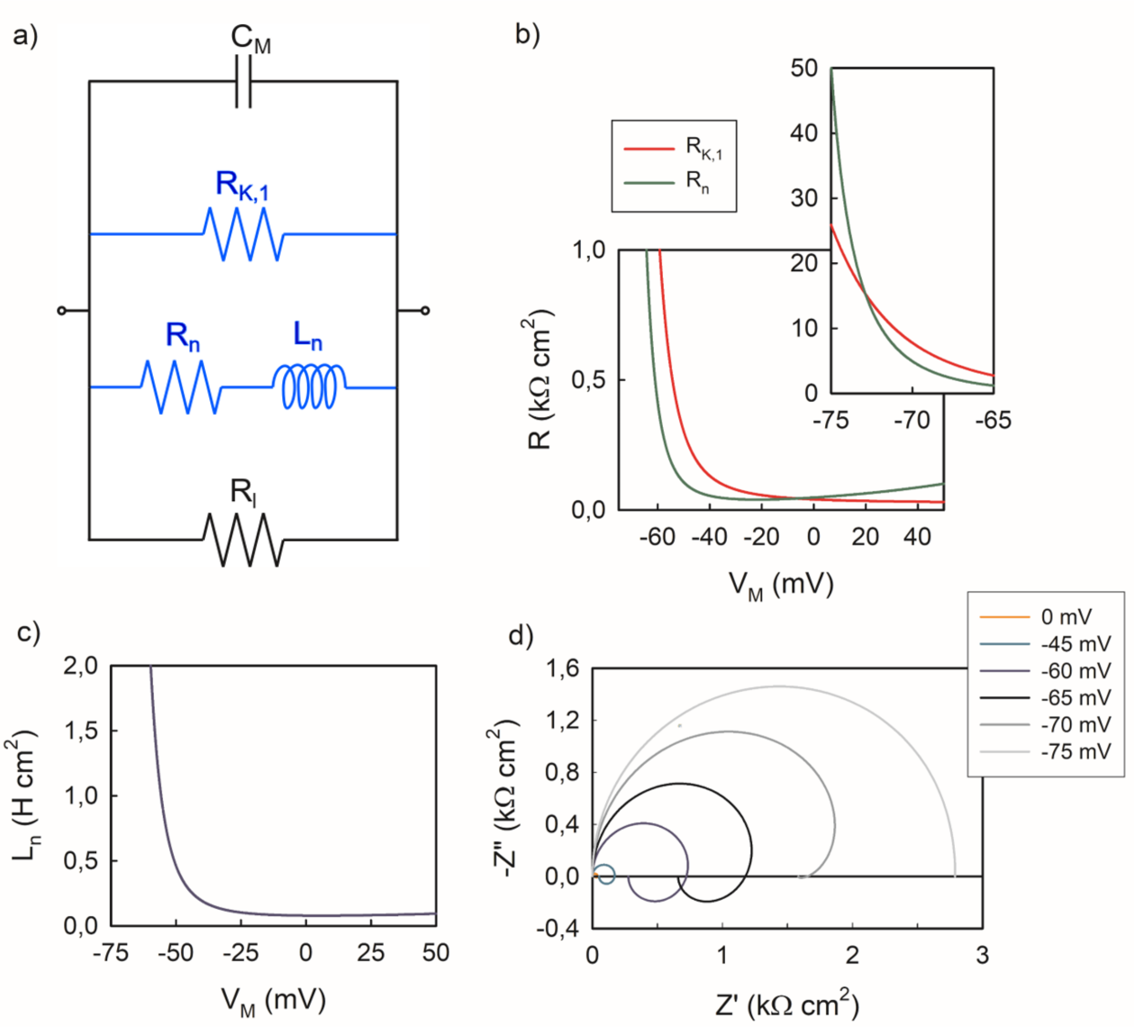

Figure 16. Impedance details of the K channel. (a) EC used for (d). (b) and (c) values of the elements for the range of membrane voltages. (d) impedance complex plane plot for different values.

In Figure 16d, we can see the impedance complex plane plots for a variety of membrane voltages. The spectra generated by this circuit and the evolution of these elements generally shows an arc at the first quadrant at high frequency and another arc in the fourth quadrant at low frequency. This behaviour has been described above in Figure 4. The arcs are relatively small at voltages above $V_M = -20$ mV, where the values of all the potassium channel resistances and inductor have small values. Below these values, the arcs start to increase, until the fourth quadrant arc disappears, and the spectrum is dominated by the constant elements. This means that the potassium channel closes as we get closer to the voltage V_K.

If we calculate the Jacobian and apply the stability conditions in the same way we did before but for this EC, we get the following conditions:

$$-\left(\frac{1}{R_{k,1}}+\frac{1}{R_l}\right) < \frac{C_M}{\tau_n} \tag{82}$$

$$-\left(\frac{1}{R_{k,1}}+\frac{1}{R_l}\right) < \frac{1}{R_n} \tag{83}$$

Moreover, if we apply the condition $R_{Z''=0} > R_{dc}$ for the appearance of inductive loops, we get:

$$-\left(\frac{1}{R_{k,1}}+\frac{1}{R_l}\right) < \frac{C_M}{\tau_n} < \frac{1}{R_n} \tag{84}$$

Since the values of all these elements and parameters are fixed for any given membrane voltage, we can predict the appearance of the inductive loops, as well as the stable voltage values. For this aim, we plot the three factors in Figure 17, to find those voltages. In this Figure, we have defined the resistance $R_c^{-1} = R_{k,1}^{-1} + R_l^{-1}$.

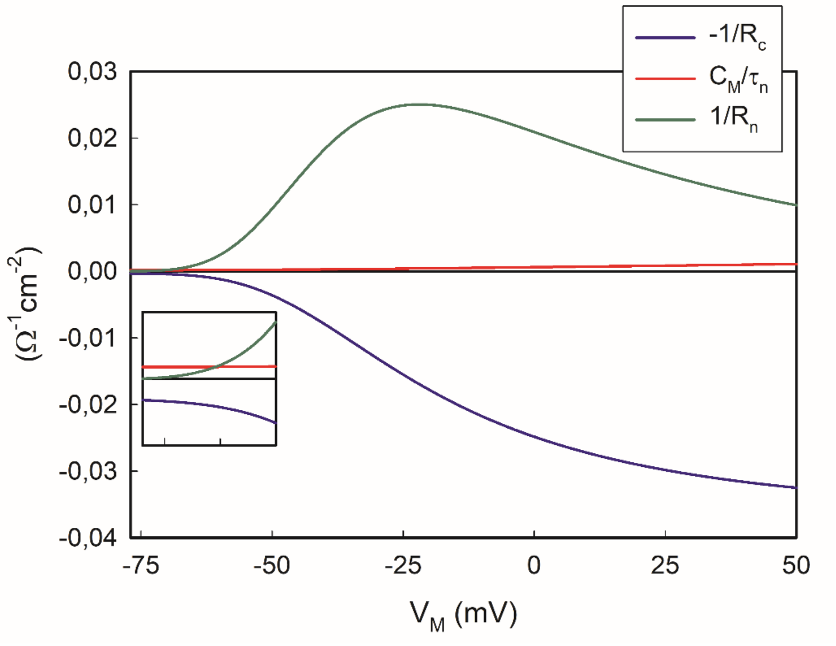

Figure 17. Factors for the conditions of stability and inductive loops appearance.

From Figure 17, we can conclude that the potassium channel circuit is stable in the whole range of voltages. Moreover, we see a wide range of voltages in which the inductive loop will appear, and we can estimate the voltage where it disappears. This is below a voltage around $V_M = -70$ mV, which agrees with the spectra plotted in Figure 16d.

Looking at the sodium channel, we build in Figure 18a a partial EC including the elements of the membrane, therefore, we can again see when the channel closes and these elements dominate. As we can see, this channel is richer in the number of elements. From Figures 18b and 18c, we find elements that take negative values. These are the elements R_m and L_m and they make the spectra generated from this channel even richer, with spectra appearing in any of the four quadrants of the complex plane representation, as previously demonstrated in Section 2.3.

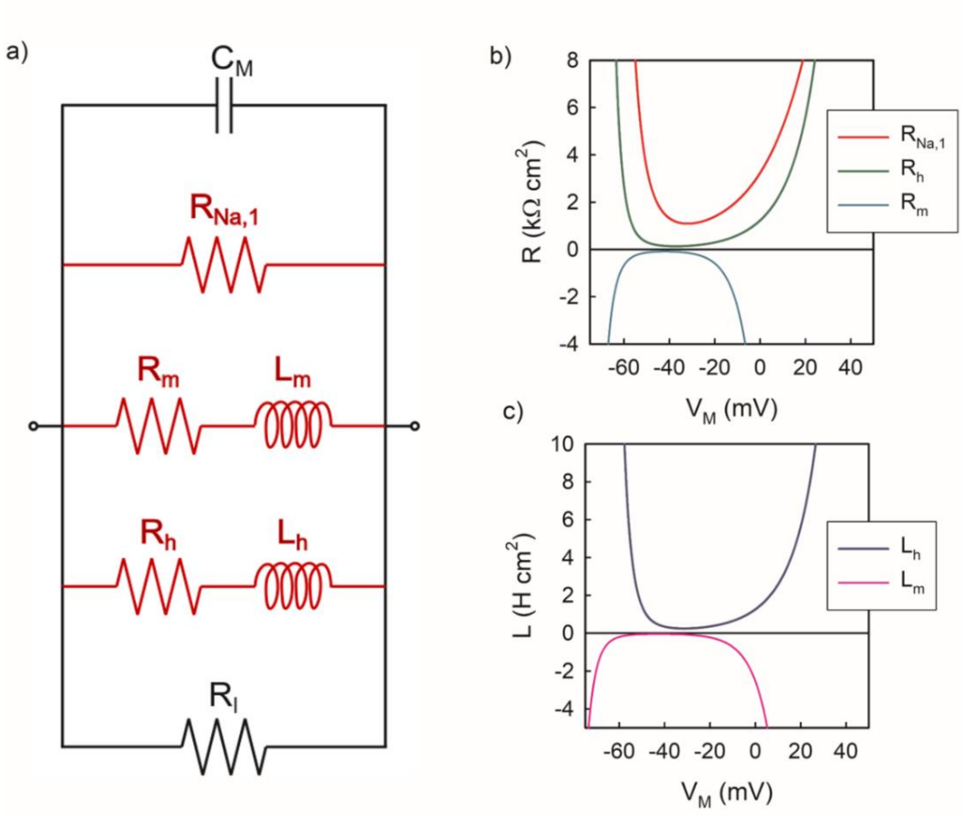

Figure 18. Impedance details of the Na channel. (a) EC used of the Na channel. (b) and (c) values of the resistances and inductors for the range of membrane voltages, respectively.

As in the case of the potassium channel, the elements have low values in a certain range of voltages, while they take huge values outside this range. This is clearly seen in Figures

18b and 18c and it relates with the fact that at voltages $20\ \text{mV} < V_M < -65\ \text{mV}$ the sodium channel is mainly closed, and we again see a single arc corresponding to the constant membrane elements in Figure 19. However, inside this range we again see the memristive inductive loop into the fourth quadrant at $V_M = -20\ \text{mV}$. More interestingly, we see the hidden negative resistance at $V_M = -30\ \text{mV}$, and a clear negative resistance from approximately $V_M = -40\ \text{mV}$ to $V_M = -65\ \text{mV}$. Therefore, it looks evident that the channel causing the negative impedance in the whole membrane is the sodium channel. However, the full membrane will not show a negative impedance at zero frequency.

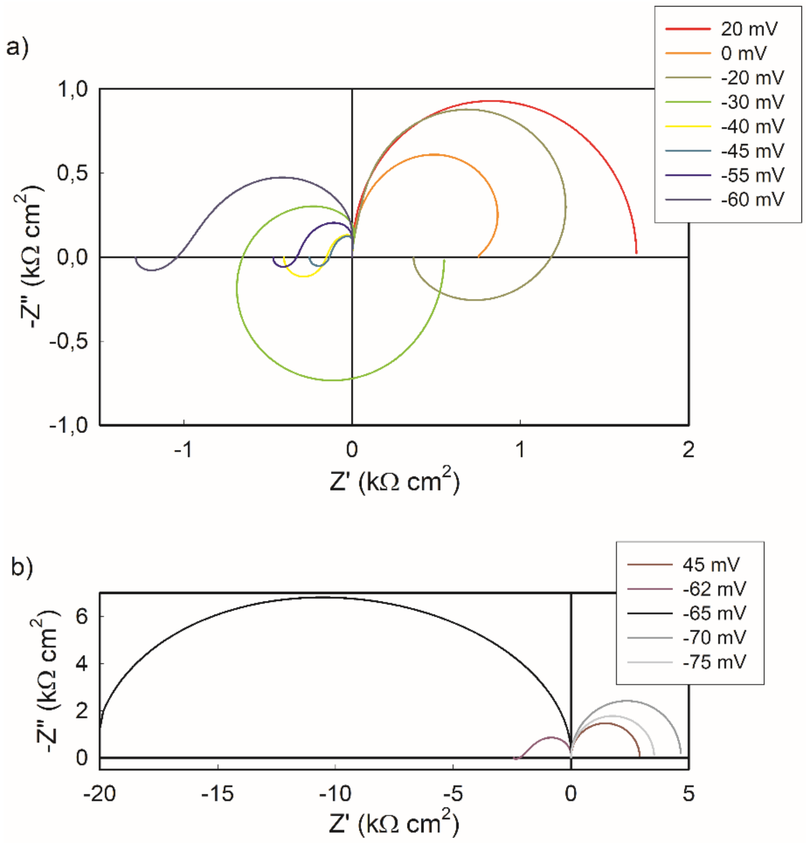

Figure 19. Impedance complex plane plots for the sodium channel EC. (a) is for spectra with smaller impedance values and (b) is for spectra with bigger impedance values.

6. Conclusion

The method we have developed in this paper consists on the determination of the small perturbation ac IS response of highly nonlinear systems, related to memristors and neuromorphic response, starting from the time domain constitutive equations of each model. We showed the connection of impedance response and the shape of the spectra to the physical interpretation of memory effects and stability, following previous insights in stability theory and electrochemical oscillations.

Firstly, we presented a frequency domain analysis of memristors. We showed that the memristor can be decomposed into a simple equivalent circuit, and it cannot be regarded as an additional fundamental element for small signal response. This is because the mechanism of memory is well represented by a resistor-inductor line. The basic structure of the impedance model is obtained across different material platforms and independent fields of study. There is possibly a universal behaviour related to the suggested kinetic memory effect that needs further investigation. Nevertheless, the model is not unique to describe memristor systems. There is indeed a very broad type of responses under the label of memristive systems, based on different mechanisms and physical effects.

The impedance response of the adaptative exponential integrate-and-fire model for the neuron membrane shows a similar response to that of the memristor, thus confirming them as good candidates for neuromorphic computations. We have made a classification of the spectra generated by this model, and we have established the required conditions for the stability of the impedance response. A variety of criteria consisting of relations among the model parameters have been given in order to clarify which conditions generate each kind of spectra.

The same has been made for the Hodgkin-Huxley model for the squid giant axon. We made an extended calculation of the full impedance model, showing the full equivalent circuit that governs the operation of these membranes. We have presented the spectra generated by this model for a wide range of voltages, finding a wide variety of shapes, including the hidden negative resistance. With respect to the previously described simple models, this model has the additional complexity of consisting of different channels that cause positive and negative feedback loops. To obtain better insight about the concerted action that produces the diverse impedance spectra responses, we investigated separately the individual ion channels responses. Interestingly, we have found that the potassium channel fulfills the stability conditions in all the voltage range and the condition for inductive loops is satisfied. However, the sodium channel is more complex, and its equivalent circuit includes a branch with negative elements (a resistance and an inductor) that produce all kind of spectra going through the four quadrants. This feature is responsible for the positive feedback that causes depolarization including the hidden negative resistance in the full model.

In summary we have suggested a method to analyze the response of a required dynamical system in the frequency domain as a tool to construct material systems with a similar functionality.

Acknowledgment

We thank Generalitat Valenciana for the project PROMETEO/2020/028. A.B. acknowledges FPI studentship funding from Ministerio de Ciencia e Innovación of Spain (BES-2017-080351).

References

(1) Basheer, I. A.; Hajmeer, M. Artificial neural networks: fundamentals, computing, design, and application, *J.Microbiol. Meth.* **2000**, *43*, 3-31.

(2) Indiveri, G.; Linares-Barranco, B.; Legenstein, R.; Deligeorgis, G.; Prodromakis, T. Integration of nanoscale memristor synapses in neuromorphic computing architectures, *Nanotech.* **2013**, *24*, 384010.

(3) Tang, J.; Yuan, F.; Shen, X.; Wang, Z.; Rao, M.; He, Y.; Sun, Y.; Li, X.; Zhang, W.; Li, Y.; Gao, B.; Qian, H.; Bi, G.; Song, S.; Yang, J. J.; Wu, H. Bridging Biological and Artificial Neural Networks with Emerging Neuromorphic Devices: Fundamentals, Progress, and Challenges, *Adv. Mater.* **2019**, *31*, 1902761.

(4) Tuchman, Y.; Mangoma, T. N.; Gkoupidenis, P.; van de Burgt, Y.; John, R. A.; Mathews, N.; Shaheen, S. E.; Daly, R.; Malliaras, G. G.; Salleo, A. Organic neuromorphic devices: Past, present, and future challenges, *MRS Bulletin* **2020**, *45*, 619-630.

(5) Mehonic, A.; Kenyon, A. J. Emulating the Electrical Activity of the Neuron Using a Silicon Oxide RRAM Cell, *Front. Neurosc.* **2016**, *10*.

(6) Zhang, Y.; Wang, Z.; Zhu, J.; Yang, Y.; Rao, M.; Song, W.; Zhuo, Y.; Zhang, X.; Cui, M.; Shen, L.; Huang, R.; Yang, J. J. Brain-inspired computing with memristors: Challenges in devices, circuits, and systems, *Appl. Phys. Rev.* **2020**, *7*, 011308.

(7) Burr, G. W.; Shelby, R. M.; Sebastian, A.; Kim, S.; Kim, S.; Sidler, S.; Virwani, K.; Ishii, M.; Narayanan, P.; Fumarola, A.; Sanches, L. L.; Boybat, I.; Le Gallo, M.; Moon, K.; Woo, J.; Hwang, H.; Leblebici, Y. Neuromorphic computing using non-volatile memory, *Adv. Phys.: X* **2017**, *2,* 89-124.

(8) Zhang, X.; Zhuo, Y.; Luo, Q.; Wu, Z.; Midya, R.; Wang, Z.; Song, W.; Wang, R.; Upadhyay, N. K.; Fang, Y.; Kiani, F.; Rao, M.; Yang, Y.; Xia, Q.; Liu, Q.; Liu, M.; Yang, J. J. An artificial spiking afferent nerve based on Mott memristors for neurorobotics, *Nat. Commun.* **2020**, *11*, 51.

(9) Zhang, X.; Wang, W.; Liu, Q.; Zhao, X.; Wei, J.; Cao, R.; Yao, Z.; Zhu, X.; Zhang, F.; Lv, H.; Long, S.; Liu, M. An Artificial Neuron Based on a Threshold Switching Memristor, *IEEE Electron Device Letters* **2018**, *39*, 308-311.

(10) Kim, S.; Roe, D. G.; Choi, Y. Y.; Woo, H.; Park, J.; Lee, J. I.; Choi, Y.; Jo, S. B.; Kang, M. S.; Song, Y. J.; Jeong, S.; Cho, J. H. Artificial stimulus-response system capable of conscious response, *Sci. Adv.* **2021**, *7*, eabe3996.

(11) Hodgkin, A. L.; Huxley, A. F. A quantitative description of membrane current and its application to conduction and excitation in nerve, *J Physiol* **1952**, *117*, 500-544.

(12) Gerstner, W.; Kistler, W. M.; Naud, R.; Paninski, L. *Neuronal Dynamics. From single neurons to networks and models of cognition*; Cambridge University Press, 2014.

(13) Burkitt, A. N. A Review of the Integrate-and-fire Neuron Model: I. Homogeneous Synaptic Input, *Biol. Cybern.* **2006**, *95*, 1-19.

(14) Pickett, M. D.; Medeiros-Ribeiro, G.; Williams, R. S. A scalable neuristor built with Mott memristors, *Nat. Mater.* **2013**, *12*, 114-117.

(15) Bredar, A. R. C.; Chown, A. L.; Burton, A. R.; Farnum, B. H. Electrochemical Impedance Spectroscopy of Metal Oxide Electrodes for Energy Applications, *ACS Appl. Ener. Mater.* **2020**, *3*, 66-98.

(16) von Hauff, E. Impedance Spectroscopy for Emerging Photovoltaics, *J. Phys. Chem. C* **2019**, *123*, 11329-11346.

(17) Fabregat-Santiago, F.; Garcia-Belmonte, G.; Mora-Seró, I.; Bisquert, J. Characterization of nanostructured hybrid and organic solar cells by impedance spectroscopy, *Phys. Chem. Chem. Phys.* **2011**, *13*, 9083–9118.

(18) Lopez-Varo, P.; Jiménez-Tejada, J. A.; García-Rosell, M.; Ravishankar, S.; Garcia-Belmonte, G.; Bisquert, J.; Almora, O. Device Physics of Hybrid Perovskite Solar cells: Theory and Experiment, *Adv. Energy Mater.* **2018**, 1702772.

(19) Wang, H.; Guerrero, A.; Bou, A.; Al-Mayouf, A. M.; Bisquert, J. Kinetic and material properties of interfaces governing slow response and long timescale phenomena in perovskite solar cells, *Energy Environ. Sci.* **2019**, *12,* 2054-2079.

(20) Johnston, M. B.; Herz, L. M. Hybrid Perovskites for Photovoltaics: Charge-Carrier Recombination, Diffusion, and Radiative Efficiencies, *Acc. Chem.Res.* **2016**, *49*, 146-154.

(21) Grimnes, S.; Martinsen, O. G. *Bioimpedance and Bioelectricity Basics, 3rd ed.*; Academic Press, 2015.

(22) Stupin, D. D.; Kuzina, E. A.; Abelit, A. A.; Emelyanov, A. K.; Nikolaev, D. M.; Ryazantsev, M. N.; Koniakhin, S. V.; Dubina, M. V. Bioimpedance Spectroscopy: Basics and Applications, *ACS Biomat. Sci. Eng.* **2021**, 10.1021/acsbiomaterials.1020c01570.

(23) Xu, Y.; Xie, X.; Duan, Y.; Wang, L.; Cheng, Z.; Cheng, J. A review of impedance measurements of whole cells, *Biosen. Bioel.* **2016**, *77*, 824-836.

(24) Spencer, D. C.; Paton, T. F.; Mulroney, K. T.; Inglis, T. J. J.; Sutton, J. M.; Morgan, H. A fast impedance-based antimicrobial susceptibility test, *Nat. Commun.* **2020**, *11*, 5328.

(25) Zou, Y.; Guo, Z. A review of electrical impedance techniques for breast cancer detection, *Med. Eng. Phys.* **2003**, *25*, 79-90.

(26) Van Eijnatten, M. A.; Van Rijssel, M. J.; Peters, R. J.; Verdaasdonk, R. M.; Meijer, J. H. Comparison of cardiac time intervals between echocardiography and impedance cardiography at various heart rates., *J. Elec. Bioimped.* **2019**, *5*, 2– 8.

(27) Pradhan, R.; Mitra, A. D., S. . Quantitative evaluation of blood glucose concentration using impedance sensing devices, *J. Elec. Bioimped.* **2019**, *4*, 73– 77.

(28) Vardi, R.; Goldental, A.; Marmari, H.; Brama, H.; Stern, E. A.; Sardi, S.; Sabo, P.; Kanter, I. Neuronal response impedance mechanism implementing cooperative networks with low firing rates and μs precision, *Fron. Neural Circ.* **2015**, *9*.

(29) Bou, A.; Pockett, A.; Raptis, D.; Watson, T.; Carnie, M. J.; Bisquert, J. Beyond Impedance Spectroscopy of Perovskite Solar Cells: Insights from the Spectral Correlation of the Electrooptical Frequency Techniques, *J. Phys. Chem. Lett.* **2020**, *11*, 8654-8659.

(30) Fletcher, S. Tables of Degenerate Electrical Networks for Use in the Equivalent-Circuit Analysis of Electrochemical Systems, *J. Electrochem. Soc.* **1994**, *141*, 1823-1826.

(31) Koper, M. T. M. Oscillations and Complex Dynamical Bifurcations in Electrochemical Systems, *Adv. Chem. Phys.* **1996**, *92*, 161.

(32) Naito, M.; Tanaka, N.; Okamoto, H. General relationship between complex impedance and linear stability in electrochemical systems, *J. Chem. Phys.* **1999**, *111*, 9908-9917.

(33) Gonzales, C.; Guerrero, A.; Bisquert, J. Spectral properties of the dynamic state transition in metal halide perovskite-based memristor exhibiting negative capacitance, *App. Phys. Lett.* **2021**, *118*, 073501.

(34) T. M. Koper, M. Non-linear phenomena in electrochemical systems, *J. the Chem. Soc. Farad. Trans.* **1998**, *94*, 1369-1378.

(35) Chua, L.; Sbitnev, V.; Kim, H. Hodgkin–Huxley axon is made of memristors, *Int. J. Bifurc. Chaos* **2012**, *22*, 1230011.

(36) Chua, L.; Sbitnev, V.; Kim, H. Neurons are poised near the edge of chaos, *Int. J. Bifurc. Chaos* **2012**, *22*, 1250098.

(37) Yang, J.-Q.; Wang, R.; Wang, Z.-P.; Ma, Q.-Y.; Mao, J.-Y.; Ren, Y.; Yang, X.; Zhou, Y.; Han, S.-T. Leaky integrate-and-fire neurons based on perovskite memristor for spiking neural networks, *Nano Energy* **2020**, *74*, 104828.

(38) Chua, L. Memristor-The missing circuit element, *IEEE Trans. Circuit Theory* **1971**, *18*, 507-519.

(39) Strukov, D. B.; Snider, G. S.; Stewart, D. R.; Williams, R. S. The missing memristor found, *Nature* **2008**, *453*, 80-83.

(40) Sun, K.; Chen, J.; Yan, X. The Future of Memristors: Materials Engineering and Neural Networks, *Adv. Func. Mater.* **2021**, *31*, 2006773.

(41) Pershin, Y. V.; Di Ventra, M. Memory effects in complex materials and nanoscale systems, *Adv. Phys.* **2011**, *60*, 145-227.

(42) Linares-Barranco, B.; Serrano-Gotarredona, T. Memristance can explain Spike-Time-Dependent-Plasticity in Neural Synapses, *Nature Proceedings* **2009**.

(43) Jo, S. H.; Chang, T.; Ebong, I.; Bhadviya, B. B.; Mazumder, P.; Lu, W. Nanoscale Memristor Device as Synapse in Neuromorphic Systems, *Nano Lett.* **2010**, *10*, 1297-1301.

(44) Prezioso, M.; Mahmoodi, M. R.; Bayat, F. M.; Nili, H.; Kim, H.; Vincent, A.; Strukov, D. B. Spike-timing-dependent plasticity learning of coincidence detection with passively integrated memristive circuits, *Nat. Commun.* **2018**, *9*, 5311.

(45) *Advances in Neuromorphic Memristor Science and Applications*; Kozma, R.; Pino, R. E.; Pazienza, G. E., Eds.; Springer, 2012.

(46) Mehonic, A.; Shluger, A. L.; Gao, D.; Valov, I.; Miranda, E.; Ielmini, D.; Bricalli, A.; Ambrosi, E.; Li, C.; Yang, J. J.; Xia, Q.; Kenyon, A. J. Silicon Oxide (SiOx): A Promising Material for Resistance Switching?, *Adv. Mater.* **2018**, *30*, 1801187.

(47) Jiang, X.; Ma, Z.; Xu, J.; Chen, K.; Xu, L.; Li, W.; Huang, X.; Feng, D. a-SiNx:H-based ultra-low power resistive random access memory with tunable Si dangling bond conduction paths, *Sci. Rep.* **2015**, *5*, 15762.

(48) Yang, J. J.; Pickett, M. D.; Li, X.; Ohlberg, D. A. A.; Stewart, D. R.; Williams, R. S. Memristive switching mechanism for metal/oxide/metal nanodevices, *Nat. Nanotech.***2008**, *3*, 429-433.

(49) Wang, X.; Shao, Q.; Ku, P. S.; Ruotolo, A. A memristive diode for neuromorphic computing, *Microel. Eng.* **2015**, *138*, 7-11.

(50) van de Burgt, Y.; Gkoupidenis, P. Organic materials and devices for brain-inspired computing: From artificial implementation to biophysical realism, *MRS Bulletin* **2020**, *45*, 631-640.

(51) Javad, M.; Hossein, M.; Donati, E.; Yokota, T.; Lee, S.; Indiveri, G.; Someya, T.; Nawrocki, R. A. Organic electronics Axon-Hillock neuromorphic circuit: towards biologically compatible, and physically flexible, integrate-and-fire spiking neural networks, *J. Phys. D: Appl. Phys.* **2021**, *54*, 104004.

(52) Li, B.; Hui, W.; Ran, X.; Xia, Y.; Xia, F.; Chao, L.; Chen, Y.; Huang, W. Metal halide perovskites for resistive switching memory devices and artificial synapses, *J. Mat. Chem. C* **2019**, *7*, 7476-7493.

(53) Harikesh, P. C.; Febriansyah, B.; John, R. A.; Mathews, N. Hybrid organic—inorganic halide perovskites for scaled-in neuromorphic devices, *MRS Bulletin* **2020**, *45*, 641-648.

(54) Solanki, A.; Guerrero, A.; Zhang, Q.; Bisquert, J.; Sum, T. C. Interfacial Mechanism for Efficient Resistive Switching in Ruddlesden-Popper Perovskites for Non-Volatile Memories, *J. Phys. Chem. Lett.* **2020**, *11*, 463-470.

(55) Kim, S. G.; Van Le, Q.; Han, J. S.; Kim, H.; Choi, M.-J.; Lee, S. A.; Kim, T. L.; Kim, S. B.; Kim, S. Y.; Jang, H. W. Dual-Phase All-Inorganic Cesium Halide Perovskites for Conducting-Bridge Memory-Based Artificial Synapses, *Adv. Func. Mater.* **2019**, *29*, 1906686.

(56) Zhao, X.; Xu, H.; Wang, Z.; Lin, Y.; Liu, Y. Memristors with organic-inorganic halide perovskites, *InfoMat* **2019**, *1*, 183-210.

(57) Choi, J.; Han, J. S.; Hong, K.; Kim, S. Y.; Jang, H. W. Organic–Inorganic Hybrid Halide Perovskites for Memories, Transistors, and Artificial Synapses, *Adv. Mater.* **2018**, *30*, 1704002.

(58) Dorf, R. C.; Bishop, R. H. *Modern Control Systems, 13th edition*; Pearson, 2017.

(59) Chua, L. Resistance switching memories are memristors, *Appl. Phys. A* **2011**, *102*, 765-783.

(60) Abraham, I. The case for rejecting the memristor as a fundamental circuit element, *Sci. Rep.* **2018**, *8*, 10972.

(61) Bisquert, J.; Guerrero, A.; Gonzales, C. Theory of hysteresis in halide perovskites by integration of the equivalent circuit *ACS Chem. Phys. Au* **2021**.

(62) Zohar, A.; Kedem, N.; Levine, I.; Zohar, D.; Vilan, A.; Ehre, D.; Hodes, G.; Cahen, D. Impedance Spectroscopic Indication for Solid State Electrochemical Reaction in $(CH_3NH_3)PbI_3$ Films, *J. Phys. Chem. Lett.* **2016**, *7*, 191-197.

(63) Fabregat-Santiago, F.; Kulbak, M.; Zohar, A.; Vallés-Pelarda, M.; Hodes, G.; Cahen, D.; Mora-Seró, I. Deleterious Effect of Negative Capacitance on the Performance of Halide Perovskite Solar Cells, *ACS Energy Lett.* **2017**, *2*, 2007-2013.

(64) Guerrero, A.; Garcia-Belmonte, G.; Mora-Sero, I.; Bisquert, J.; Kang, Y. S.; Jacobsson, T. J.; Correa-Baena, J.-P.; Hagfeldt, A. Properties of Contact and Bulk Impedances in Hybrid Lead Halide Perovskite Solar Cells Including Inductive Loop Elements, *J. Phys. Chem. C* **2016**, *120*, 8023-8032.

(65) Bisquert, J.; Garcia-Belmonte, G.; Pitarch, A.; Bolink, H. Negative capacitance caused by electron injection through interfacial states in organic light-emitting diodes, *Chem. Phys. Lett.* **2006**, *422*, 184-191.

(66) Mora-Seró, I.; Bisquert, J.; Fabregat-Santiago, F.; Garcia-Belmonte, G.; Zoppi, G.; Durose, K.; Proskuryakov, Y. Y.; Oja, I.; Belaidi, A.; Dittrich, T.; Tena-Zaera, R.; Katty, A.; Lévy-Clement, C.; Barrioz, V.; Irvine, S. J. C. Implications of the negative capacitance observed at forward bias in nanocomposite and polycrystalline solar cells, *Nano Lett.* **2006**, *6*, 640-650.

(67) Göhr, H.; Schiller, C.-A. Faraday-Impedanz als Verknüpfung von Impedanzelementen, *Zeitschrift für Physikalische Chemie* **1986**, *148*, 105-124.

(68) Ghahremanirad, E.; Bou, A.; Olyaee, S.; Bisquert, J. Inductive Loop in the Impedance Response of Perovskite Solar Cells Explained by Surface Polarization Model, *J. Phys. Chem. Lett.* **2017**, 1402-1406.

(69) Dualeh, A.; Moehl, T.; Tétreault, N.; Teuscher, J.; Gao, P.; Nazeeruddin, M. K.; Grätzel, M. Impedance spectroscopic analysis of lead iodide perovskite-sensitized solid-state solar cells, *ACS Nano* **2014**, *8*, 362-373.

(70) Khan, M. T.; Huang, P.; Almohammedi, A.; Kazim, S.; Ahmad, S. Mechanistic origin and unlocking of negative capacitance in perovskites solar cells, *iScience* **2021**, *24*.

(71) Alvarez, A. O.; Arcas, R.; Aranda, C. A.; Bethencourt, L.; Mas-Marzá, E.; Saliba, M.; Fabregat-Santiago, F. Negative Capacitance and Inverted Hysteresis: Matching Features in Perovskite Solar Cells, *J. Phys. Chem. Lett.* **2020**, *11*, 8417-8423.

(72) Klotz, D. Negative capacitance or inductive loop? – A general assessment of a common low frequency impedance feature, *Electrochem. Comm.* **2019**, *98*, 58-62.

(73) Taibl, S.; Fafilek, G.; Fleig, J. Impedance spectra of Fe-doped SrTiO3 thin films upon bias voltage: inductive loops as a trace of ion motion, *Nanoscale* **2016**, *8*, 13954-13966.

(74) Greenlee, J. D.; Calley, W. L.; Moseley, M. W.; Doolittle, W. A. Comparison of Interfacial and Bulk Ionic Motion in Analog Memristors, *IEEE Trans. Electron Devices* **2013**, *60*, 427-432.

(75) Lanza, M.; Wong, H. S. P.; Pop, E.; Ielmini, D.; Strukov, D.; Regan, B. C.; Larcher, L.; Villena, M. A.; Yang, J. J.; Goux, L.;et al. Recommended Methods to Study Resistive Switching Devices, *Adv. Electron. Mater.* **2019**, *5*, 1800143.

(76) Brette, R.; Gerstner, W. Adaptive exponential integrate-and-fire model as an effective description of neuronal activity., *J Neurophysiol.* **2005**, *94*, 3637-3642.

(77) Touboul, J.; Brette, R. Dynamics and bifurcations of the adaptive exponential integrate-and-fire model, *Biological Cybernetics* **2008**, *99*, 319.

(78) Ashida, G.; Nogueira, W. Spike-Conducting Integrate-and-Fire Model, *eNeuro* **2018**, *5*, ENEURO.0112-0118.2018.

(79) Górski, T.; Depannemaecker, D.; Destexhe, A. Conductance-Based Adaptive Exponential Integrate-and-Fire Model, *Neural Computation* **2021**, *33*, 41-66.

(80) Fardet, T.; Ballandras, M.; Bottani, S.; Métens, S.; Monceau, P. Understanding the Generation of Network Bursts by Adaptive Oscillatory Neurons, *Front. Neurosci.* **2018**, *12*, 41.

(81) Barranca, V. J.; Johnson, D. C.; Moyher, J. L.; Sauppe, J. P.; Shkarayev, M. S.; Kovačič, G.; Cai, D. Dynamics of the exponential integrate-and-fire model with slow currents and adaptation, *J. Comp.Neurosci.***2014**, *37*, 161-180.

(82) Naud, R.; Marcille, N.; Clopath, C.; Gerstner, W. Firing patterns in the adaptive exponential integrate-and-fire model, *Biological Cybernetics* **2008**, *99*, 335.

(83) Karantonis, A.; Nakabayashi, S. Phase flow deformations and coupled electrochemical oscillators, *Chem. Phys. Lett.* **2001**, *347*, 133-137.

(84) Rotstein, H. G. Preferred frequency responses to oscillatory inputs in an electrochemical cell model: Linear amplitude and phase resonance, *Physical Review E* **2013**, *88*, 062913.

(85) Fourcaud-Trocmé, N.; Hansel, D.; van Vreeswijk, C.; Brunel, N. How Spike Generation Mechanisms Determine the Neuronal Response to Fluctuating Inputs, *The Journal of Neuroscience* **2003**, *23*, 11628-11640.

(86) Koper, M. T. M.; Sluyters, J. H. Instabilities and oscillations in simple models of electrocatalytic surface reactions, *J. Electroanal. Chem.* **1994**, *371*, 149.

(87) Koper, M. T. M. Non-linear phenomena in electrochemical systems, *Journal of the Chemical Society, Faraday Transactions* **1998**, *94*, 1369.

(88) Glarum, S. H.; Marshall, J. H. The Anodic Dissolution of Copper into Phosphoric Acid: II . Impedance Behavior, *J. Electrochem. Soc.* **1985**, *132*, 2878-2885.

(89) Sadkowski, A.; Dolata, M.; Diard, J.-P. Kramers-Kronig Transforms as Validation of Electrochemical Immittance Data Near Discontinuity, *J. Electrochem. Soc.* **2004**, *151*, E20.

(90) Malmivuo, J.; Plonsey, R. - *Bioelectromagnetism: Principles and Applications of Bioelectric and Biomagnetic Fields*, 1995.

(91) Kandel, E. R. *Principles of neural science*, 2013.

Supporting Information

Impedance spectroscopy dynamics of biological neural elements: from memristors to neurons and synapses

Agustín Bou, Juan Bisquert*

Institute of Advanced Materials (INAM), Universitat Jaume I, 12006 Castelló, Spain

Email: bisquert@uji.es

Elements of the equivalent circuit for each model

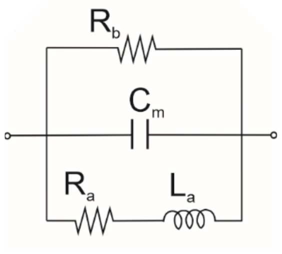

Figure 3. Equivalent circuit with an inductor and a capacitor, representative of a memristor.

The equivalent circuit (EC), represented in Figure 3, has the elements R_a, R_b, L_a and C_m.

The EC stands for both

-the general memristor model, and

- the Adaptative exponential integrate-and-fire neuron model.

The EC is obtained in both cases from the kinetic equations of these models. Hence, in each case the elements of the circuit depend on the parameters of the kinetics models, which are obviously different. Therefore, the relations that the elements of the circuit have with the model parameters and between them are different for each model.

In Table S1, we show a summary of the values for the EC parameters R_a, R_b, τ_m and τ_k. The parameters C_m and L_a are not shown because they are redundant with τ_m and τ_k, and R_I is a parameter of the kinetic models. Additionally, we give the values of R_{dc} which are relevant for the conditions of different spectra.

Table S1. Equivalent circuit parameters

	Memristor model	AdEx neuron model
R_a	$-\frac{g_w}{G_w g_u \bar{u}}$	R_a
R_b	$(\bar{G} + G_u \bar{u})^{-1}$	$\frac{R_I}{1 - \exp\left(\frac{\bar{u} - \theta_{th}}{\Delta_T}\right)}$
τ_m	$R_I C_m$	$R_I C_m$
τ_k	$(G_w g_u \bar{u}) L_a$	L_a / R_a
$R_{dc} = \left(\frac{1}{R_a} + \frac{1}{R_b}\right)^{-1}$	$\left(-\frac{G_w g_u \bar{u}}{g_w} + \bar{G} + G_u \bar{u}\right)^{-1}$	$\left(\frac{1}{R_a} + \frac{1 - \exp\left(\frac{\bar{u} - \theta_{th}}{\Delta_T}\right)}{R_I}\right)^{-1}$

In Table S2, we summarize the different conditions of the equivalent circuit elements for different types of spectra. Substituting Table S1 values into the conditions of Table S2, we can obtain each condition in terms of the parameters of each model, specifically.

Table S2. Conditions on the equivalent circuit elements

The frequency of the intercept $Z''(\omega_1) = 0$	$\omega_1 = \left(\omega_{LC}^2 - \frac{1}{\tau_k^2}\right)^{1/2} = \left[\frac{1}{L_a C_m} - \left(\frac{R_a}{L_a}\right)^2\right]^{1/2}$
$R_{Z''=0} > R_{dc}$ (condition for the loop in the fourth quadrant)	$\tau_k > R_a C_m$
The resistance at the intercept $Z'' = 0$	$R_{Z''=0} = \frac{R_b}{1 + R_a R_b C_m / L_a}$
Region of R_b negative but R_{dc} still positive (“hidden negative impedance”)	$-R_a > R_b$

General Conclusions

Perovskites have an enormous potential as a semiconductor material for a variety of applications due to their ideal properties for light absorption and electronic transport. Moreover, they have an additional uncommon property, which is the combined ionic-electronic conductivity. Although this characteristic may appear problematic for the construction of solar cells, it can be a desirable property for alternative applications, such as perovskite memristors. In this thesis we have contributed to the understanding of perovskites for both solar cells and memristors, by studying them with small perturbation techniques.

In the case of perovskite solar cells, we have developed a successful model and equivalent circuit for understanding the characteristic inductive behaviours that such devices present in IS measurements. However, this model has not been able to serve for the extraction of electronic parameters of perovskites. For that purpose, we have had to resort to the use of a combination of techniques, connecting light-modulated techniques with IS. The use of IMPS has led to the observation of a special characteristic of carbon-based perovskite solar cells that, eventually, has uncovered the diffusion of electronic charges in perovskites. Therefore, the electronic diffusion of perovskites has been finally obtained from small perturbation techniques under conditions of non-uniform generation profiles. Specifically, we have calculated the diffusion parameters of perovskites from the spiralling feature of the high frequency part of IMPS spectra.

From this finding, we have identified the factor that allows the display of the diffusion trace in light-modulated techniques in contrast with voltage-modulated ones. By calculating the transfer functions of IS, IMPS and IMVS produced by a non-uniform generation profile inside the perovskite films, we have shown the differences between modulation of light and voltage. We point to the spiralling high-frequency loop of IMPS and IMVS as the trace of diffusion in perovskites. We have complemented this calculations with experimental data and we have demonstrated experimentally the results obtained in our models. Finally, we have proved the relation between the techniques, and we have been able to distinguish the features that occur at different timescales.

In the case of perovskite memristors, we have linked the responses of the previous impedance model and equivalent circuit developed for IS of perovskite solar cells with the responses of perovskite memristors and any theoretical memristor. We have developed a systematic method for the analysis of the similarity of their IS characteristics with neuron models, broadening the possibilities to study these devices as a possible candidate for applications in neuromorphic networks. For such purpose, we have calculated the impedance characteristics of two reference models for neuron operation: the integrate-and-fire neuron model and the Hodgkin-Huxley model. We have found similarities with perovskite memristors but we have also found added complexity to the spectral characteristics of memristors. Therefore, further investigation is needed to acquire the neuromorphic computation with perovskite memristors. Nevertheless, the IS investigation has the great advantage that the analysis of highly complex phenomena can be based purely on the shape of experimental impedance spectra and the identification of similarities in the equivalent circuits.